UNIVERSITAT DE BARCELONA

DEPARTAMENT DE FÍSICA APLICADA I ÒPTICA

Av. Diagonal, 647, 08028 Barcelona

PROGRESS IN HOT-WIRE DEPOSITED NANOCRYSTALLINE SILICON SOLAR CELLS

Marta Fonrodona Turon

Memòria presentada per optar al grau de Doctor

Barcelona, juny de 2003

UNIVERSITAT DE BARCELONA

DEPARTAMENT DE FÍSICA APLICADA I ÒPTICA

Av. Diagonal, 647, 08028 Barcelona

PROGRESS IN HOT-WIRE DEPOSITED NANOCRYSTALLINE SILICON SOLAR CELLS

Marta Fonrodona Turon

Programa de doctorat: Tècniques Instrumentals de la Física i la Ciència de Materials

Bienni: 1998-2000

Tutor: Enric Bertran Serra

Director: Joan Bertomeu i Balagueró

Memòria presentada per optar al grau de Doctor

Barcelona, juny de 2003

A la Pepeta, la Núria
i tots els que hi ha entremig.

This work has been carried out in the Laboratory of Thin Film Materials of the Department of Applied Physics and Optics of the University of Barcelona, supervised by Dr. Joan Bertomeu Balagueró, in the framework of the projects TIC98-0381-C0201 and MAT2001-3541-C03-01 of the CICYT of the Spanish Government , and also with the aid of the project JOR3-CT97-0126 in the JOULE programme of the European Commission. The stage at Utrecht University was possible thanks to grant 2001BEAI200159 of Generalitat de Catalunya.

Contents

Agraïments

Aquest escrit és fruit d'una mica més de quatre anys de treball però no tan sols és això. Enmig d'aquestes pàgines hi ha estones, esforços i, sobretot, persones que no haurien de passar desapercebudes. Sense el seu ajut i encoratjament aquesta tesi no hauria estat possible.

Primerament, voldria agrair al Dr. José-Luís Morenza, director del departament de Física Aplicada i Òptica, haver-me acceptat com a estudiant de doctorat, fet que m'ha permès conèixer de primera mà el món de la recerca.

Seguidament voldria agrair al Dr. Joan Bertomeu, director d'aquesta tesi, i al Dr. Jordi Andreu, cap del grup fotovoltaic, el seu suport i confiança durant aquests quatre anys. De la mateixa manera voldria agrair-los tots els coneixements adquirits durant les innombrables discussions i les oportunitats de dur a la pràctica alguna de les meves iniciatives. També cal agrair-li a en Jordi els somriures que han suscitat les seves, ara famoses, exageracions. No sé passar per la terminal A del Prat sense mirar el sostre.

També vull donar les gràcies al Dr. David Peiró i al Dr. Cristóbal Voz per la paciència d'explicar-me el funcionament del reactor de Hot-Wire i les diferents tècniques de caracterització. En especial vull agrair a en Cristóbal totes les mesures i atacs de cèl·lules que amablement ens ha fet a la UPC. Al Dr. José Miguel Asensi voldria agrair-li, especialment, l'esforç posat en la millora del sistema de mesura de dispositius (aunque ese linux me tenga manía!) i totes les explicacions.

Si en aquests quatre anys hi ha algú que m'ha patit en dosis probablement més altes del recomanable és en David Soler. Gràcies per la paciència, les mesures i l'ajut sempre que ho he necessitat. Gràcies també per compartir hores i hores de dipòsit i el fatídic moment de la mesura de les cèl·lules, per tots els CD's que m'he piratejat (mmm... sóc petita!) i, sobretot, per la teva amistat.

Quatre anys de tesi donen per molts esmorzars i berenars al bar. Aquestes estones no haurien estat les mateixes sense la companyia del Dr. J.Marcos Fernández, el Dr. Pere Serra i la Dra. Elena Martínez. Al Marcos li agraeixo els consells i truquets apresos, el mig kit-kat de l'hora de berenar (encara que tot sovint oblidi a qui li toca pagar...) i la seva

amistat i paciència amb el “lastre”. Al Pere, les converses de cinema i llibres, i a l’Elena, les bones estones, el suport... i la xocolata!

També voldria agrair al Dr. Cèsar Ferrater i el Dr. Adolf Canillas les bones estones passades a les hores de dinar. Aquells àpats no haurien estat el mateix sense l’esmerçar-se constant d’en Cèsar i l’Adolf a la recerca de l’expressió més escaient en cada moment.

També vull donar les gràcies per tots els moments compartits durant tot aquest temps a en Jordi R. (the man in black), l’Ángel (el hombre de las camisas a cuadros), l’Albert (com era allò... lleig-i-antipàtic, oi Pinyolet?), la Cristina (que, no sé si és bo o dolent, però és com si fossis de planta 4...), en Jordi E. i en Ferran (que m’han patit de srta. Rotenmeyer!) i a tota la resta de companys de departament. Menció a part per a en Jordi Solà, l’eficiència personificada, per facilitar-nos sempre tant com fos possible les feixugues tasques burocràtiques.

I thank all the people at the group of Physics of Devices at Utrecht University for the nice three months I spent there. I especially want to thank Prof. Ruud Schropp for accepting me as guest in his lab. Thanks also to Bernd, Marieke, Aad, Karine, Patrick and Raúl for making me feel like at home. Bedankt voor een erg leuke tijd in Nederland!

I also acknowledge the members of the Thesis Jury, for accepting our invitation and reading this manuscript.

Finalment, vull agrair el suport incondicional i els consells a la família i els amics. A la Núria li vull agrair especialment la paciència que fa falta per conviure (gairebé tres anys ja!) soleta amb una germana gran una mica llunada. I finalment, com que allò que es promet s’ha de complir, vull donar-li les gràcies (bé, és un dir...) a la meva mare pel seu constant rondinar. No sé si sense, la tesi s’hauria acabat abans o després, però segur que m’hauria semblat més curta sense ningú que em preguntés cada divendres si ja l’havia acabada!

Marta

1. Introduction

1.1. Thin film silicon technology

Nowadays, about 99% of the solar cell world production for photovoltaic terrestrial applications is dominated by silicon related materials, an 85% of which corresponds to the so-called wafer technology [Goetzberger et al., 2003]. However, efforts heading to a reduction in production and manufacturing costs have, over the past decades, drawn special attention to the development of thin film silicon technology. Currently, the 50% of the cost of a crystalline silicon module is due to the cost of processed silicon wafers. In thin film silicon technology, the amount of material necessary to produce a solar cell is up to five hundred times less than in the case of wafer-based cells. Besides, such devices can be easily deposited on low cost substrates (i.e., glass, stainless steel or plastics) using relatively simple techniques that allow the possibility of large area deposition and roll-to-roll processes in mass production.

Among the different possible morphologies achievable in the wide range of thin film silicon materials, amorphous silicon (a-Si:H) is the most commonly used one due to its enhanced light absorption that makes it feasible to deposit devices with total thicknesses well below 1 μm. Unfortunately, a-Si:H presents a major drawback, the fact that its electrical properties degrade when the material is exposed to illumination due to the generation of light-induced defects, the so-called Staebler-Wronski effect after the scientists who first described this behaviour [Staebler and Wronski, 1977].

Parallel to a-Si:H technology, different types of thin film silicon materials have also been developed for solar cell applications: protocrystalline (p-Si:H) [Ahn et al., 2003], polymorphous (pm-Si:H) [Fontcuberta et al., 2002], nanocrystalline (nc-Si:H) [Brünhe et al., 2001], microcrystalline (μc-Si:H) [Meier et al., 2002] and polycrystalline silicon (poly-Si:H) [Schropp and Rath, 1999]. In all cases, the H in the abbreviation stands for hydrogenated, due to the presence of this element in the silicon network. At first sight, the different morphologies could be generally classified by the differences in the amount of amorphous phase present and the crystallite size. While p-Si:H and pm-Si:H mainly refer to very small grains embedded in a mostly amorphous material, poly-Si:H is defined as a single-phase crystalline material with grain boundaries [Schropp and Zeman, 1998]. On the

other hand, both nc-Si:H and μc-Si:H refer to a two-phase amorphous and crystalline material with grain sizes of the order of tens of nm and both terms end up being indistinguishable in literature. Throughout this work, the term employed to describe the above-mentioned material will be nc-Si:H.

1.2. Nanocrystalline silicon

As described in the previous section, the term nc-Si:H refers to an aggregate of crystallites with sizes in the range of few tens of nanometers embedded in an amorphous matrix. One of the characteristic features of material containing small crystals is the presence of grain boundaries.

When to be applied as active layer in thin film solar cells, intrinsic nc-Si:H layers have to fulfil certain requirements so that devices with reasonably good properties are obtained. These "device-quality" material properties are, according to [Schropp and Zeman, 1998], those listed in table 1.1:

Crystalline preferential orientation	(220)
Band gap (indirect)	1.0-1.1 eV
100 mW/cm^2 photoconductivity	> 10^{-5} S/cm
Dark conductivity	< 10^{-7} S/cm
Activation energy	~ 0.55 eV

Table 1.1. Criteria for "device-quality" intrinsic nanocrystalline silicon, extracted from [Schropp and Zeman, 1998].

These requirements mostly refer to those ensuring an intrinsic enough material to allow carrier transport through it. In that reference, also crystalline fractions higher than 90% are considered necessary in device-quality material, but recent results have pointed out better solar cell performances using nc-Si:H close to the transition to amorphous growth [Klein et al., 2002].

Nanocrystalline silicon is mostly obtained by Chemical Vapour Deposition (CVD) techniques. In them, material is deposited on the substrate after producing the dissociation of the gas mixture containing the precursor. Depending on the activation method considered, different CVD methods are distinguished. The most widely used ones are

Plasma-Enhanced CVD (PECVD) [Nasuno et al., 2002] and its variant Very High Frequency Glow Discharge (VHF-GD) [Shah et al., 2002]. Other CVD methods employed in the deposition of nc-Si:H are Electron Cyclotron Resonance CVD (ECR-CVD) [Hsiao et al., 1999] and Hot-Wire CVD (HWCVD) [Matsumura, 1991]. Furthermore, these kind of materials can be also grown by other techniques like Rapid Thermal Annealing (RTA) [Cheng et al., 2000], Laser Melt Recrystallisation (LMR) [Dyer et al., 1993] or aluminium-induced crystallisation [Aberle et al., 2001].

1.3. Hot-Wire Chemical Vapour Deposition

In Hot-Wire CVD, silicon deposition takes place upon catalytic decomposition of the reactant gases, i.e. silane (SiH_4) and hydrogen (H_2), at the surface of a hot filament heated at temperatures in the range of 1500-2000ºC. Tungsten (W) and tantalum (Ta) are, at present, the most widely used wire materials. This technique was first used to deposit a-Si:H by Wiesmann in 1979 [Wiesmann et al., 1979] and later on by Matsumura who not only deposited the first polycrystalline layers [Matsumura, 1991] but also introduced the term Catalytic CVD (Cat-CVD) to describe the process due to the catalytic nature of the reactions taking place at the surface of the catalyst. Nowadays, the two different terms coexist in literature to describe the same process. Nevertheless, the denomination Cat-CVD is less restrictive and comprises the use of other catalysts apart from wires, like foils or the so-called “catalytic plate” [Masuda et al., 2000].

Hot-Wire CVD is now becoming a mature technique in the field of thin silicon film deposition. Besides, it offers several features that overcome the limitations of PECVD technology, the currently most applied deposition technique in industry:

a) absence of ion bombardment during deposition
b) high deposition rates
c) low equipment implementation and upkeep costs
d) high gas utilisation [Honda et al., 2000]
e) easy scalability to large areas

Presently, Hot-Wire CVD yields devices with state-of-the-art properties: efficiencies as high as 9.4% have been achieved in single junction nc-Si:H solar cells with the active layer deposited by this technique [Klein et al., 2002]. This performance is comparable

to the best PECVD results reported [Yamamoto et al., 1998, Shah et al., 2002]. Hot-Wire thin silicon films have also been successfully applied in the field of thin film transistors (TFT), where high mobility and stability have been achieved [Stannowski et al., 2003]. Additionally, thanks to the simplicity of its geometry, large area HWCVD set-ups have been developed allowing homogeneous deposition over surfaces as large as 92 x 73 cm [Matsumura et al., 2003].

1.4. Hot-Wire CVD research at Universitat de Barcelona

Hot-Wire technology was first implemented at Universitat de Barcelona in 1993. Despite the fact that it was a very elementary set-up, the first polycrystalline layers grown in Europe with this technique were in our group [Cifre et al., 1994]. In situ doping of the layers by adding controlled amounts of doping gases (phosphine (PH_3) for n-type and diborane (B_2H_6) for p-type layers) was also demonstrated [Puigdollers et al., 1995].

Prior to the present work, the results concerning nc-Si:H technology at the Universitat de Barcelona can be found in the PhD thesis of Dr. D. Peiró [Peiró, 1999] and Dr. C. Voz [Voz, 2001]. The former of these complementary works mainly deals with an extensive description of the actual deposition set-up and the structural characterisation of the samples whereas the nucleus of the latter comprises electrical and optical studies of the material as well as device characterisation.

From the preliminary results regarding nc-Si:H solar cells in [Voz, 2001], where a 2.5% photovoltaic conversion efficiency in a p-i-n structure was reported, several drawbacks concerning the active layer, and mainly attributable to the incorporation of contaminants during and post deposition, were highlighted. It was concluded that deposition rates over 5 Å/s were necessary to obtain dark conductivity activation energies around midgap, and that such an increase also resulted in the lowering of the density of charged centres in the gap from 10^{17} to 10^{16} cm^{-3}. On the other hand, not only low deposition rates were responsible of a high density of charged centres, but so were high filament temperatures. Both trends are illustrated in figure 1.1 (extracted from [Voz, 2001]), where the concentration of charged centres was determined from the depletion capacitance of pseudo-Schottky contacts. Furthermore, several shallow donor levels ascribable to O and Cu were resolved by deep level transient spectroscopy (DLTS). As mentioned above, we

could attribute the origin of this behaviour to the undesired incorporation of contaminants (gas phase impurities, metallic components evaporated from the wire or its holders, or even impurities degassed from the reactor walls) during growth.

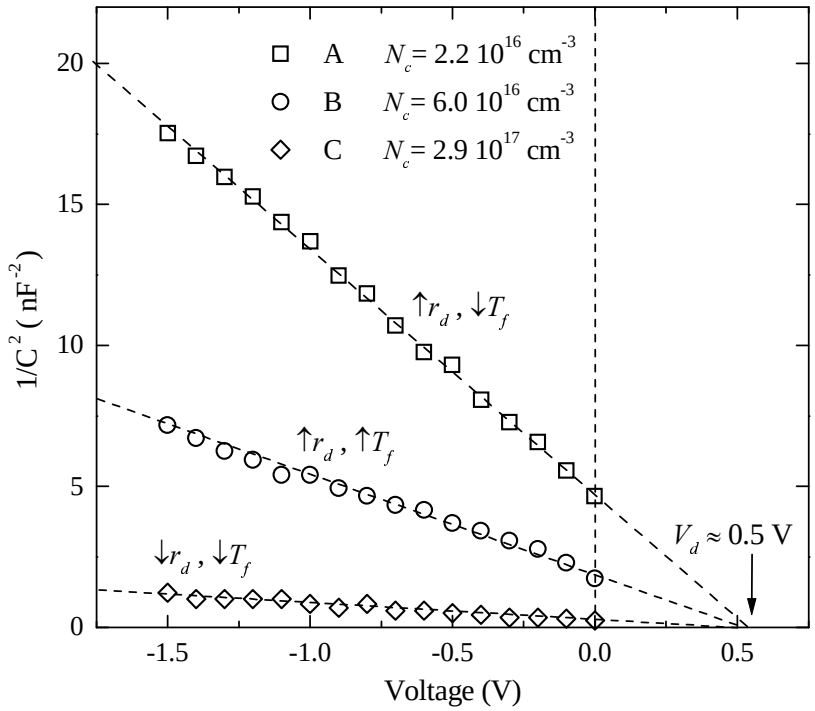

Fig. 1.1. Effect of deposition rate and filament temperature in the concentration of charged centres. Extracted with permission from [Voz, 2001].

Damaging effects of the undesired incorporation of contaminants were also evidenced in the photovoltaic conversion of p-i-n solar cells, as it was concluded that the performance of these preliminary devices was mainly limited by the screening of the electric field within the active layer. Thus, deposition conditions leading to a material with less concentration of impurities (high deposition rate and low filament temperatures) also resulted in solar cells with improved performance [Fig. 1.2].

Regarding the stability of the deposited devices, chemical instability leading to an increased n-type character and, thus, to a poorer performance of the device, was observed for samples exposed to air for a long time due to an important post-oxidation through the surface of the nc-Si:H films. Oxygen incorporation after deposition was imputable to porosity of the layers, in particular to lack of compactness in the regions comprised

between grains, which act as oxygen paths into the bulk of the layer as soon as the film is exposed to the atmosphere. Besides, post-oxidation was somehow accelerated under high irradiances when photons are able to break weak bonds, thus favouring oxidation.

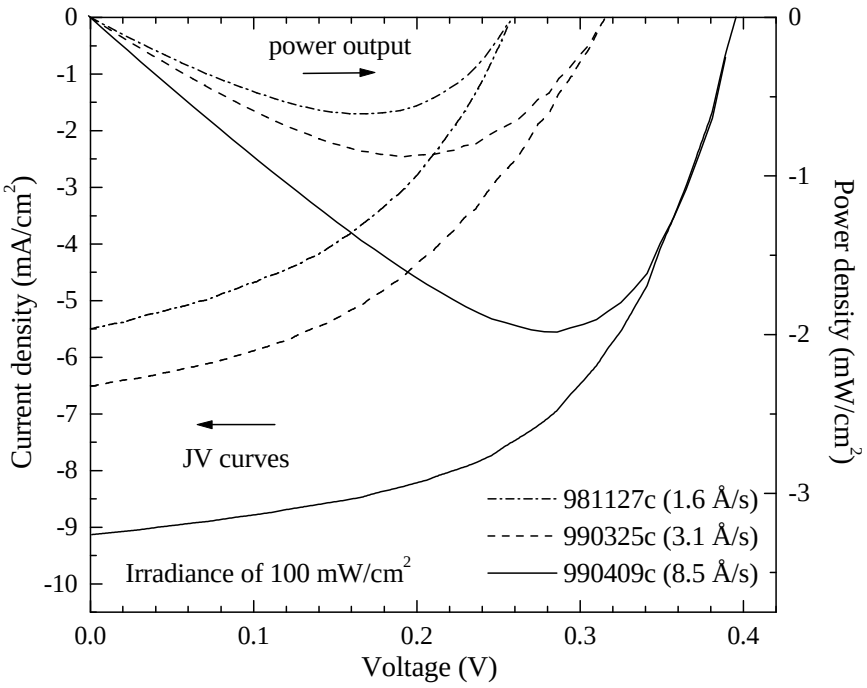

Fig. 1.2. J-V curves and power outputs under an irradiance of 100 mW/cm^2 for three solar cells obtained at different deposition rates. The efficiency is clearly correlated with the deposition rate. Extracted with permission from [Voz, 2001].

1.5. Aim and outline of this thesis

Taking as a starting point the state of the research in nc-Si:H deposited by HWCVD presented in the conclusions of the previous theses in our group, briefly summarised in the previous section, the main goal of the present work was the optimisation of both the deposition conditions and the set-up itself heading towards the obtaining of a stable nc-Si:H solar cell with an improved photovoltaic conversion.

Therefore, additionally to modifications in the internal arrangement of the set-up aiming to avoid the undesired incorporation of contaminants, special effort has been done to appropriately tune the deposition parameters in order to grow impurity-free compact material. Further on, preliminary strategies concerning light confinement to enhance light

absorption within the devices have also been considered together with stability studies of the solar cells.

Chapter 2 briefly describes the HWCVD set-up and the characterisation techniques used throughout the work. Special attention is paid to the modifications the chamber where intrinsic material is deposited has suffered in order to improve the quality of the layers.

Chapter 3 focuses on the growth of compact and chemically stable nc-Si:H. First of all, special attention is paid to the role of the filament and to oxygen incorporation after deposition. Afterwards, the effects of the inclusion of a protective funnel in the material and device properties are studied.

In chapter 4, the effect of the nature of the substrate on which thin film silicon layers are grown on their microstructure will be considered. The conclusions reached concerning intrinsic material will be validated in the case of doped material, the one actually grown onto a foreign substrate in a solar cell. Finally, scaling of doped layers to device size will be considered.

nc-Si:H solar cells are the nucleus of chapter 5. The first part of the chapter deals with all the different technological aspects that need to be taken into consideration when fully optimising a device: suppression of lateral leakage currents and light-trapping strategies. On the other hand, the second part of the chapter focuses in the performance of different solar cells, paying special attention to the stability against light soaking with relation to their microstructure. Finally, results of a preliminary solar cell where all the details described in the first part of the chapter have been implemented will be also presented.

The first annexe included describes the work carried out during a three-month stage at the at Debye Institute, SID – Physics of Devices at Utrecht University, The Netherlands. During the stage, first HW μc-Si:H n-type layers were deposited and characterised at the laboratory in Utrecht.

In the second annexe, in our research of a method to deposit impurity-free silicon thin films, silane decomposition upon collision with atomic hydrogen generated using titanium as catalyst, what will be called Low Temperature Cat-CVD, is considered. First layers deposited by this new technique are analysed.

Finally, the third annexe deals with device evaluation by means of Variable Illumination Measurement technique.

2. The HWCVD set-up. Characterisation techniques

This chapter briefly describes the HWCVD set-up and the characterisation techniques used to study the properties of our layers and devices. Extensive and more accurate descriptions of the set-up and the structural characterisation [Peiró, 1999] and of the electrical and optical characterisation [Voz, 2001] are part of previous works in our group. Special attention is paid to the modifications the chamber in which intrinsic material is deposited has suffered in order to improve the quality of the layers.

2.1. The HWCVD set-up

The HWCVD set-up at Universitat de Barcelona [Fig. 2.1] consists of three inline ultra-high vacuum (UHV) chambers isolated among them by gate valves and designed to make it feasible to deposit a whole solar cell without exposing the device interfaces to the atmosphere. A magnetic transfer system is used to place the substrate in the desired chamber.

HWCVD processes can take place in two of the chambers, whereas the third one acts as a load-lock and is also used to deposit transparent conductive oxide (TCO) by radio frequency (RF) magnetron sputtering. Several TCO films can be deposited by changing the 2" diameter target. In this work, ZnO:Al (deposited from a $ZnO:Al_2O_3$ 98:2 wt%, 99.99% purity ceramic target) is used as front contact in glass/TCO/p-i-n structures and also as back reflector in these superstrate structures (p-i-n/TCO/metal).

Two different chambers are employed to deposit intrinsic and doped nc-Si:H in order to avoid doping cross contamination in the active layer of the device. The presence of contaminants in the intrinsic active layer of a solar cell causes the screening of the electric field and makes such layers unsuitable to be implemented in photovoltaic devices [Voz et al., 2000].

Figure 2.2 shows the internal arrangement of one of the HWCVD deposition chambers. The gas mixture is catalytically dissociated by means of a metallic filament resistively heated at temperatures between 1500 and 2000ºC. Process pressure during deposition is tuned changing the pumping section of the turbo pump with the butterfly valve, permitting its control in a very wide range, independently of the gas flows entering the chamber.

Finally, uniform heating of the substrate is achieved using a 10 cm diameter resistive heater.

Fig. 2.1. Picture of the multichamber HWCVD set-up. The system was fabricated by the Scientific-Technical Services of Universitat de Barcelona.

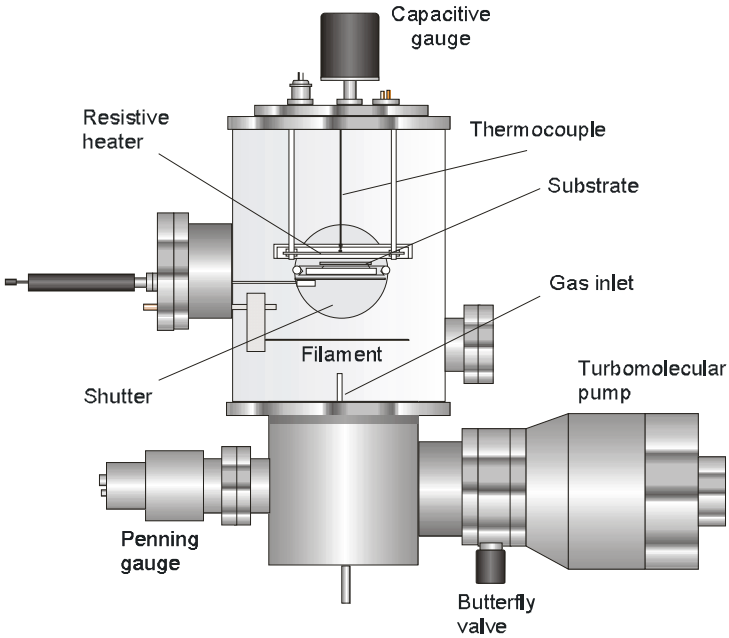

Fig. 2.2. Schematic cross-section of one of the HWCVD chambers.

2.2. Strategies against contaminants. Set-up modifications

The inner arrangement shown in figure 2.2 corresponds to the state in which the two HWCVD process chambers were at the beginning of this work. Several modifications have been carried out in the chamber where processes not involving doping gases take place in order to improve the quality of intrinsic nc-Si:H. These modifications were induced by the evidence of the presence of contaminants, mainly O and metallic impurities like Cu, coming from inside the chamber and their influence on the electrical properties of our devices [Voz et al., 2000].

2.2.1. External heater

Initially, internal graphite resistive heaters (10 cm diameter) were implemented in both HWCVD chambers so that good temperature uniformity was achievable over the whole substrate. Nevertheless, an internal heater is a potential source for impurities in intrinsic nc-Si:H layers. This fact motivated the change of the internal heater in the “intrinsic” chamber for an external one.

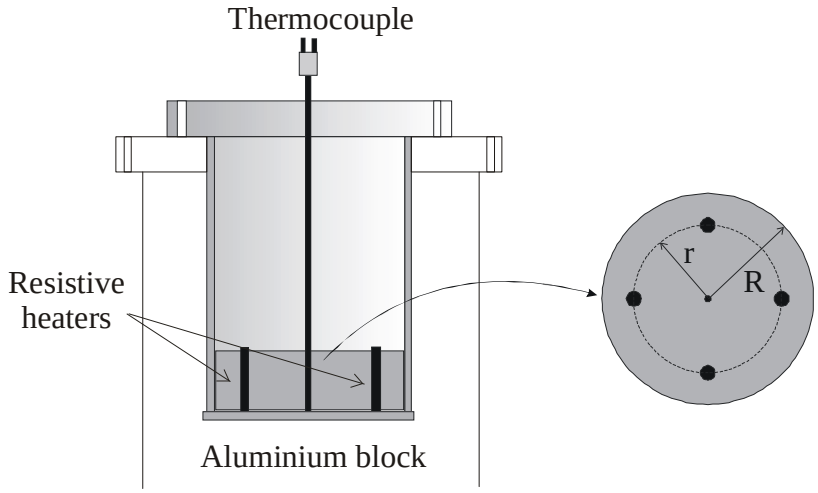

Fig. 2.3. Design of the new external heater.

The new external heater basically consisted of an aluminium block with four 200 W resistive heaters in it connected in parallel. The heater was placed 1.5 cm above the substrate holder. The design of the heater is shown in figure 2.3. The position of the

resistive heaters was calculated so that the block was homogeneously heated. Being R the radius of the block, the resistive heaters were located at a distance r = R/√2 from the centre. In this way, the area under the influence of each heater was maximal. The aluminium block was covered with K-Wool to avoid heat dissipation to the atmosphere.

The actual temperature of the substrate during deposition is one of the most difficult parameters to measure, and its value directly depends on the system used to heat the substrate. In order to verify whether the change of heater provoked a noticeable difference in the substrate temperature, we measured this crucial parameter in conditions similar to the process ones (P = $7x10^{-3}$ mbar, T_f = 1740ºC) and compared the obtained values with results of the same experiment performed with the internal heater [Peiró, 1999]. This experiment consisted in measuring the substrate temperature using a thermocouple attached to a glass substrate for different set-point temperatures. In both cases, temperature values were obtained once the value in the thermocouple located in the substrate holder had stabilised.

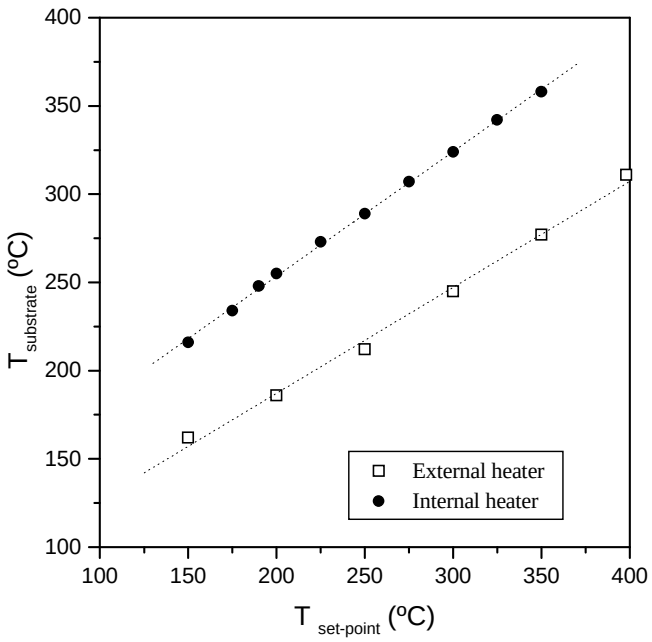

Fig. 2.4. Calibration of the substrate temperature as a function of the set-point temperature. Solid circles represent values obtained for an internal heater and a 1 mm diameter W-shaped filament (data extracted from [Peiró, 1999]) whereas open squares correspond to the new external heater and a 0.5 mm diameter 3-loop inverted basket-shaped wire.

The results for both heaters are presented in figure 2.4. In both cases, the substrate temperature exhibited a linear behaviour with the set-point temperature. On one hand, values obtained with the internal heater were always slightly higher to the set-point whereas, on the other hand, for set-point temperatures above 200ºC, the substrate temperature measured with the external heater turned to be somewhat lower to the set-point. This difference in the actual temperature measured partly could be attributed to the fact that the W-shaped 1 mm-thick tungsten wire dissipated more power than the 0.5 mm-thick basket-shaped one [Peiró, 1999]. In this experiment, dissipated power was around 340 W for the 1 mm-thick wire and about 170 W for the 0.5 mm-thick one.

Taking into account the linear behaviour existent between substrate and set-point temperatures and the difficulties to perform accurate measurements, from now on the term substrate temperature (T_s) will refer to the set-point values. Therefore, T_s will be an estimation of the actual substrate temperature. Nevertheless, this is enough when comparing technological series as in them the only change was the set-point value in the PID electronics that controls the heater.

2.2.2. The funnel

Deep level transient spectroscopy (DLTS) measurements performed in our samples revealed the existence of several shallow donor levels in the gap ($\Delta E < 0.1$ eV) attributable to the incorporation of oxygen in the films during growth [Stöger et al., 1999]. Since our set-up has UHV specifications and the gas inlet incorporates a feedgas purifier (SAES Getters MonoTorr®), we thought that this oxygen was degassed from the reactor walls or inner parts of the deposition chamber [Voz et al., 2000]. Further DLTS measurements also evidenced the presence of metallic impurities that were likely to come from the filament itself or its holders [Voz et al., 2000].

These results pointed out the necessity to shield the incoming gas flow and the substrate from the potential sources of impurities. The protective shield designed [Fig. 2.5] was, basically, a metallic funnel placed on the gas inlet and located around 1.5 cm beneath the substrate holder. Therefore, all species reaching the substrate after being dissociated by the filament come directly from the gas inlet. The funnel also avoids incoming gases from touching the cooler parts of the wire and prevents the formation of silicides in these critical

points of the wire. Similar strategies to confine the incoming gases and dissociated species inside a limited volume with no cold points or any other contamination sources have also been carried out by other groups [Guillet et al., 2000].

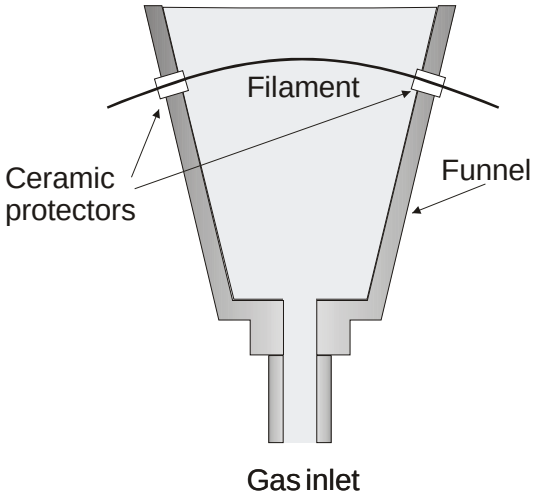

Fig. 2.5. Design of the protective funnel.

2.3. The wire

The wire is the main feature of HWCVD technology, but it is also its most delicate part. Thus, the research of the adequate filament to grow nc-Si:H has been the centre of many studies. Over the past decades, the possible use of different materials has been investigated, knowing that the filament material plays a role in the catalysis reactions that control the dissociation of the reactant gases. Special attention has been paid to refractory metals like tungsten (W) [Matsumura, 1998], tantalum (Ta) [Diehl et al., 1998] and molybdenum (Mo) [Matsumura, 1989], but other catalysers like graphite (C) [Morrison and Madan, 2001], palladium (Pa) [Ruihua et al., 2000] or rhenium (Re) [Veenendaal et al., 2002] have also been studied. Extremely short filament lifetimes have discarded Re and Pa as suitable materials, whereas carbon incorporation and the consequent degradation caused in the layers turned out to be the major problem of C wires.

W and Ta are, nowadays, the most commonly used filament materials. The choice between them seems to be conditioned by the range of working temperatures used. W seems more adequate when dealing with high filament temperatures ($T_f \sim 1800^oC$) as Ta has a trend to sag at these temperatures. On the other hand, dense nc-Si:H has been reported using Ta wires at low T_f, around 1600ºC [Fonrodona et al., 2002]. Tantalum is

more ductile and less brittle than tungsten, and it allows low temperature operation due to almost insignificant silicide formation, especially when compared to W. This ductility, together with the tendency to sag at moderately high T_f, makes Ta filaments more difficult to reproduce.

It is important to highlight that the fact that a difference in properties between nc-Si:H deposited using W and Ta in almost identical conditions [Veenendaal et al., 2001, Fonrodona et al., 2002] confirms the catalytic nature of the reactions taking place at the surface of the wire.

The main problem to be faced when dealing with hot-wires, regardless the material they are made of, is the breakage of the filament. When working with silane (diluted or undiluted), a build-up of silicon at the cold ends of the wire is commonly observed, and it is there where the break generally occurs. Different strategies have been followed in order to lengthen the life of the wire, but their main aim is always avoiding excessive silicide formation by avoiding high SiH_4 concentrations near the cooler parts of the filament. This can be done either by designing a hot-wire assembly with different inlets for H_2 and SiH_4 so that the former can prevent the latter from colliding with the cold ends of the catalyser [Ishibashi, 2001] or by avoiding this contact by means of an insulator-box that keeps all gases inside and the cold ends of the wire outside [Guillet et al., 2000 and section 2.2.2]. The life of the filament can be also further lengthened by an annealing treatment with H_2 gas at high T_f previous to each deposition [Schropp, 2002].

The majority of the samples analysed in this work have been deposited using Ta wires (99.9% purity, ∅ = 0.5 mm). Most usual filament geometry used is 3-loop inverted basket [Fig. 2.6], even though linear filaments have also been used after the implementation of the protective funnel. Nevertheless, unless mentioned otherwise, the wire shape considered is the basket one, in which more dissociation of the incoming gases is achieved. Basket-shaped filaments also result in a more homogeneous growth along the substrate than the linear one. This effect of the use of a linear wire could be solved by using two or more parallel filaments instead of only one.

The measurement of the filament temperature is carried out by means of an optical pyrometer. After the replacement of each filament, a calibration of its temperature as a function of the filament intensity is done and the data are fitted to the expression $I_f = k \cdot T_f^{\,n}$,

as is shown in figure 2.7. A 50ºC difference in T_f is easily found at a set I_f for different filaments. The intensity through the filament is indeed the actual parameter that is set during the deposition and reproduced from one wire to another to obtain the same material. Nevertheless, in this work T_f will be used as a descriptive parameter to provide better understanding of the deposition conditions.

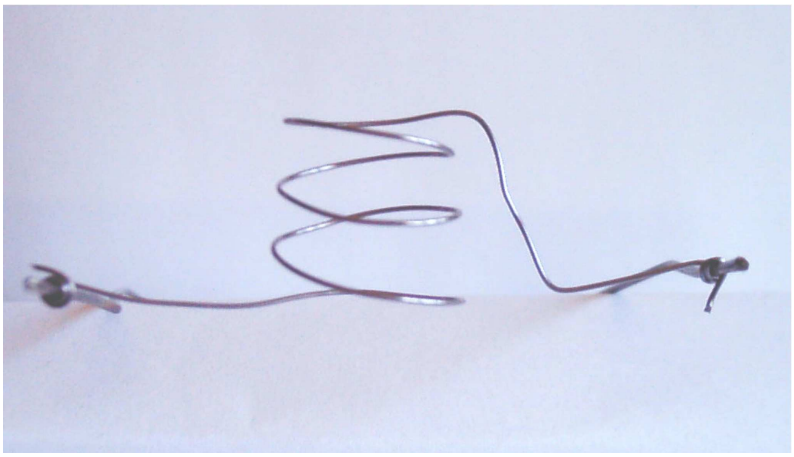

Fig. 2.6. Picture of a 3-loop basket-shaped Ta wire. The diameter of the filament is 0.5 mm and its height is around 2 cm.

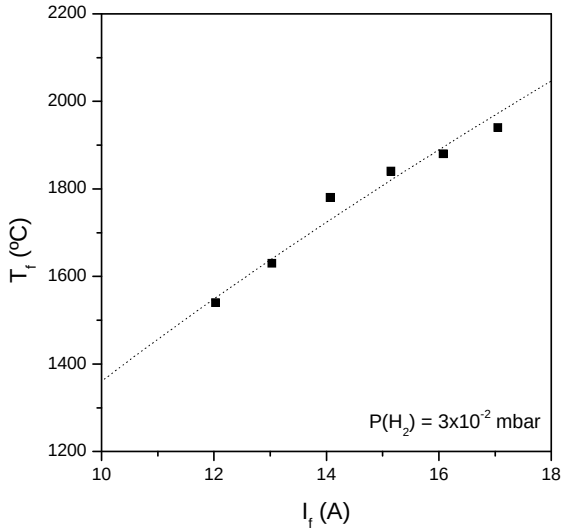

Fig. 2.7. Calibration of a Ta filament temperature as a function of the filament intensity.

2.4. Characterisation techniques

2.4.1. Morphology and structural properties

The first measurement carried out in every sample is thickness measuring and it is carried out by means of a Dektak 3030 stylus profilometer. From this value, knowing the deposition time of each sample, the average deposition rate (r_d) is determined.

Different characterisation techniques have been used to study the microstructure of the samples. Crystallinity of the nc-Si:H layers has been analysed by X-Ray Diffraction (XRD) in a Siemens D500 diffractometer in the Bragg-Brentano geometry. The standard method was the $\theta/2\theta$ scan, in which the diffraction peaks are obtained from the crystallographic planes oriented with the (hkl) axis perpendicular to the layer surface. Diffraction spectra give us information about the crystalline preferential orientation in the sample and allow the determination of the crystallite grain sizes (G_S) from the broadening of the diffraction peaks using the Scherrer formula [Cullity, 1977]. A deeper discussion of the treatment of the X-Ray spectra, as well as of the rest of the structural and compositional characterisations can be found in [Peiró, 1999].

Further structural characterisation has been performed by means of Raman spectroscopy using a Jobin-Yvon T64000 spectrometer at a wavelength of 514 cm^{-1}. Raman analysis of nc-Si:H are centred in the TO-phonon band of Si, as the crystalline fraction (X_c') can be determined by deconvoluting the amorphous and microcrystalline contributions using the formula [Tsu et al., 1982]:

$$X_c' = \frac{I_c}{I_c + \sigma I_a} \tag{2.1}$$

where I_c corresponds to the microcrystalline contribution, located near 520 cm^{-1}, and I_a to the amorphous contributions centred around 480 cm^{-1}. Additional peaks centred around 500-510 cm^{-1} and 495 cm^{-1} are also considered by different groups in the microcrystalline contribution and attributed to very small grains and to grain boundaries, respectively [Han et al., 2000, Niikura et al., 2001, Finger et al., 2002]. The parameter σ is the cross section ratio for the Raman effect in a-Si:H and nc-Si:H and strongly depends on the crystallite size [Bustarret et al., 1988].

The parameter used in our case to evaluate the crystallinity of the samples is the so-called crystalline ratio or integrated crystalline fraction X_c,

$$X_c = \frac{I_{520}}{I_{520} + I_{480}} \tag{2.2}$$

which is simply the ratio of the integrated contributions at 520 and 480 cm^{-1}. This parameter is commonly used as an estimation of the real crystallinity. From now on, in order to facilitate comprehension, the denomination crystalline fraction will refer to X_c.

Transmission Electron Microscopy (TEM) measurements have also been carried out in several samples. Images presented in this work have been taken with a Philips CM30 microscope. High-resolution images allow the direct observation of the crystalline domains and the substrate-film interface region.

Surface roughness of nanocrystalline silicon and ZnO:Al samples has been evaluated from Atomic Force Microscopy (AFM) images taken with an AFM Nanoscope III-A microscope.

2.4.2. Compositional analysis

Oxygen and hydrogen content (C_O and C_H, respectively) in the samples has been determined from the infrared absorption peaks measured by Fourier Transform Infrared (FTIR) spectroscopy using a Nicolet 5ZDX spectrometer. C_H, the content of hydrogen bonded to Si, is estimated from the absorption band related to the Si-H wagging band, centred around 630 cm^{-1} following [Curtins and Veprek, 1986]:

$$C_H[\%at] = 3.2x10^{-2} \int_{band} \frac{\alpha(\omega)}{\omega} d\omega \tag{2.3}$$

The presence and further evolution of the double broad peak attributed to the stretching Si-O bands centred around 1100 cm^{-1} and 1220 cm^{-1} allows the study and estimate quantification of the oxidation of our samples [Curtins and Veprek, 1986]:

$$C_O[\%at] = 3.02x10^{-5} \int_{band} \frac{\alpha(\omega)}{\omega} d\omega \tag{2.4}$$

Additional compositional analysis was performed by Secondary Ion Mass Spectroscopy (SIMS). Depth profiles of silicon, doping atoms and contaminants, mainly oxygen incorporation, have been obtained with an ATOMIKA 3000-30 ion microprobe system by sputtering the samples with Ar or O ions and analysing the positive secondary ions.

2.4.3. Optical and electrical properties

Optical characterisation of nc-Si:H layers has been carried out by Photothermal Deflection Spectroscopy (PDS) and Optical Transmittance. The optical absorption coefficient (α) at every wavelength, the optical band gap (E_g) and the subgap defect density can be obtained from the treatment of the optical spectra. An accurate description of the PDS system, as well as of all optical and electrical characterisation systems and procedures and of device characterisation, briefly explained here, can be found in [Voz, 2001].

Two aluminium stripes have been evaporated onto the sample prior to electrical characterisation. The stripes are 1 cm long per 1 mm wide and 1 mm apart from each other. Dark conductivity at room temperature (σ_d) and activation energy (E_a) of the samples have been determined from the measure of resistance against temperature (R(T)) in vacuum in the range of 30-150ºC. The activation energy is used as an indication of the Fermi level position in the material and is determined from the thermal activated behaviour of conductivity:

$$\sigma = \sigma_0 \exp\left(-\frac{E_a}{k_B T}\right) \tag{2.5}$$

In the case of highly conductive samples like heavily doped nc-Si:H layers, conductivity of the layers as well as carrier mobility (μ) and carrier concentrations (N_A, N_D) have been obtained from Hall measurements using van der Paw's method.

The photoconductivity of a sample is the relative change in its electrical conductivity when it is illuminated. Photoconductivity (σ_{ph}) and the mobility-lifetime product of majority carriers ($\mu\tau$) have been determined by means of Steady State Photoconductivity (SSPC) measurements at a wavelength of 620 nm.

2.4.4. Device characterisation

Once a solar cell is deposited, the first measurement to characterise it is the J-V curve. This curve is obtained measuring the current density for different values of voltage applied. From a J-V curve, as shown in figure 2.8, the characteristic values of a solar cell are easily determined: the short circuit current density (J_{sc}), the open circuit voltage (V_{oc}), the efficiency (η) of the cell and its fill factor (FF). The latter are defined as:

$$\eta = \frac{P_{maximum\ power}}{P_{incident}} \ , \ FF = \frac{P_{mp}}{J_{sc} \cdot V_{oc}} = \frac{J_{mp} \cdot V_{mp}}{J_{sc} \cdot V_{oc}} \tag{2.6}$$

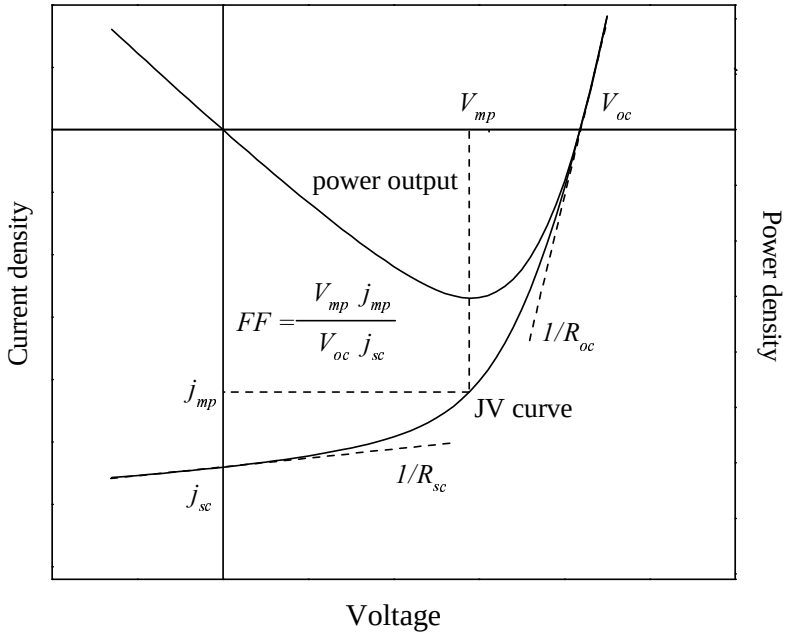

Fig. 2.8. Example of how the different parameters of a solar cell are evaluated from a J-V curve.

From the acquisition of J-V curves over a wide range of illumination levels, the so-called Variable Illumination Measurement technique (VIM) [Merten et al. 1998], the evolution of the characteristic parameters of the device (V_{oc}, FF, and the open circuit (R_{oc}) and short circuit (R_{sc}) resistances) are evaluated. Analysing these data, several technological and material-related effects that might affect the performance and the stability of the device can be deduced. A wider explanation of the information obtained from VIM measurements can be found in Annexe III of this thesis.

The spectral response of the device (i.e., for an external voltage applied, how much current in amperes is collected from the device per incident watt of light with wavelength λ) allows the calculation of the external quantum efficiency by measuring the current generated at different incident radiation wavelength. The external quantum efficiency, that is the fraction of incident photons of a given wavelength that results in an electron-hole pair collected at the contacts of the cell, is not only influenced by the collection efficiency but also by the optical optimisation of the device.

3. The search of a more chemically stable material

This chapter describes the strategies followed in order to improve the quality of our intrinsic nc-Si:H. First of all, several studies have been carried out with the different technological parameters, taking into account their effect on the material, in our search of dense and contaminant-free nc-Si:H. Special attention is paid to oxygen incorporation in our samples once they have been exposed to the atmosphere as an indication of their compactness. Finally, the inclusion of a protective funnel in the deposition chamber will be considered, taking into account the possible variations its implementation could cause in the optimised deposition conditions. In both cases, solar cells will be used to evaluate the stability of the material.

3.1. Initial approaches

After DLTS results mentioned in section 1.4, the internal heater was substituted for an external one, as the former was a potential source for the resolved Cu. Afterwards, several trials at different regimes of deposition conditions were carried out heading towards a material that did not oxidise and fulfilled all the requirements to be used in a solar cell. It is important to mention here that the wires used at this step of the research were still tungsten ones. Hence, we tried to select deposition conditions propitious for the achievement of our goal. Two trends that favour higher density are those enhancing either crystallinity or the mobility of precursors on the substrate. The latter was achieved by means of increasing the substrate temperature from 200 to 500ºC. Table 3.1 summarises the deposition conditions and some results of these samples. Even though the films obtained at such T_s showed almost no oxygen incorporation, their electrical features ($\mu\tau \sim 10^{-11}$ cm^2/V, as can be seen in fig. 3.1) made them absolutely useless to be implemented in a solar cell, evidencing that at 500ºC there was not enough H incorporated to appropriately passivate the grain boundaries.

On the other hand, crystallinity of the samples was enhanced by decreasing the total amount of gas flow while keeping the process pressure and the hydrogen dilution, i.e., the percentage of hydrogen in the total gas flow, constant at 90%. A decrease in the deposition rate at the same D_H causes a higher mobility of the precursors that might provoke the

growth of less porous material. Despite the higher crystalline fractions obtained, which can be seen in table 3.2, porosity among the grains was not avoided and the resulting layers still suffered from oxygen incorporation when exposed to air. This fact is evidenced in figure 3.2, where temporal evolution of the FTIR spectra of sample 990720i, the most crystalline one, is plotted.

Sample	T_s (ºC)	d (μm)	r_d (Å/s)	X_c	$\mu\tau$ (cm^2/V)	G_s (nm)
990720i	200	1.7	4.7	0.87	3.3×10^{-7}	49
990721i	400	1.7	4.7	0.82	7.5×10^{-9}	36
990722i	500	2.2	6.1	0.87	2.0×10^{-11}	29

Table 3.1. Summary of deposition conditions and properties of samples deposited with a 6-loop basket-shaped W filament at different substrate temperature. The rest of the deposition conditions were P = 10^{-1} mbar, T_f = 1650ºC, $\phi(H_2)$ = 9 sccm and $\phi(SiH_4)$ = 1 sccm. G_s corresponds to grain size in the (111) direction.

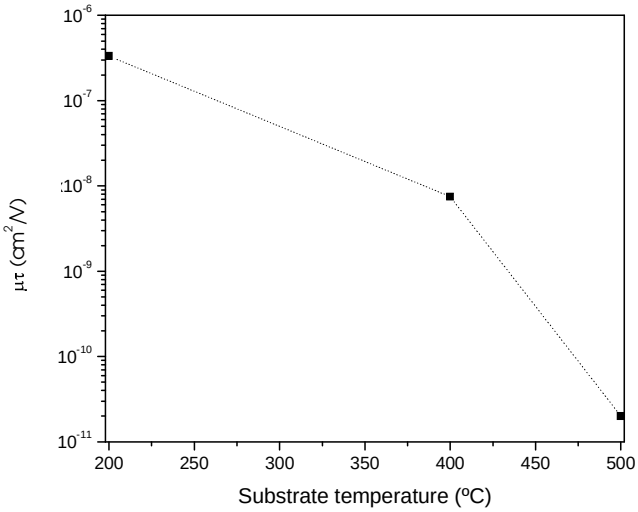

Fig. 3.1. $\mu\tau$ as a function of T_s for samples deposited using a W filament heated at 1650ºC. Process pressure was kept at 10^{-1} mbar and gas flows at 1 sccm of SiH_4 and 9 sccm of H_2.

Sample	$\phi(H_2)$ *(sccm)*	$\phi(SiH_4)$ *(sccm)*	*d (μm)*	r_d *(Å/s)*	X_c	$\mu\tau$ *(cm^2/V)*	G_s *(nm)*
990713i	36	4	3.2	17.8	0.53	$1.2x10^{-7}$	9
990719i	18	2	1.7	9.4	0.73	$2.2x10^{-7}$	24
990720i	9	1	1.7	4.7	0.87	$3.3x10^{-7}$	49

Table 3.2. Summary of deposition conditions and properties of samples deposited with a 6-loop basket-shaped W filament changing the total gas flow while keeping hydrogen dilution constant at 90%. The rest of the deposition conditions were P = 10^{-1} mbar, T_f = 1650ºC and T_s = 200ºC. G_s corresponds to grain size in the (111) direction.

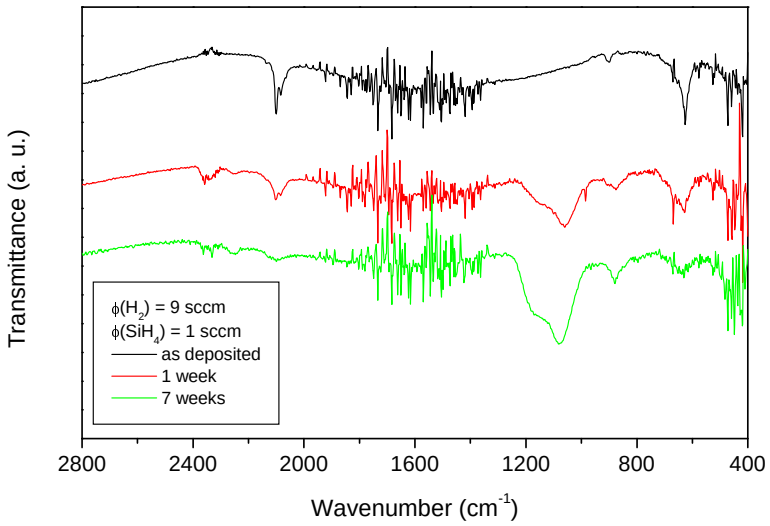

Fig. 3.2. Temporal evolution of FTIR spectrum of a sample deposited with the lowest total gas flow, 9 sccm of H_2 and 1 sccm of SiH_4. The rest of the deposition conditions considered were P = 10^{-1} mbar, T_s = 200ºC and T_f = 1650ºC.

Knowing that high filament temperatures enhance the incorporation of impurities [Voz, 2001], it was desirable to draw the deposition regime to low T_f. This fact was the key point to change the catalyst material to Ta, which is far less susceptible to silicide formation [Bauer et al., 1998] and, therefore, seemed to be more adequate to study the low filament temperature regime. Hence, all samples deposited from this point on were grown using a Ta wire as a catalyst. Thus, taking the low T_f conditions for W in [Voz, 2001] as a starting

point, a scan in the deposition parameters was performed aiming to obtain dense and device-quality nc-Si:H.

3.1.1. Hydrogen dilution

First of all, the evolution of crystalline fraction for different values of hydrogen dilution (D_H) was considered. This parameter is defined as the percentage of hydrogen in the total gas flow, i.e., $D_H = \phi(H_2)/(\phi(H_2)+\phi(SiH_4))$. Aiming to obtain a first approximation to the optimum value of D_H, several samples were deposited at T_f = 1650ºC, T_s = 200ºC and using a process pressure of $3x10^{-2}$ mbar. The change in D_H was carried out by varying the amount of hydrogen in the total gas flow while keeping the silane flow constant at 4 sccm. Figure 3.3 shows the Raman spectra measured for D_H = 90, 92.5 and 95% (36, 50 and 76 sccm of H_2, respectively). All three samples had thicknesses around 1 μm and the deposition rate decreased from 7 to 5 Å/s with increasing D_H.

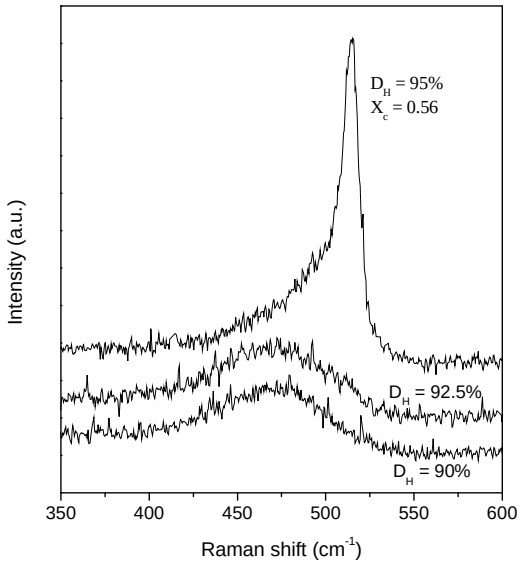

Fig. 3.3. Raman spectra of samples deposited at D_H = 90, 92.5 and 95% with a Ta wire. The rest of the technological parameters were T_f = 1650ºC, T_s = 200ºC and P = $3x10^{-2}$ mbar.

Analysing the Raman spectra it was clearly seen that, under these deposition conditions, the transition between amorphous and nanocrystalline growth abruptly took place somewhere between 92.5 and 95% hydrogen dilution. The crystalline fraction for the

highest dilution used was $X_c = 0.56$, indicating an important contribution of the amorphous phase. This value turned out to be a good starting point to optimise our material. Further on, slight changes in D_H around this point had to be done in order to optimise the intrinsic layer when to implement it into a solar cell.

3.1.2. Substrate temperature

Atomic hydrogen plays a critical role in grain boundary passivation in nc-Si:H. The substrate temperature is directly related with the amount of H incorporated into the layer. The FTIR spectra shown in figure 3.4 are an example of the dependence between T_s and C_H. There it can be seen that both the Si-H_x stretching band (2100 cm^{-1}) and the wagging band (630 cm^{-1}) diminished their intensity with increasing T_s, turning into a decrease in C_H from 4.6% at 200ºC to 2.9% at 500ºC. These layers were deposited in the same conditions (T_f = 1650ºC, P = 3.5x10^{-2} mbar and D_H = 95%) but the substrate temperature, and resulted in similar values of activation energy around midgap ($E_a \approx 0.5$ eV) and crystalline fraction values around 0.68.

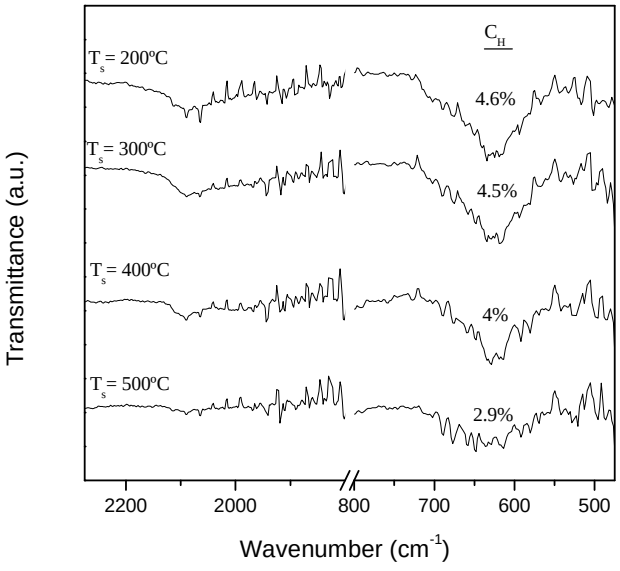

Fig. 3.4. FTIR spectra of samples deposited at different substrate temperatures. The evolution of the hydrogen content with T_s is also shown. The rest of the deposition parameters were T_f = 1650ºC, P = 3.5x10^{-2} mbar and D_H = 95%.

If we take into account the electronic transport properties of these samples by studying the trend of the μτ-product with decreasing T_s, an important change was found between 300 and 400ºC. In that 100-degree step, a drop from $1x10^{-7}$ to $4x10^{-8}$ cm^2/V took place, indicating that low substrate temperatures resulted in material more suitable to be used in a solar cell. In this case, as all layers had a clear intrinsic character ($E_a \approx 0.5$ eV), a decrease in the μτ-product could be associated with a decrease in the quality of the transport properties. Indeed, best values for the μτ-product, as shown in fig. 3.5, and a slightly better photoresponse (close to 10) were obtained at 200ºC. Similar behaviour has been reported by [Klein et al., 2001], concluding that device-quality nc-Si:H was obtained at T_s<300ºC, as for higher values of this deposition parameter enhanced hydrogen desorption during the growth process resulted in poor grain boundary passivation.

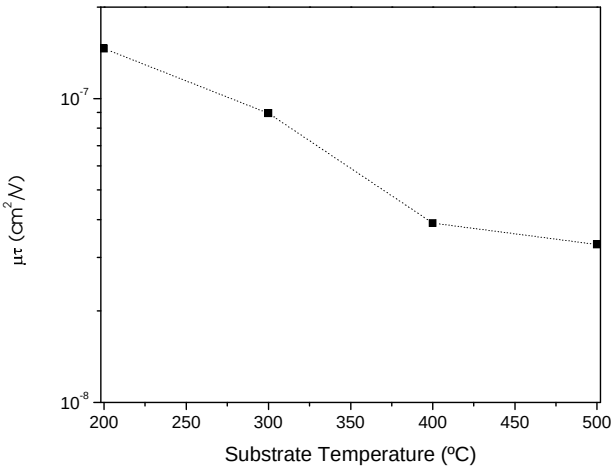

Fig. 3.5. μτ-product as a function of T_s for samples deposited at T_f = 1650ºC, P = $3.5x10^{-2}$ mbar and D_H = 95%.

3.2. The role of the filament

3.2.1. Structural properties

Since the species generated on the surface of the hot filament are highly dependent on its temperature, we have especially concentrated on the effects of this key parameter on the structure and chemical stability of the layers. With such an aim, a series of samples with

thicknesses around 1 μm at wire temperatures in the range 1500-1850ºC were deposited. The substrate temperature was kept at 200ºC and a process pressure of $3x10^{-2}$ mbar and a gas mixture of 4 sccm of SiH_4 and 76 sccm of H_2 (D_H = 95%) were used. It is important to mention that due to the geometry of our deposition chamber, a change in 300ºC in T_f did not affect the substrate temperature significantly. Without any additional substrate heating, the sample temperature reaches 150ºC with the filament geometry used (3-loop basket-shaped tantalum wire) at its maximum temperature. Deposition rate slightly increased with filament temperature from 2.3 Å/s at T_f = 1500ºC to 3.3 Å/s for filament temperatures above 1650ºC. Deposition conditions and some results from material characterisation are displayed in table 3.3.

Sample	T_f (ºC)	d (μm)	r_d (Å/s)	X_c	E_a (eV)	$\mu\tau$ (cm^2/V)
000626i	1850	1.00	2.8	0.73	0.62	$2.1x10^{-10}$
000622i	1800	1.20	3.3	0.77	0.68	$5.9x10^{-9}$
000615i	1750	1.15	3.2	0.73	0.64	$2.3x10^{-8}$
000607i	1700	1.20	3.3	0.82	0.57	$9.6x10^{-8}$
000608i	1650	1.20	3.3	0.77	0.53	$1.9x10^{-7}$
000616i	1600	0.90	2.5	0.73	0.54	$2.9x10^{-7}$
000619i	1550	0.85	2.4	0.77	0.54	$1.5x10^{-7}$
000623i	1500	0.80	2.3	0.73	0.54	$1.5x10^{-7}$

Table 3.3. Summary of different properties of samples grown at different Ta filament temperatures. P = $3x10^{-2}$ mbar, T_s = 200ºC and D_H = 95% were used in all cases.

Raman measurements of the films performed with the laser beam incident from the top side showed crystalline fraction values between 0.73 and 0.82 regardless T_f. Same measurements performed through the glass resulted in X_c values in the range of 0.70 indicating high crystallinity throughout the whole thickness of the layer.

Differences in the crystallographic preferential orientation were found at different T_f. XRD showed (220) crystalline preferential orientation for samples grown at low T_f (below 1650ºC). On the other hand, nc-Si:H layers obtained at T_f above 1700ºC exhibited (111) crystalline preferential orientation, as can be seen in fig. 3.6, where the spectra of the samples deposited at 1550 and 1800ºC are plotted.

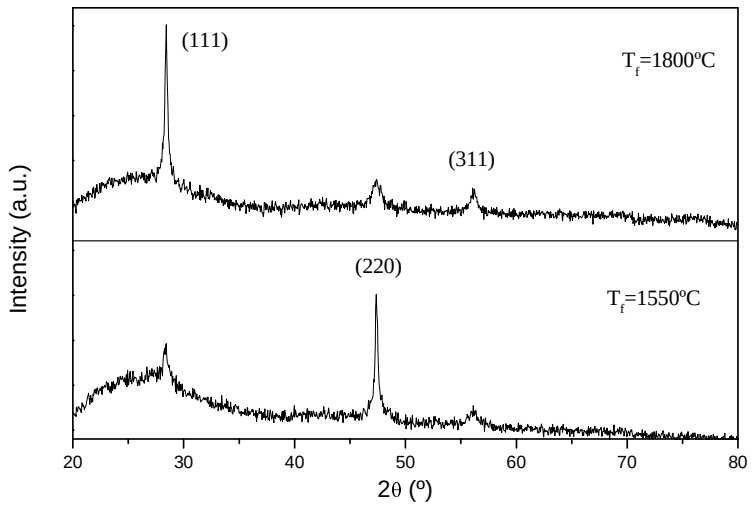

Fig. 3.6. XRD spectra of samples deposited at filament temperatures of 1800 and 1550ºC. P was $3x10^{-2}$ mbar, T_s = 200ºC and D_H = 95%.

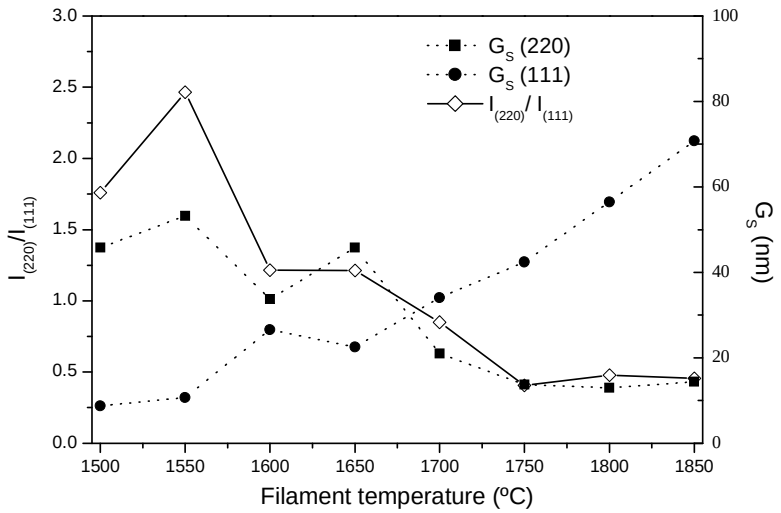

Fig. 3.7. Grain sizes in (111) and (220) crystalline preferential orientations and intensity ratio of crystalline orientations ($I_{(220)}/I_{(111)}$) as a function of the filament temperature.

The intensity ratio of crystalline orientations ($I_{(220)}/I_{(111)}$) had its maximum at 1550ºC, as can be observed in fig. 3.7. This figure also shows that grain size values obtained are in

agreement with the intensity ratio. (220) grain size decreased with increasing temperatures from 50 nm to values around 15 nm whereas (111) grain sizes increased from 10 nm at 1500ºC to 70 nm at 1850ºC. Even though a transition from (220) to (111) with increasing T_f had not been observed in samples deposited in our system with a similar W filament and similar deposition conditions, a similar behaviour has been reported for samples deposited with W wire under different deposition conditions [Guillet et al., 1998].

Whereas some (220) preferential growth was reported early with HWCVD in thick samples grown at higher temperatures (>350ºC) [Cifre et al., 1994], it is much more difficult to obtain this preferential growth in thinner samples at lower temperatures. Here, (220) crystalline preferential orientation has been obtained at low T_f in samples with thicknesses slightly lower than 1 μm using a Ta filament. This behaviour, which is reported in [Fonrodona et al., 2002], is different to the one observed with a W wire , where a minimum thickness of 1.5 μm seemed to be required in order to show (220) preferential orientation instead of (111) [Peiró, 1999].

Hydrogen content of the samples decreased as T_f increased, changing from values of C_H = 7% at 1500ºC to values of 3% at high filament temperatures. Activation energy values tended towards midgap for T_f < 1700ºC (E_a ~ 0.54 eV) and μτ-product values evolved from 10^{-7} cm^2/V in the samples having (220) preferential orientation to values unsuitable to be used in photovoltaic devices at high T_f, as shown in table 3.3.

3.2.2. Oxygen incorporation after deposition

Oxygen incorporated into the samples after several months of air exposure has been measured by means of FTIR and SIMS as an indication of their density. FTIR allowed the study of the degree of oxidation of the layers and its evolution with time. Figure 3.8 shows the Si-O bands measured three months after the deposition of the layers and there it can be seen that the average C_O diminished with decreasing T_f. Saturated C_O up to 18.5% were obtained after a long time air exposure for samples deposited at high T_f whereas values lower than 2% were obtained at T_f below 1600ºC. Further air exposure of the layers under illumination, which enhances the oxidation process and allows a faster reaching of the saturated oxygen content, did not enlarge the peak.

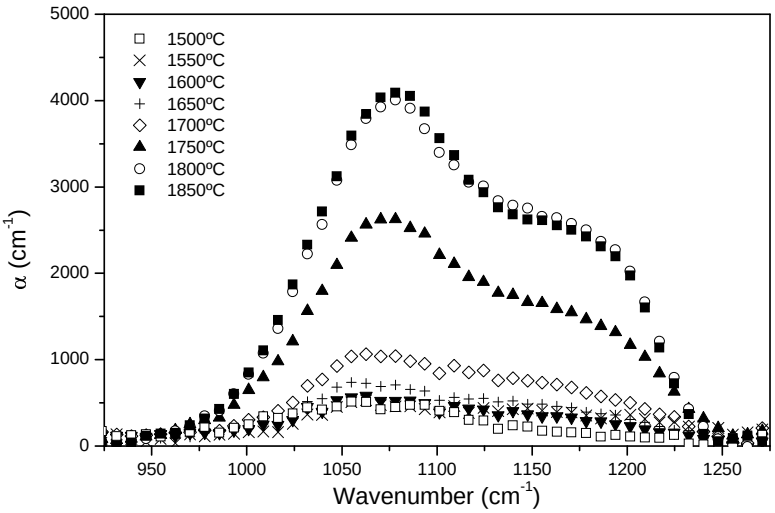

Fig. 3.8. Si-O absorption bands measured by FTIR three months after deposition for samples grown at filament temperatures between 1500 and 1850ºC.

The low value of the average oxygen content in the samples deposited at low T_f suggested a possible limitation of the oxidation process in these samples to a superficial layer. This hypothesis was investigated by performing SIMS measurements to two representative samples. Those grown at 1550 and 1800ºC were chosen. The oxygen compositional profiles obtained half a year and a year after deposition of the samples are represented in figure 3.9. Sample grown at 1800ºC showed a uniform oxygen content from the top of the sample to the sample-substrate interface. The amount of oxygen incorporated into the sample deposited at 1550ºC decreased as we approached the substrate from a value close to $10^{20}cm^{-3}$ at the top of the sample to a value of $4x10^{18}$ cm^{-3} near the interface, with an almost constant concentration around $6x10^{18}$ cm^{-3} inside the film. The SIMS depth profile clearly showed that oxygen incorporation in this case was limited to a more superficial layer. A constant oxygen concentration of about $3x10^{18}$ cm^{-3} inside the film has been reported for device-quality compact nc-Si:H deposited by HWCVD at moderately high substrate temperatures [Schropp et al., 2001]. The bulk value of oxygen concentration reported for microcrystalline silicon deposited by VHF CVD is $2x10^{18}$ cm^{-3}. It is worth mentioning that the ratio of C_O between both samples calculated from the FTIR spectra was in agreement with the ratio of integrated oxygen concentration measured from SIMS depth profiles.

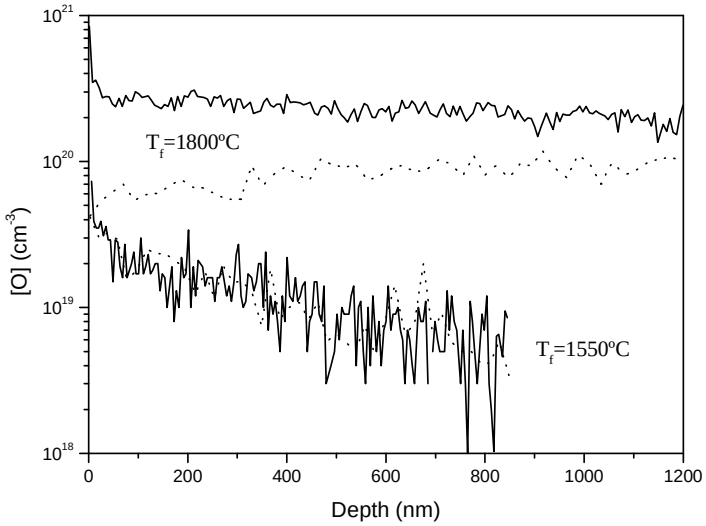

Fig. 3.9. Oxygen concentration depth profiles measured by SIMS for samples deposited at 1550ºC and 1800ºC. Dotted lines correspond to measures performed half a year after the deposition of the samples and straight lines to those carried out a year after the deposition.

SIMS measurements carried out one year after deposition showed that the amount of oxygen incorporated into the film grown at 1550ºC had not changed whereas the oxygen content in that deposited at 1800ºC was still uniform but had increased from 10^{20} cm^{-3} to $2x10^{20}$ cm^{-3}.

Oxidation results up to now suggested that films grown at low T_f had denser tissue among grain boundaries that prevented it from post-oxidation. In order to characterise this material more thoroughly, TEM and high-resolution TEM (HRTEM) measurements of the sample at 1550ºC were performed. Columnar grains in the direction of growth, like the one in fig. 3.10, were observed. Contrary to what has been reported for compact nc-Si:H deposited using a W filament and at higher substrate temperatures, these grains did not present an inverted conic shape [Rath and Schropp, 2000] but were more parallel in the vertical direction. TEM cross-sections showed that the sample had a superficial roughness of around 15 nm, in agreement with AFM rms roughness (fig. 3.11). HRTEM photographs pointed out the presence of crystalline domains very near the substrate (30 Å), indicating that crystalline growth took place from the very first formation stages.

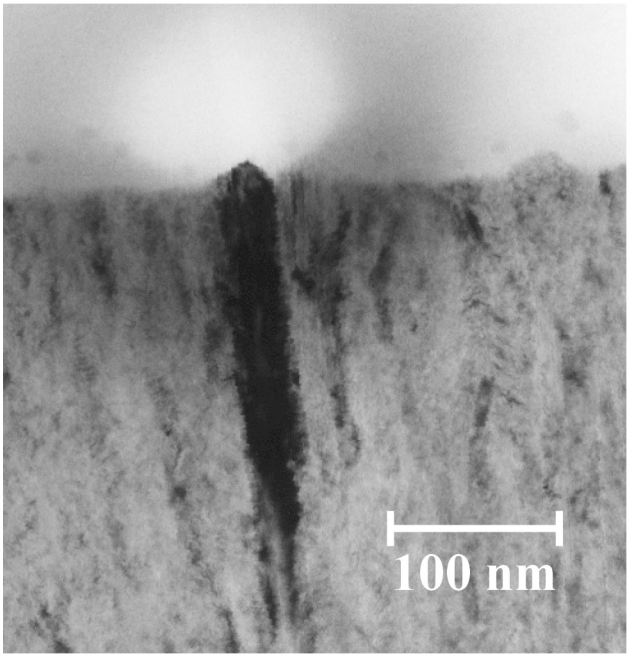

Fig. 3.10. TEM image of one of the crystalline grains observed in the sample deposited at T_f = 1550ºC.

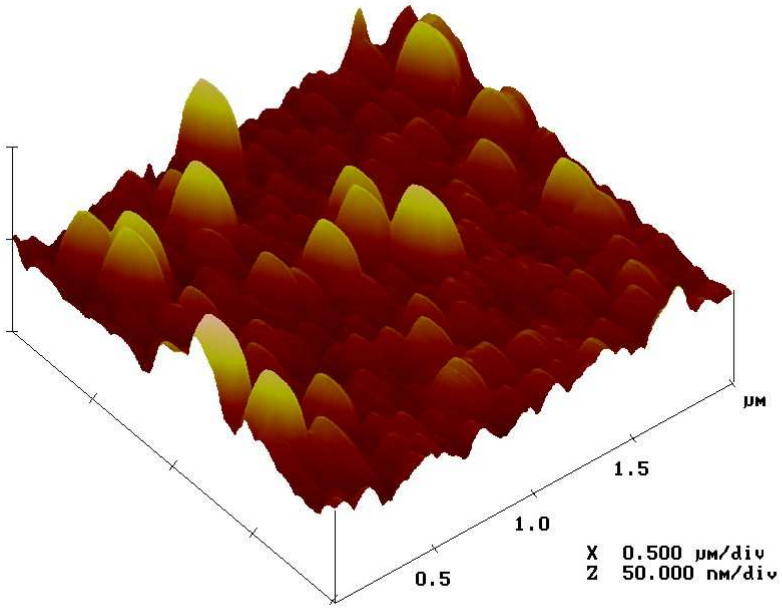

Fig. 3.11. AFM image of the sample grown at 1550ºC. An rms roughness of approximately 15 nm was deduced from these images.

Planar view images showed a wide distribution of grain sizes between a few and 100 nm, even though the majority of grains had sizes between 10 and 30 nm. Fig. 3.12 shows a planar view TEM image where grains surrounded by white lines can be seen. These lines, which are clearly observable in the double magnification image in the upper right part of the figure, correspond to areas having a lower density than the crystalline grains [He et al., 1998], which can be attributed to an amorphous tissue surrounding the grains.

In the samples presented here, the results observed could be due to differences in SiH_4 dissociation at the filament. As reported recently [Pant et al., 2001], the mole fraction of SiH_4 not being decomposed by a tantalum filament decreases with increasing T_f. This means that at a lower T_f there is more SiH_4 left for being consumed in the reaction $SiH_4 + H \rightarrow SiH_3 + H_2$ and, therefore, that more SiH_3 is produced at low temperature. This radical is considered to be the main precursor for the growth of dense a-Si:H and nc-Si:H in PECVD and is likely to provoke that material grown in the adequate conditions (low T_f in this case) has a dense tissue surrounding grain boundaries.

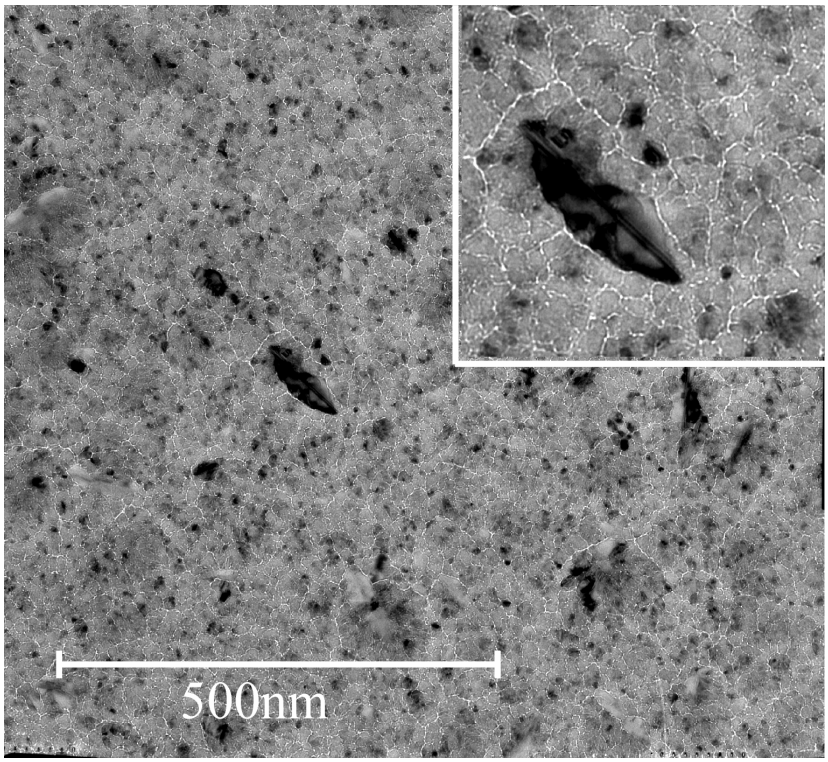

Fig. 3.12. TEM planar view image of the sample deposited at 1550ºC. The inset shows a double magnification image.

The resistance of compact device-quality nc-Si:H obtained using a W filament to oxidation [Schropp et al., 2001] was due to the coalescence of conical grains in the growth direction. This kind of structure has as a result a surface with no amorphous tissue among the grains and, therefore, without paths for oxygen to enter the film. Columns observed here were parallel in the vertical direction and did not reach coalescence. This fact, together with the low and superficial degree of oxidation achieved by samples grown at low T_f after a long exposure to air, suggested the presence of a more compact tissue among grain boundaries. On the other hand, the dramatic oxidation observed in layers deposited at high T_f from the top to the substrate-sample interface could be attributed to the porosity of the material between grain boundaries. The higher density of the nc-Si:H grown at 1550ºC was in agreement with the above-mentioned consequences a high production of SiH_3 at low T_f would have.

3.2.3. Application to solar cell

The following step to test low T_f nc-Si:H (~1550ºC) was its implementation into a solar cell. A 1.5μm-thick layer was used as active layer of a p-i-n solar cell. The structure of the whole device was glass/ZnO:Al/p-i-n/Cr-Al, where the doped layers were also deposited by HWCVD. No texture of the front TCO, back reflector or any structure to enhance light trapping were used. The resulting cell, whose J-V curve can be seen in fig. 3.13, had a V_{oc} of 0.41V and J_{sc} = 7.1 mA/cm^2. Even though the initial output features of this cell were lower than the best ones previously obtained in our laboratory [Voz, 2001], from the low degree of oxidation measured in the intrinsic samples one would expect it to outlast the former ones. The J-V curve of the same cell after 18 months of air exposure is also shown in the same figure, as well as the initial and degraded state of a cell deposited using a W filament, evidencing the expected longer life of the Ta cell attributable to its higher density. The curves corresponding to the cell deposited with W prove the damaging effects of air exposure to the conversion efficiency of a porous solar cell.

J-V measures performed to the Ta cell throughout more than 500 days showed a decrease of J_{sc} and V_{oc} to 4.2 mA/cm^2 and 0.32 V during the first month, remaining then almost constant for the rest of the measure. These values correspond to a poor conversion

efficiency but were a symptom of the higher density and, therefore, superior resistance to oxidation of nc-Si:H deposited at low T_f. Figure 3.14 shows the temporal evolution of J_{sc} and V_{oc} for the Ta cell (b) and from one of the W cells in [Voz, 2001] (a) represented in fig. 3.13. These W cells, despite having higher initial values of J_{sc} (12 mA/cm^2 for the cell in fig. 3.14 (a)), were completely degraded after several weeks, as shown previously in fig. 3.13.

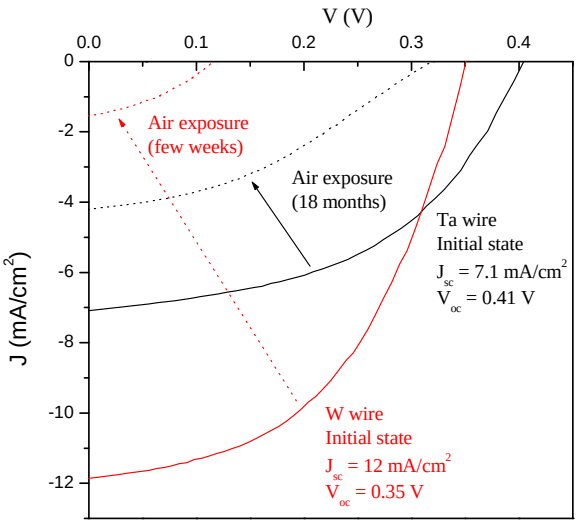

Fig. 3.13. J-V characteristics of p-i-n solar cells deposited with Ta and W wires. Straight lines correspond to their initial state whereas dotted curves represent their state after air exposure.

In spite of the long life –compared to our previous devices- achieved by the solar cell deposited at T_f = 1550ºC, the J_{sc} value obtained was too low. This fact clearly seemed to be an effect of the screening of the internal field due to the incorporation of contaminants during deposition [Voz et al., 2000]. The relatively low deposition rate of these samples, which enhances the incorporation of impurities during growth, was in agreement with this misbehaviour. Thus, further strategies to avoid the undesirable incorporation of contaminants, additional to the change in heater type and catalyst material, should be the next step in our research. On one hand, the inclusion of a shield that protected the gas flow and the substrate from possible impurities coming from inside the chamber will be considered in the next section. On the other hand, a completely different strategy consisting in silicon deposition from secondary reactions between silane and atomic hydrogen will be considered in Annexe II.

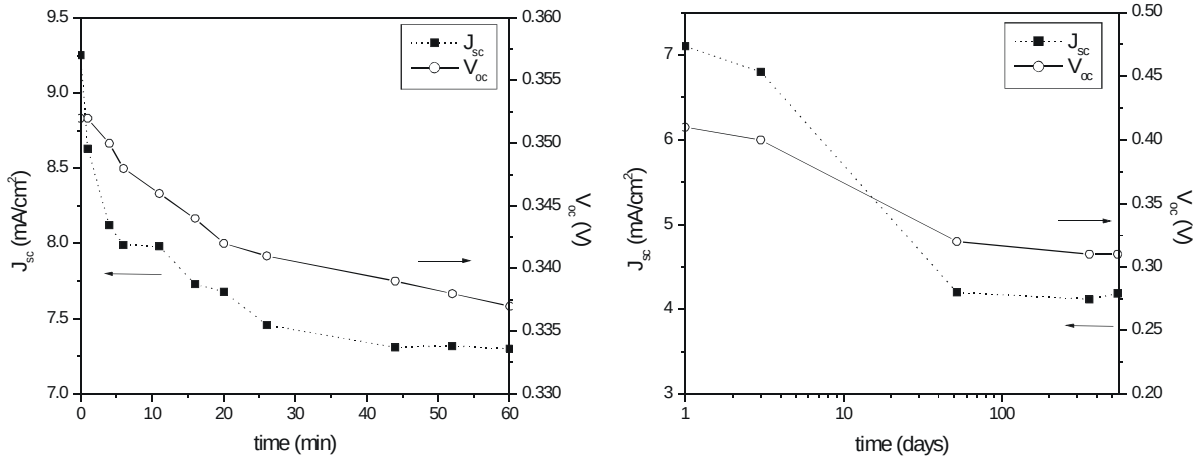

(a) (b)

Fig. 3.14. Temporal evolution of J_{sc} and V_{oc} of a cell deposited with W wire at moderately high T_f (a) and of cell represented in fig. 3.10, i.e., deposited with Ta wire at low T_f (b).

3.3. The protective funnel

Results presented in the previous section, despite showing a clear improvement regarding material oxidation, still evidenced several effects imputable to the incorporation of contaminants during growth. Thus, the origin of these impurities should be located somewhere inside the deposition chamber, like the walls or the wire itself. Aiming to prevent the incoming gas flow or the dissociated species from being in contact with the potential sources of impurities, the protective funnel described in section 2.2.2 was implemented to our set-up. The design of the funnel [Fig. 2.5] induced a change in the filament geometry towards the use of a linear wire instead of a basket-shaped one, resulting in a decrease of the deposition rate due to the diminution of the effective wire surface.

3.3.1. O incorporation during growth

After the funnel implementation into the chamber where the intrinsic material is grown, together with a new linear Ta wire, three a-Si:H samples were deposited under exactly the same conditions in order to investigate not only impurity incorporation but also any possible side effect due to filament aging or funnel dirtying after several depositions. All

three samples were deposited at T_f ~ 1600ºC, T_s = 200ºC, D_H = 92.5% and P = 3x10^{-2} mbar, and were directly transferred to the SIMS system right after deposition with an air break as brief as possible. Deposition rate was 1.2 Å/s. Figure 3.15 shows the Si and O SIMS depth profiles of the three samples. It is seen that oxygen was, in all cases, at the detection limit of our system throughout the whole layer. These few counts per second, calibrated using a wafer with a known oxygen concentration (C_O = 2x10^{18} cm^{-3}), corresponded to a concentration of 3x10^{18} cm^{-3}. Thus, we could consider that the amount of impurities incorporated into the films had been drastically reduced by including the shielding funnel. Moreover, no side effects attributable to wire aging or funnel dirtying were detected, as further characterisation of the samples gave identical results in the three cases. Figure 3.16, showing the FTIR spectra of the layers, has been included as an example of this last statement.

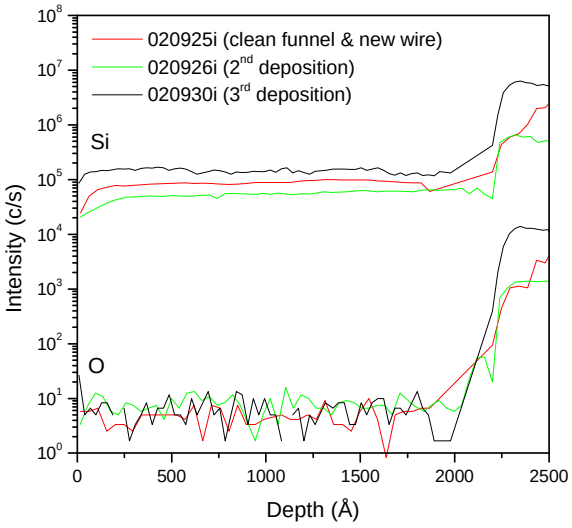

Fig. 3.15. Si and O SIMS depth profiles of three samples deposited under the same deposition conditions (T_f ~ 1600ºC, T_s = 200ºC, D_H = 92.5% and P = 3x10^{-2} mbar).

The parameter $C_O \cdot r_d$ gives information about the amount of oxygen atoms reaching the substrate per unit of area and time. When the amount of atoms reaching the substrate per unit of area and time is high, less oxygen is incorporated during growth if the deposition rate is increased, as the deposition time is lessened [Voz, 2001]. After the inclusion of the funnel, despite the low deposition rates obtained, oxygen incorporation was drastically diminished. Therefore, it seemed to indicate that after the implementation of the funnel, the amount of oxygen atoms per unit of area and time reaching the substrate had decreased.

Despite the low deposition rate and assuming that all oxygen atoms are incorporated into the layer, the number of oxygen atoms reaching the substrate was $3.6x10^{10}$ atoms/cm^2·s, which is clearly lower than the impingement ratio in ultra-high vacuum specifications ($<10^{13}$ atoms/cm^2·s).

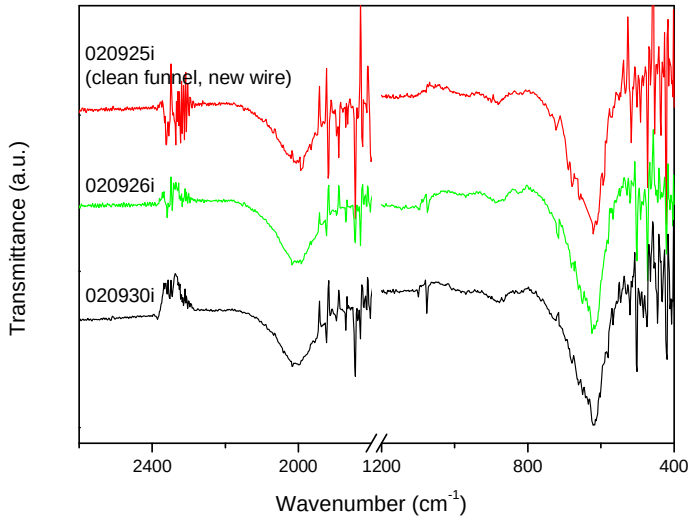

Fig. 3.16. FTIR spectra of the samples in fig. 3.15.

3.3.2. Effect of the process pressure

The possibility that the inclusion of the funnel might have somehow changed the optimal deposition conditions drove us to check the effect a slight variation in some of the parameters would have in the resulting samples. Firstly, process pressure values between $3x10^{-2}$ and $1x10^{-1}$ mbar were selected while maintaining the rest of the parameters in the "standard" values (T_s = 200ºC, T_f ~ 1600ºC, D_H = 95%). Such increase in P resulted in an increment in the deposition rate from 1.1 Å/s at the lowest pressure to 2.8 Å/s at 10^{-1} mbar. Raman spectra [Fig. 3.17] evidenced a decrease in the crystalline fraction when P was incremented, leading to an entirely amorphous sample at P = $1x10^{-1}$ mbar. Crystalline fraction values measured in this case (X_c = 0.56 and 0.41 for P = $3.0x10^{-2}$ and $5.7x10^{-2}$ mbar, respectively) were slightly lower than the ones obtained at similar deposition conditions with a basket-shaped wire without the funnel (X_c = 0.73 and 0.57, respectively for the considered process pressures). This difference might be a consequence of the

reduction of the effective catalytic area resulting from the change from three loops to a lineal filament useful only inside the funnel.

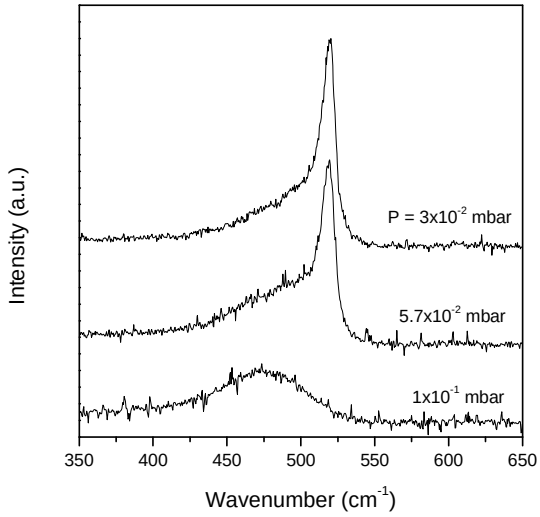

Fig. 3.17. Raman spectra of nc-Si:H samples deposited at different process pressures. The rest of the deposition parameters were T_s = 200ºC, T_f ~ 1600ºC and D_H = 95%.

A summary of the results of the different characterisation techniques is presented in table 3.4. Sample deposited at $1x10^{-1}$ mbar showed clearly amorphous features, whereas a comparison between the two nanocrystalline films seemed to point out slightly better properties at $5.7x10^{-2}$ mbar, where the lowest crystalline fraction is measured. This trend was in agreement with last results stating that better conversion efficiencies are achieved in nc-Si:H solar cells made with material grown near the transition to a-Si:H [Klein et al., 2002].

Sample	*P (mbar)*	*d (μm)*	r_d *(Å/s)*	E_g *(eV)*	$\mu\tau$ *(cm^2/V)*	X_c	G_s *(nm)*
011126i	$3.0x10^{-2}$	0.4	1.1	1.19	$2.0x10^{-6}$	0.56	18
011128i	$5.7x10^{-2}$	0.7	1.9	1.12	$1.8x10^{-6}$	0.41	36
011129i	$1.0x10^{-1}$	1	2.8	1.73	$4.2x10^{-8}$	0	0

Table 3.4. Summary of the main electrical, optical and structural properties of samples deposited at different pressure. The rest of the deposition conditions were kept constant at T_f = 1600ºC, T_s = 200ºC and D_H = 95%.

FTIR measures performed nine months after deposition showed that, despite having better properties, the layer grown at the intermediate pressure regime was a bit porous as a Si-O peak (~ 1100 cm^{-1}) evidencing post-deposition oxygen incorporation was observed. The FTIR spectra of the films are plotted in figure 3.18, were no traces of Si-O bands are detected in the cases of a-Si:H and nc-Si:H deposited at $3x10^{-2}$ mbar.

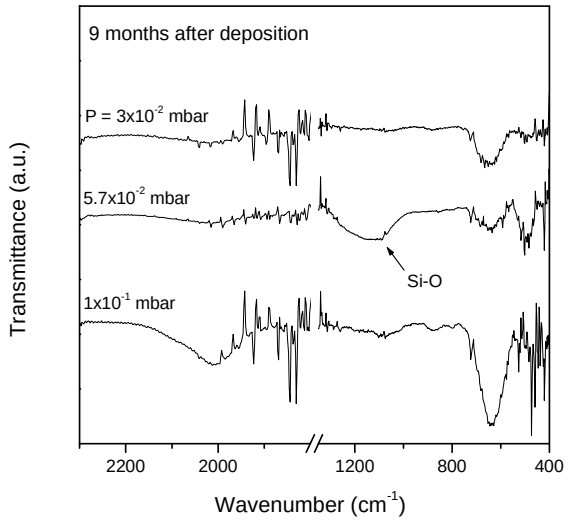

Fig. 3.18. FTIR spectra of samples described in table 3.4 obtained nine months after deposition.

3.3.3. Effect of the hydrogen dilution

Since best material properties and, therefore, best device efficiencies are found near the transition to a-Si:H, a set of samples were deposited in a narrow range of hydrogen dilutions close to that critical point, aiming to the further incorporation of some of these layers into solar cells. D_H was tuned by changing the silane flow between 4 and 7 sccm, while keeping the hydrogen flow at 76 sccm (D_H = 91.6-95%). The evolution of the crystalline fraction with D_H can be seen in the Raman spectra plotted in figure 3.19, where it was seen that, under the present deposition conditions, the transition took place somewhere between D_H = 93.5% and 92.5 %.

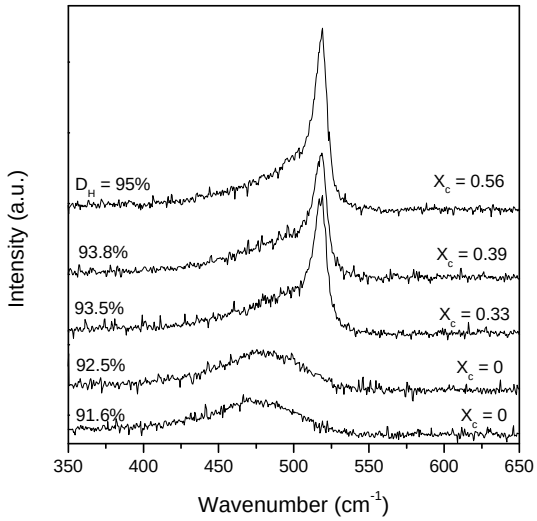

Fig. 3.19. Raman spectra of samples deposited at different hydrogen to silane ratios. The rest of the process parameters were T_f = 1600ºC, T_s = 200ºC and P = $3x10^{-2}$ mbar.

The transition from nc-Si:H to a-Si:H caused by decreasing the hydrogen to silane ratio was also observable by FTIR as a shift towards a sole Si-H_x stretching band centred at 2000 cm^{-1} in the case of entirely amorphous material. Contrary to that, as shown in fig. 3.20, nanocrystalline layers also presented a contribution around 2100 cm^{-1}. FTIR measurements carried out several weeks after deposition showed no trace of oxygen incorporation in any case, in agreement with what expected under the selected deposition conditions.

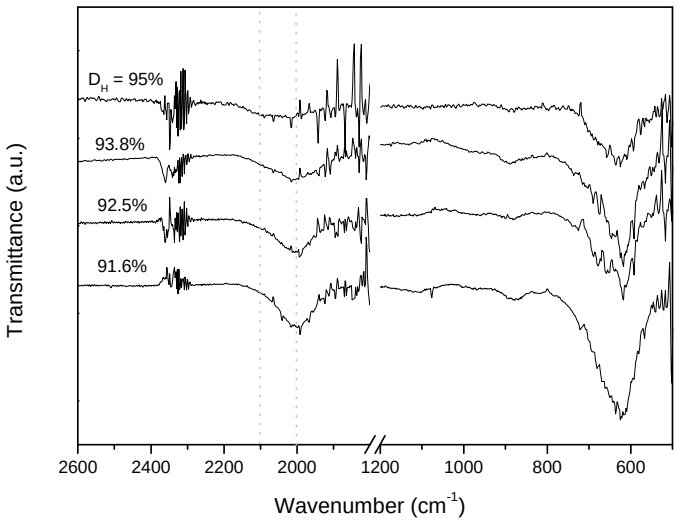

Fig. 3.20. FTIR spectra of samples deposited at different D_H.

3.3.4. Essay on a solar cell

Once intrinsic nc-Si:H deposited after the funnel implementation had been studied, next step was to make a solar cell attempt. The chosen material, taking into consideration its initial properties and the deposition rate, was that described in section 3.3.2. deposited at a process pressure of $5.7x10^{-2}$ mbar. Traces of oxidation in that intrinsic sample deposited at this pressure, and previously shown in fig. 3.18, were not observed until several months after the choice of the material to be used in the first solar cell attempt. When comparing the properties of samples deposited at $3.0x10^{-2}$ and $5.7x10^{-2}$ mbar listed in table 3.4, the main reason to choose the latter was the higher deposition rate, i.e. less time needed to deposit the cell.

The solar cell structure chosen was p-i-n, grown onto ZnO:Al coated glass. No texture of the front TCO, back reflector –the back contact was Cr-Al– or any structure to enhance light trapping were used. Doped layers used in this case were still not optimised and thick (~1000Å). The J-V curve and the initial features of the cell are shown in figure 3.21. These initial cell values were a bit lower than those in the cell presented in section 3.2.3. Despite this difference, the reduction of the contaminants in the device caused by the inclusion of the funnel in the set-up should lead to a higher stability in the cell studied here.

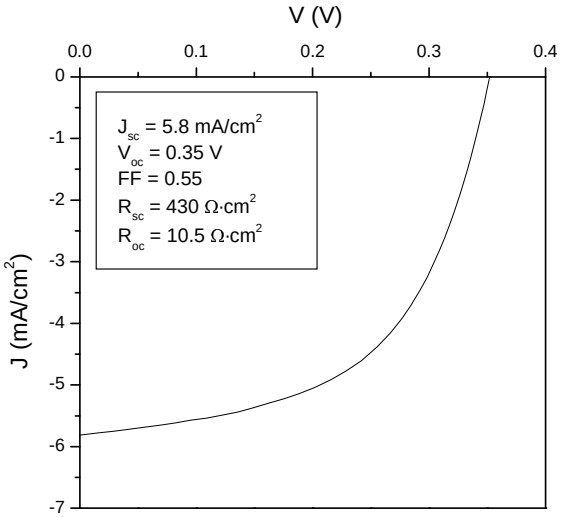

Fig. 3.21. J-V curve of a nc-Si:H solar cell incorporating an i-layer deposited after the implementation of the protective funnel. The inset shows the parameters of the device measured under AM1.5 illumination. No light trapping strategy was used in the deposition of this cell.

The stability of the solar cell was evaluated by means of VIM. This technique allows the study of the evolution of the characteristic parameters of the device from the measure of J-V curves over a wide range of illumination levels [Merten et al., 1998]. From the V_{oc}, FF, R_{sc} and R_{oc} curves obtained as a function of J_{sc}, several technological and material-related effects that affect the performance of the cell can be deduced.

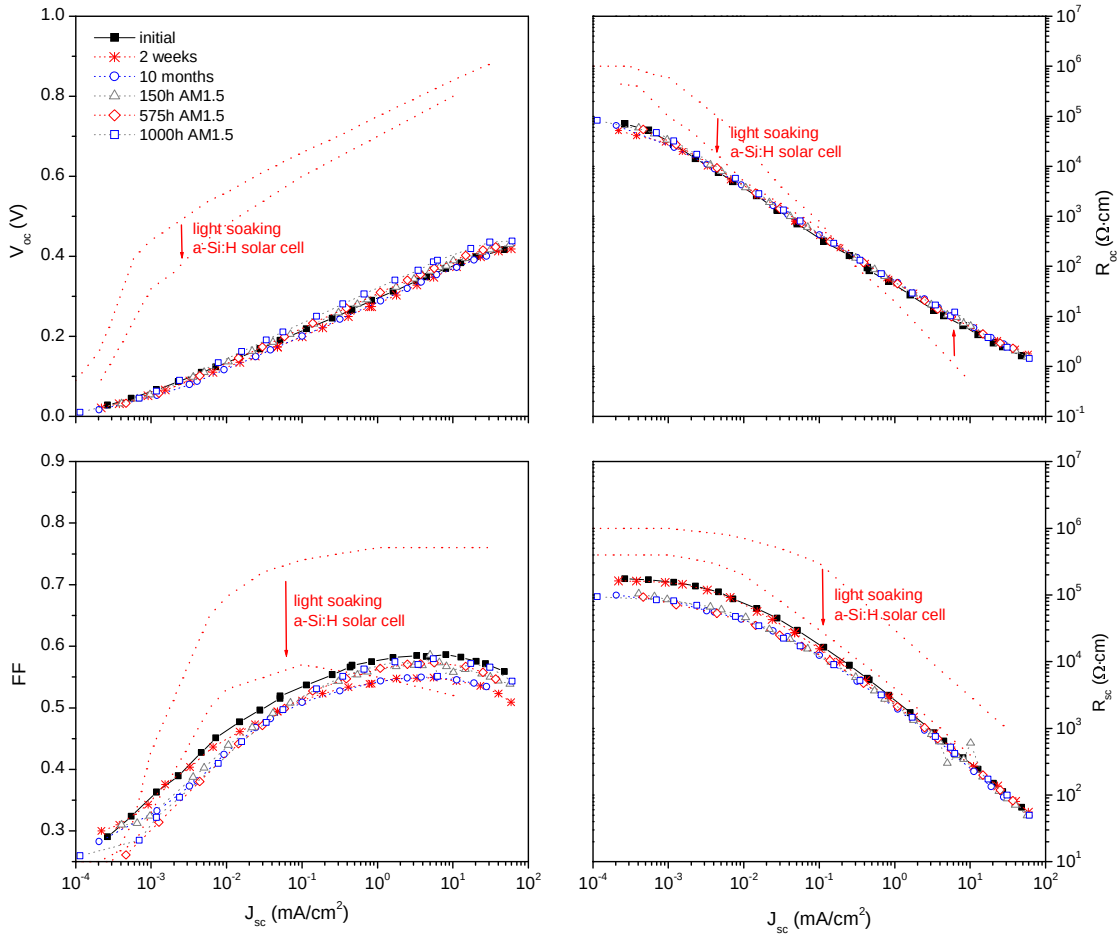

Fig. 3.22. VIM measurements at different steps of light soaking of a nc-Si:H solar cell with $X_c = 0.51$. Dotted lines illustrate the degradation effects suffered when an a-Si:H solar cell is exposed to illumination (extracted from [Merten et al., 1998]).

Figure 3.22 shows VIM measurements performed to the solar cell in fig. 3.21 right after deposition, ten months after deposition and at different stages during 1000 hours of AM1.5 illumination (100 mW/cm^2). Crystalline fraction deduced from the Raman spectrum was

X_c = 0.51. Results after 1000 hours of light soaking evidenced almost no degradation of the device, i.e., no significant traces of Staebler-Wronski defect creation were seen despite the important amorphous fraction present in the i-layer. A small change, unrelated with illumination, could be observed in R_{sc} in the low illumination regime, i.e., in the parallel resistance, R_p. This decrease was in agreement with an increase in the lateral leakage currents in the device. Such effect could be avoided by chemically etching the cell.

Summarising, the inclusion of a protective funnel in the set-up has led to a clear reduction in the amount of impurities incorporated to intrinsic nc-Si:H during growth. This fact has been evidenced after the inclusion of such material in a solar cell. Comparison between VIM results in figure 3.22, where no degradation attributable to problems inside the i-layer were observed after several months in dark and 1000 hours of AM1.5 illumination, with the J-V curve in figure 3.13, where degradation imputable to the presence of contaminants was observed, clearly illustrated the improvement caused by the inclusion of the funnel.

4. Substrate influence and doped layers

In this chapter, the effect of the nature of the substrate on which thin film silicon layers are grown on their microstructure will be considered. First of all, the effect of hydrogen dilution on the crystallinity of intrinsic samples deposited on glass will be studied, as well as the dependence of the crystallinity threshold on the kind of substrate used (glass, c-Si, ZnO:Al coated glass and stainless steel). Further on, the conclusions reached concerning intrinsic material will be validated in the case of doped material, the one actually grown onto a foreign substrate regardless the device configuration. Finally, most suitable doped layers will be scaled to device size while keeping good electrical properties.

4.1. Introduction

After many years focusing in the research of nc-Si:H with a very high crystalline fraction, recent results have drawn attention to that grown near the transition to a-Si:H, both using PECVD [Meier et al., 2001] and HWCVD [Niikura et al., 2002], leading to conversion efficiencies up to 9.4% [Klein et al., 2002].

The microstructure of thin layers can be considerably influenced by small changes in the deposition parameters. This fact turns to be especially critical when working in the region where the passage from nc-Si:H to a-Si:H takes place. Such transition can be provoked by appropriately varying one of the deposition parameters like the process pressure [Zhu et al., 2000], the filament temperature [Martins et al., 1998, Soler et al., 2001] or the substrate temperature [Alpuim et al., 1999]. Among all the process conditions that can cause the above-mentioned transition, the hydrogen dilution is probably the most delicate, as a very slight variation in the silane to hydrogen ratio can cause a transition from a-Si:H to nc-Si:H growth. This trend has been observed for both PECVD [Vallat-Sauvain et al., 2000] and HWCVD [Brüggemann et al., 2000] techniques.

Different solar cell configurations (p-i-n/n-i-p) require nanocrystalline growth on different kind of substrates. p-i-n cells (superstrate configuration) are usually deposited onto TCO, generally aluminium-doped zinc oxide (ZnO:Al), being the most common structure glass/ZnO:Al/p-i-n/metal. On the other hand, solar cells with n-i-p (substrate) configuration are usually grown onto a metallic substrate (stainless steel, silver), resulting

in metal/n-i-p/TCO architecture. The need of nanocrystalline growth on different substrates has led to the study of the effects of their nature on the properties of the material obtained. Substrate-dependent differences in the crystalline structure of thin film silicon layers deposited by PECVD [Kondo et al., 1996, Bailat et al., 2002] and by the layer-by-layer technique [Roca et al., 1995] have been reported. Though, results obtained from material characterisation directly on glass should not be straightforwardly extrapolated to devices deposited on other substrates.

4.2. Intrinsic material

4.2.1. Glass as substrate. Effect of D_H

Even though solar cells are never directly deposited on a glass substrate -but on a TCO layer or a metal-, single layers used to evaluate the properties of the material and its suitability usually are. This means that it is a common practice to automatically transfer the results obtained from material characterisation on glass to devices deposited on other substrate taking for granted that there would be no substantial differences between both cases.

A series of samples at different hydrogen dilutions have been deposited on glass substrates (Corning 1737) in order to evaluate the dependence of the crystallinity of the samples with this parameter. This study took place before the implementation of the protective funnel described in the previous section. Therefore, filament geometry used was 3-loop inverted basket. Selected deposition conditions were T_f = 1650ºC, T_s = 200ºC, P = $3x10^{-2}$ mbar and 4 sccm of silane. Hydrogen dilutions between 75 and 95% have been selected by appropriately tuning the amount of hydrogen entering the system. Deposition rate decreased as the amount of hydrogen in the chamber increased, diminishing from values of 8.9 Å/s (D_H = 75%) to 5.0 Å/s (D_H = 95%). Deposition parameters, together with crystalline fraction values obtained are listed in table 4.1. Raman measurements showed only measurable crystalline contribution at D_H = 95% (X_c = 0.56). As shown in figure 4.1, no sign of crystalline peak centred at 520 cm^{-1} was detected at $D_H \leq 92.5\%$, only the broad peak around 480 cm^{-1} corresponding to the amorphous contribution.

Sample	D_H (%)	d (μm)	r_d (Å/s)	X_c
010912i	75	1.6	8.9	0
010917i	85	1.1	7.3	0
010918i	90	1.3	7.2	0
010920i	92.5	0.9	5.0	0
010919i	95	0.9	5.0	0.56

Table 4.1. Deposition parameters and crystalline fraction of samples deposited on glass at different values of hydrogen dilution. The rest of the parameters were T_f = 1650ºC, T_s = 200ºC, P = $3x10^{-2}$ mbar and $\phi(SiH_4)$ = 4 sccm.

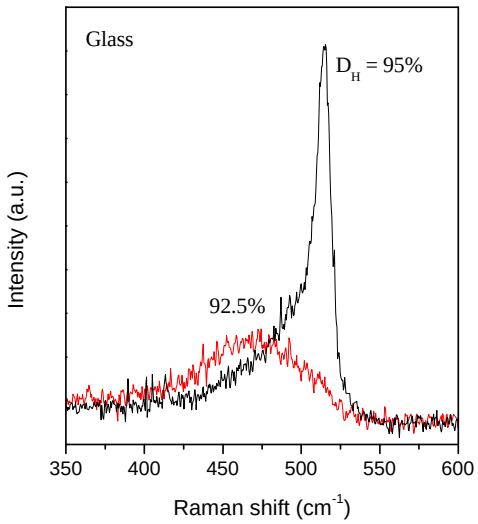

Fig. 4.1. Raman spectra of samples grown at different hydrogen dilutions at P = $3x10^{-2}$ mbar, T_f = 1650ºC and T_s = 200ºC. D_H = 95% seemed to be necessary to obtain nanocrystalline growth.

The steepness of the transition from amorphous to nanocrystalline growth has been verified for two different filament geometries keeping the deposition conditions constant. In figure 4.2, the calculated crystalline fractions for the above-considered series, deposited using a 3-loop basket Ta filament, as well as the ones obtained using a linear Ta wire are displayed. From this figure we could conclude that the transition from a-Si:H to nanocrystalline growth takes place in a very narrow range of D_H values.

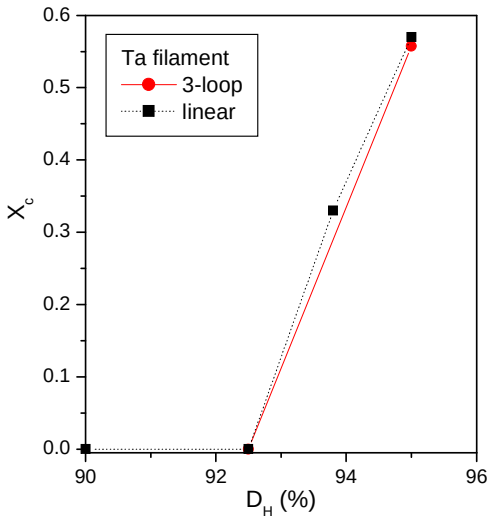

Fig. 4.2. Crystalline fraction as a function of D_H for different Ta filament geometry.

4.2.2. Substrate dependence

Samples deposited at different hydrogen dilutions were not only deposited on glass substrates but on silicon, stainless steel (SS) and ZnO:Al coated glass at the same time aiming to elucidate the possible effects of the nature of the substrate on which the layers are grown had on their microstructure. By depositing on the four different substrates during the same process, identical deposition conditions in all cases were ensured. Therefore, discrepancies measured could be only attributed to effects of the substrate nature.

Raman spectra showed clear differences in crystallinity on the different substrates at a fixed D_H. It is seen in figure 4.3 that, under the present deposition conditions, samples deposited with D_H < 87% led to a-Si:H films on all substrates. The transition from amorphous to nanocrystalline growth occurred in a very narrow range of D_H, but the threshold of hydrogen concentration in which crystalline growth started strongly depended on the substrate considered.

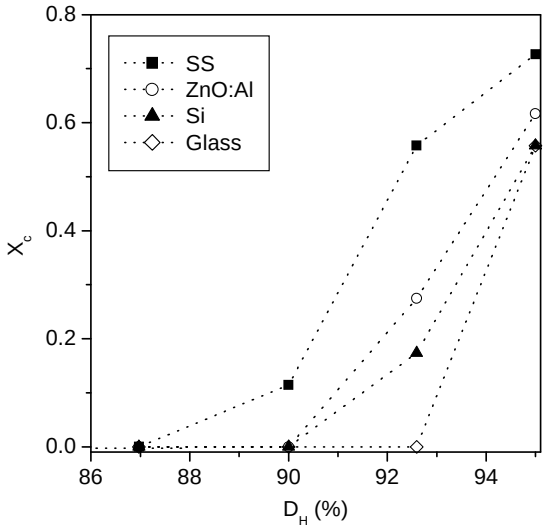

Fig. 4.3. Crystalline fraction values as a function of hydrogen dilution for the different substrates studied. The rest of the deposition conditions were P = $3x10^{-2}$ mbar, T_f = 1650ºC and T_s = 200ºC.

Stainless steel seemed to enhance nanocrystalline growth, being this substrate the sole having crystalline contribution at D_H = 90%. On the contrary, the threshold was higher on glass, where D_H = 95% was needed to have a measurable value of X_c. Thus, identical process conditions resulted in amorphous, half-crystalline or fully crystalline material depending on the substrate on which deposition took place. This conclusion is emphasised in figure 4.4, where the Raman spectra obtained at D_H = 92.5% are plotted. For this particular value of the hydrogen dilution, X_c on SS was 0.56, decreasing to 0.27 and 0.17 on ZnO:Al and Si, respectively. The spectrum on glass showed no trace of crystalline contribution, notwithstanding the high hydrogen dilution considered.

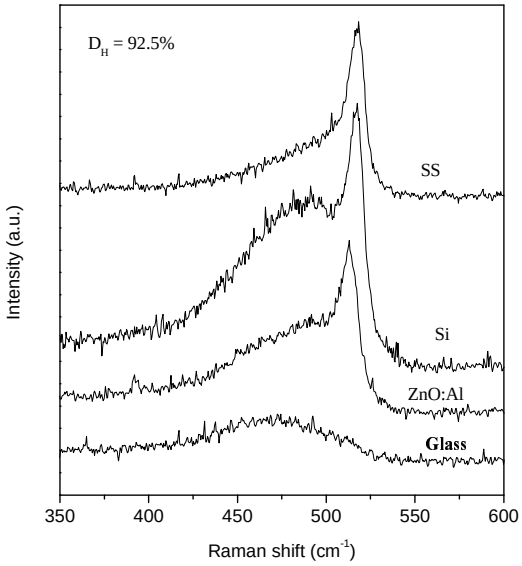

Fig. 4.4. Raman spectra for the samples deposited at D_H = 92.5% on different substrates.

FTIR measurements performed on the Si substrates also evidenced the transition from a-Si:H to nc-Si:H, as showed in figure 4.5. The Si-H_x stretching band in a-Si:H is centred around 2000 cm^{-1}, whereas in nc-Si:H this contribution is shifted to 2100 cm^{-1}. The hydrogen content of the samples lessened from values of 9-10% for $D_H \leq 92.5\%$ to C_H = 4.7% at D_H = 95%.

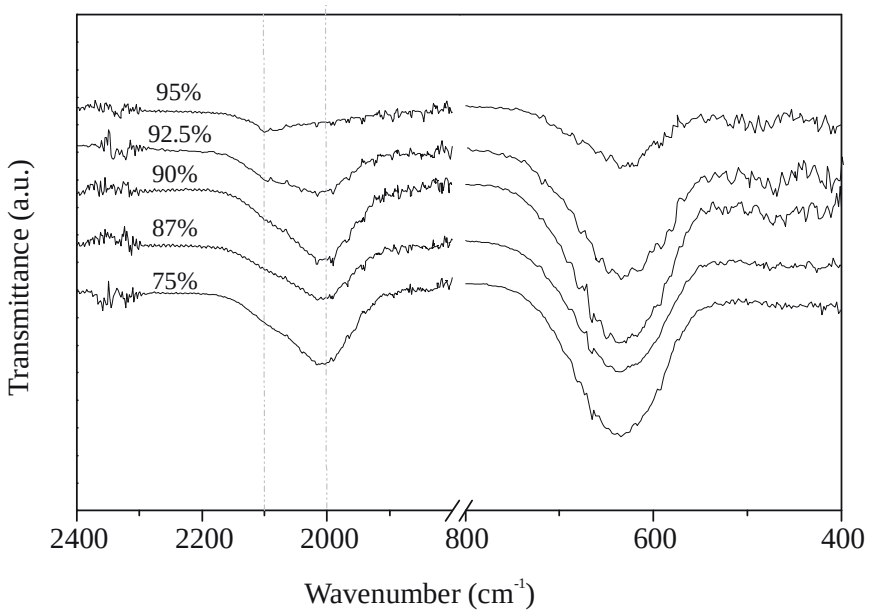

Fig. 4.5. FTIR spectra of the nc-Si:H samples deposited at different hydrogen dilutions.

XRD measurements, as expected, showed peaks in the same cases in which Raman spectra presented crystalline contribution. XRD spectra for all dilutions on SS substrate are plotted in figure 4.6. Under the present deposition conditions, only samples deposited at very high D_H (95%) exhibited (220) preferential orientation. This trend was observed for all substrates analysed (SS, ZnO:Al, and glass). Grains turned out to be bigger on SS (G_S = 24 nm) than on glass and ZnO:Al. Besides, little difference in G_S has been found between the latter, with values around 17 nm in both cases. Lower dilutions exhibited (111) preferential orientation and grain size diminished with decreasing amount of hydrogen entering the system.

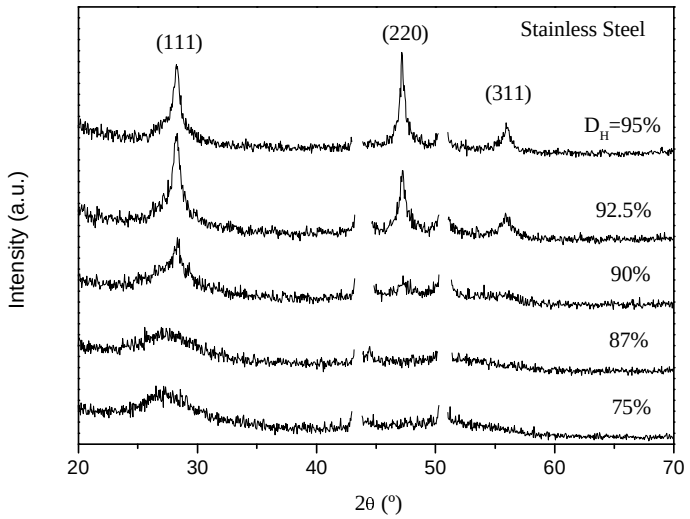

Fig. 4.6. XRD spectra measured on stainless steel substrates for the different hydrogen dilutions considered. Peaks corresponding to SS contributions have been removed to facilitate analysis.

Results presented in this section evidenced that the substrate on which a layer is grown does influence its microstructure. This effect is especially critical when the deposition regime is close to the transition from amorphous to nanocrystalline growth. Thus, results obtained from material characterisation should not be straightforwardly extrapolated to devices deposited on other substrates.

The fact that crystalline fractions on c-Si are larger than those obtained on glass is attributed to the former acting as a seed layer for nc-Si:H growth, permitting a better

coalescence of the material and, therefore, increasing nuclei size [Dirani et al., 2000]. [Bailat et al., 2002] reports higher X_c values on ZnO than on glass. [Klein et al., 2002b] and [Baia Neto et al., 2002] conclude that on metallic substrates like Al, crystalline growth is shifted to lower hydrogen dilutions than in the case of glass substrates for silicon thin films deposited by HWCVD and PECVD, respectively. These two trends, together with our results showing that $X_c(SS) > X_c(ZnO:Al) > X_c(glass)$ at a given hydrogen to silane ratio, seemed to point out that the major the conductivity of a substrate, the less amount of hydrogen necessary to obtain crystalline growth. [Kondo et al., 1996] attribute the influence of the conductivity to the bombardment of positive ions that takes place during PECVD deposition. Unfortunately, this explanation is not valid in the case of HWCVD deposition, where no ions are involved in the process. Additional explanations ascribe the origin of the substrate-dependent growth to the difference of nucleation of Si-Si bond strength on different substrates [Yu et al., 1996]. Regardless all the mentioned possibilities, the microscopic mechanism responsible for the substrate dependence of the microstructure of the layers still remains unclear and further investigation is needed.

4.3. Doped material

4.3.1. Substrate dependence

Taking into account that in a solar cell the doped layers are the ones actually deposited onto a foreign substrate, the study in section 4.2 has been also carried out with n and p-type layers. Both n and p series have been deposited at a process pressure of $3x10^{-2}$ mbar and using a SiH_4 flow of 4 sccm. Diborane doped layers have been obtained using a linear Ta wire heated up to 1850ºC whereas a 3-loop filament at 1750ºC was used to grow the n-type samples. In those latter, T_s was kept at 200ºC (like in the case of intrinsic material) but T_s = 125ºC was selected for the p-type layers, as undesired amorphisation is reported at higher substrate temperatures [Voz et al., 2000b]. The difference in filament geometry caused a decrease in the deposition rate for the B-doped layers. r_d on glass diminished from 7.5 to 4.5 Å/s with increasing hydrogen flow for n-type samples whereas for p layers r_d ~ 5 Å/s for D_H = 85% and 2 Å/s for D_H = 96%. The gas phase atomic ratios chosen were P/Si = 1% for n layers and B/Si = 5% for p-type ones.

Doped-layer thicknesses required in device structures are usually thinner than 0.1 μm. Since the material could be more defective at the initial stages of growth and cause thin layers to exhibit poorer properties than the thicker ones, all films analysed in this section have thicknesses around 0.1 μm. Further optimisation of the best layers described here to the adequate thickness required in solar cells will be needed before their implementation into the device.

Raman spectra of the doped samples showed that the crystalline fraction at a certain hydrogen dilution also depended on the substrate considered. X_c values on SS, ZnO:Al and glass at different D_H values for both p and n-type layers are presented in figure 4.7. The results obtained for intrinsic nc-Si:H in the previous section have also been included in the figure to facilitate comparison.

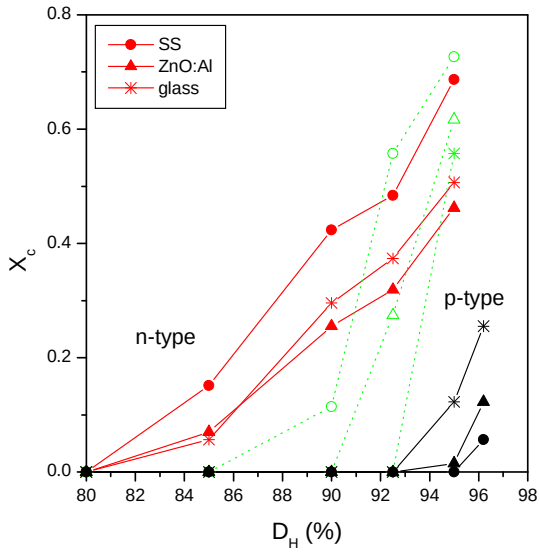

Fig. 4.7. Crystalline fractions at different hydrogen dilutions measured on SS, ZnO:Al and glass for both n and p-type layers. T_s = 200ºC for n-type layers and 125ºC for diborane doped ones. Dotted lines correspond to values measured on intrinsic nc-Si:H.

A clear difference in behaviour was seen depending on whether the doping gas considered was phosphine or diborane. Crystallisation took place at lower D_H for n-type layers on all substrates considered, as X_c values were measurable at D_H = 85% in all cases. On the other hand, D_H values of 95% or higher were necessary to detect any crystalline contribution in p-type samples. It is also worth remarking the fact that, in the case of n-type

layers, SS seemed to promote nanocrystalline growth (equally to that observed in intrinsic films) and there was little difference between glass and ZnO:Al coated glass. On the contrary, glass enhanced crystallinity of p-type samples and SS was the substrate on which less crystalline fraction was measured.

Dark conductivity measurements performed on layers deposited on glass substrates exhibited the same trend, as is shown in figure 4.8. σ_d values between 2 and 5 S/cm were observed for n samples with $D_H \geq 90\%$ and for $D_H \geq 95\%$ in the case of diborane-doped layers, which are characteristic of device-quality doped nc-Si:H [Schropp and Zeman, 1998]. Activation energy values measured in the most diluted samples were 0.06 eV for n-type layers ($D_H = 95\%$) and $E_a = 0.03$ eV in the case of p samples ($D_H = 96\%$). Results obtained for the amorphous layers were reasonably good for n layers ($\sigma_d \sim 10^{-3}$ S/cm) and poor for p samples when compared with standard PECVD layers [Schropp and Zeman, 1998]. A more detailed study regarding the conductivity of these samples and its substrate dependence can be found in [Soler, 2003].

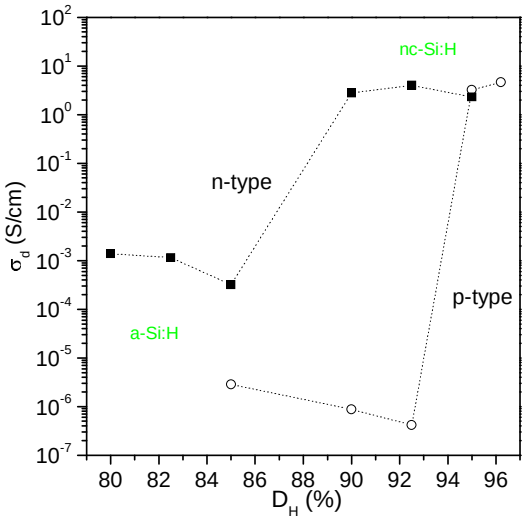

Fig. 4.8. Dark conductivity values measured in the samples deposited on glass at different hydrogen dilutions for both n and p-type films.

It is well known that the inclusion of diborane in the gas flow, especially in high B/Si ratios, causes amorphisation of the samples [Peiró et al., 1998], fact that could explain the need of higher hydrogen dilutions in p-type layers to achieve crystallinity. On the other

hand, from our results it could be deduced that the inclusion of phosphine in the gas mixture somehow favours crystalline nucleation and, therefore, results in nc-Si:H layers at lower hydrogen dilutions. One possible mechanism responsible for that behaviour could be nucleation taking place around the phosphorous atoms, so that they acted as seeds for the nanocrystalline grains. Anyway, further and thorough studies would be required as to elucidate the mechanism responsible for this behaviour. Also concerning doped material, influence of the first stages of growth in the quality of n-type layers will be considered in Annexe I of the present work.

From the results obtained in this chapter, it can be concluded that, especially in the region where the transition from amorphous to nanocrystalline growth takes place, the crystallinity of the samples clearly depended on the nature of the substrate on which they were deposited. Moreover, this behaviour strongly depended on the kind of material studied (n, i or p-type). Thus, as already mentioned for intrinsic material, results obtained on one particular substrate cannot be extrapolated to another one without taking into account the effect this change in substrate would cause.

4.3.2. Scaling to device size

Two structures are common in thin silicon film solar cells, superstrate or p-i-n and substrate or n-i-p configuration. All cells described in the present thesis were deposited in the p-i-n configuration on transparent substrates. In any configuration, apart from device-quality intrinsic material, doped layers do also have to be optimised in order to achieve reasonably good performances. Their optimisation mainly deals with their thickness, so that optical losses within them are minimised, while keeping good electrical property values. Therefore, having the best layers described in the previous section as a starting point, further optimisation of the doped layers was carried out by scaling them to the thickness suitable to device implementation. Samples analysed in the above-mentioned section were approximately 100 nm thick whereas thicknesses required in p-i-n structures are 50 nm or lower. This relatively high value (50 nm), despite ensuring good rectifying characteristics and preventing from shunting paths, might limit the maximum expected efficiency of the device due to optical losses caused by the absorption within the p-layer [Voz, 2001].

Best n-type material in the previous section was obtained using 1% phosphorous to silicon gas phase ratio and a hydrogen dilution of 95%. When decreasing the layer thickness from 100 to 40 nm, an increase in the doping ratio to [P]/[Si] = 2% was needed in order to keep dark conductivity values in the range of 5 S/cm and E_a = 0.02 eV. This very thin layer had a crystalline fraction as high as 0.37 (versus X_c = 0.43 for 0.75 μm-thick). HRTEM images evidenced the presence of crystallites near the interface, indicating crystalline growth from the very first stages of deposition, as shown in fig. 4.9. Hall measurements performed in 1 μm thick samples resulted in σ_d = 44 S/cm, μ = 0.74 cm^2/Vs and $N_D = 3.7x10^{20}$ cm^{-3} at the same phosphorous to silicon ratio.

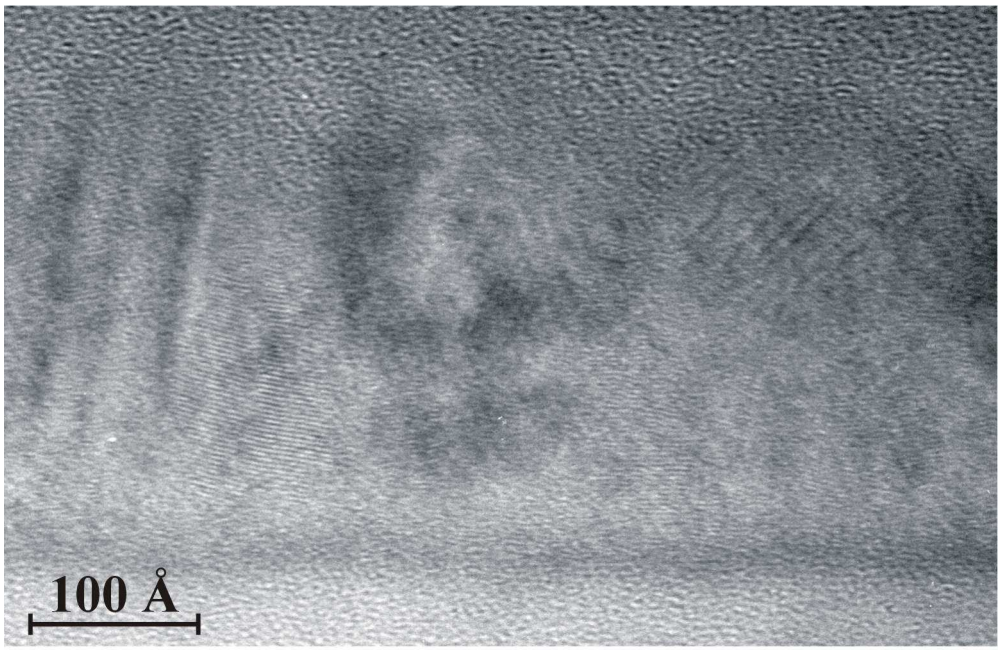

Fig. 4.9. Cross-section TEM image of a 30 nm thick n-layer deposited on glass evidencing crystalline growth from the first stages of deposition. The sample had been deposited at T_f = 1750ºC, T_s = 200ºC and at a process pressure of $3x10^{-2}$ mbar using a hydrogen dilution of 95% and a phosphorous to silicon ratio in gas phase of 2%.

On the other hand, in the case of p-type layers, boron to silicon gas phase ratio of 5% used in thick layers also led to room temperature dark conductivity values in the range of 2.5 S/cm and E_a ~ 0.04 eV when dealing with thicknesses of approximately 50 nm. Due to the high hydrogen dilution required in boron-doped layers to achieve the desired degree of

crystallinity on ZnO:Al, resulting material on glass exhibited crystalline fraction values around 0.42. Figure 4.10 shows the effect the thickness of the layers had in their crystalline fraction. Measurements carried out in thicker layers (~ 1 μm) to fully characterise the material resulted in σ_d = 40 S/cm, μ = 2.06 cm^2/Vs and N_A = $1.2x10^{20}$ cm^{-3} in samples presenting (220) crystalline preferential orientation and grain sizes around 60 nm.

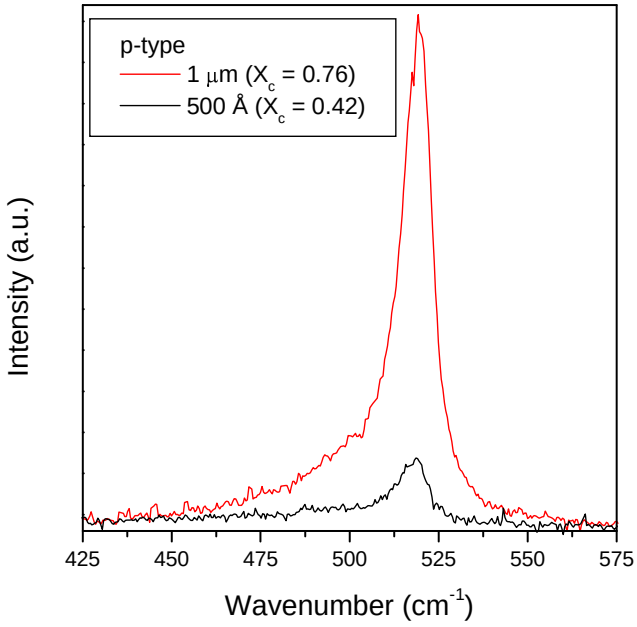

Fig. 4.10. Raman spectra of boron-doped layers with different thicknesses.

Doped layers used in the solar cells described in the following chapter will be deposited in the same deposition conditions described in this section, which are summarised in table 4.2.

Type	*P (mbar)*	*T_s (ºC)*	*T_f (ºC)*	*D_H (%)*	*B/Si or P/Si (%)*
p	$3x10^{-2}$	125	1850	96	5
n	$3x10^{-2}$	200	1750	95	2

Table 4.2. Summary of deposition conditions for very thin doped layers.

5. Solar cells

The choice of the most suitable material might be the central issue in the development of nc-Si:H solar cells. Nevertheless, in order to obtain devices with enhanced photovoltaic conversion, additional aspects in the process of designing a solar cell also have to be taken into consideration.

First aspect that needs to be taken into account is that concerning doped layers, which has already been considered in the previous chapter. On the other hand, due to the fact that edges are not very well defined during deposition in CVD processes, the n or i layers might laterally contact the TCO, thus leading to the existence of lateral leakage currents. Such parasitic currents behave like a very low parallel resistance shunting the device, and are especially notorious when the doped layers used are heavily doped. Fortunately, this technological drawback can be effectively solved by somehow “cutting” the device, i.e. by interrupting the path of the parasitic current.

A third fact that is crucial in thin-film silicon technology development is light confinement. By using light-trapping strategies, like textured conductive oxides and metallic reflectors, enhancement of the light absorption is achieved, thus leading to higher conversion efficiencies and the possibility of achieving equal performances in thinner devices. This last fact is of special interest facing industrial applications, as a reduction of the thickness of the active layer means a reduction in production time and costs.

This chapter is structured in two almost independent parts. The first half mainly deals with all these different aspects that need to be taken into consideration when fully optimising a solar cell. First of all, the effects of avoiding lateral leakage currents and enhancing light absorption in p-i-n solar cells will be qualitatively shown before properly analysing the behaviour of the devices. Complementary, the second part of the chapter focuses in the performance of different solar cells. The stability against light soaking of several devices with relation to their microstructure will be studied. Finally, results of a preliminary solar cell where all the details described in the first part of the chapter have been implemented will be also presented.

5.1. Leakage currents

Thin film rectifying devices result often affected by leakage currents. Therefore, when a reverse voltage is applied to a p-i-n device, the current that circulates is the reverse diode saturation current (I_0) plus leakage currents, as illustrated in figure 5.1. Leakage currents usually present an ohmic behaviour that allows them to be modelled by a parallel resistance shunting the device. Low parallel resistance values can significantly degrade the open circuit voltage and fill factor at low-medium irradiances [Voz, 2001]. Depending on the path followed, two different kinds of leakage currents are distinguished, lateral (I_l) and transversal (I_t) leakage currents. The latter are the result of the eventual formation of shunting paths or pinholes within the device, generally during deposition. Unfortunately, once the device is completed, transverse leakage currents cannot be solved. On the other hand, lateral leakage currents, mainly through the n-type layer, owe their existence to the fact that during CVD processes edges are not very well defined and, therefore, the n or i layers might laterally contact the TCO. Lateral leakage currents can be especially dramatic when, like in our case, the doped layers used are heavily doped and the active area of the device is small.

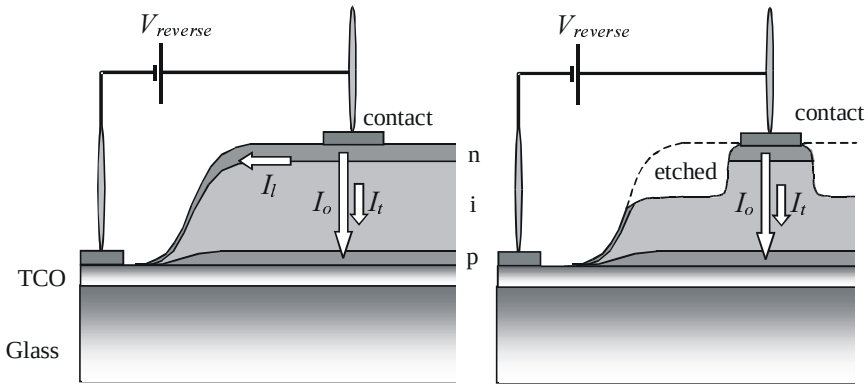

Fig. 5.1. Scheme of the leakage currents in a p-i-n solar cell [Voz, 2001]. The lateral leakage current can be avoided by etching the material surrounding the device.

Contrary to what happens with transversal leakage currents, lateral ones can be reduced by somehow cutting the n layer around the contact, thus avoiding its lateral contact with the TCO acting as front contact. Laser scribing is an effective technique to reduce lateral leakage currents by literally cutting the n-type layer around the contact [Schropp and

Zeman, 1998]. Alternatively, this kind of currents can also be avoided by etching the material surrounding the device itself, as shown in fig. 5.1. In collaboration with the Universitat Politècnica de Catalunya, our nc-Si:H p-i-n solar cells have been dry-etched with a plasma of CF_4 diluted into oxygen (20%) at a process pressure of 0.4 mbar.

The effect of dry etching on the dark current-voltage characteristics is shown in fig. 5.2, where the lateral leakage currents were clearly reduced after the etching. Fig. 5.3 shows the same current-voltage characteristics under 100 mW/cm^2 illumination, where clear reduction in the parallel resistance and improvement in the fill factor (from 0.45 prior to etching to 0.62 right afterwards) were achieved despite some undesired reduction of the $V_{oc,}$ attributable to some damage of the n-type layer during the etching process.

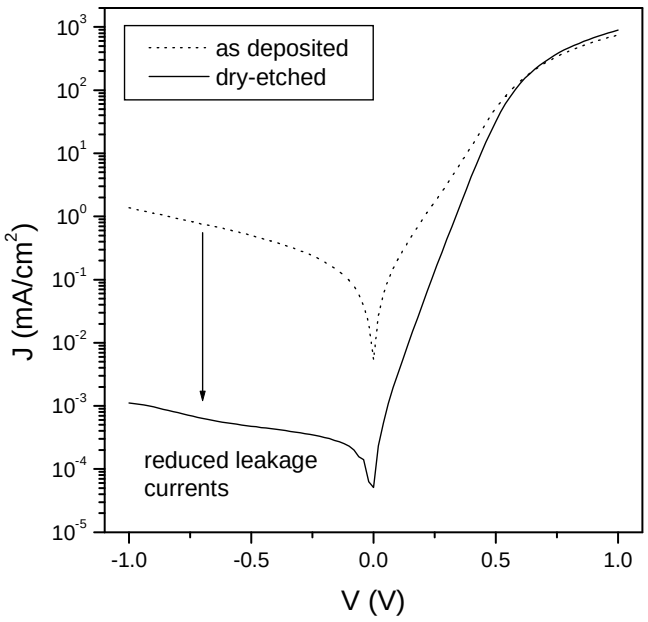

Fig. 5.2 Dark current-voltage characteristics before and after dry-etching the device. Lateral leakage currents were clearly reduced.

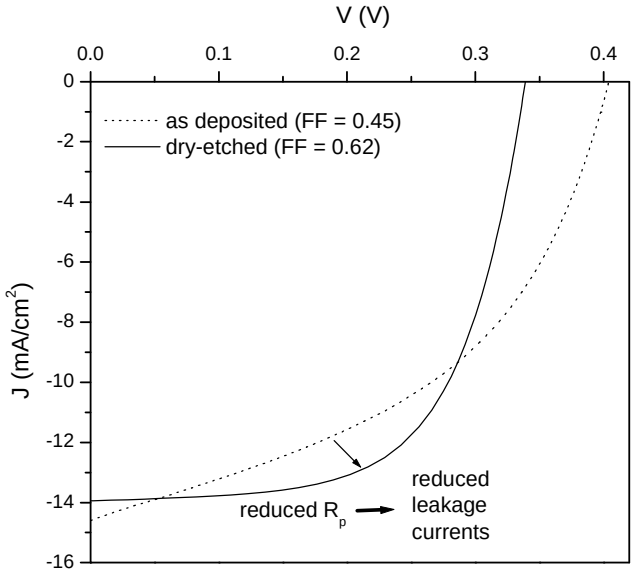

Fig. 5.3. Current-voltage characteristics under AM1.5 illumination before and after dry-etching the cell in fig. 5.2. Reduction of the parallel resistance and improvement in the fill factor were clearly seen. Undesired reduction of the V_{oc} might be due to some damage of the n-type layer during the etching process.

5.2. Light confinement

In thin-film silicon solar cell technology, light confinement by transparent conductive oxides and metallic reflectors plays a fundamental role for the efficiency. These features are of special interest as they allow, together with an increase of the device efficiency, a reduction of the thickness of the active layer and, thus, in production time and costs. Figure 5.4 shows the structure of a p-i-n solar cell including light-trapping strategies, i.e. the use of a textured front contact and of a reflector in the back contact.

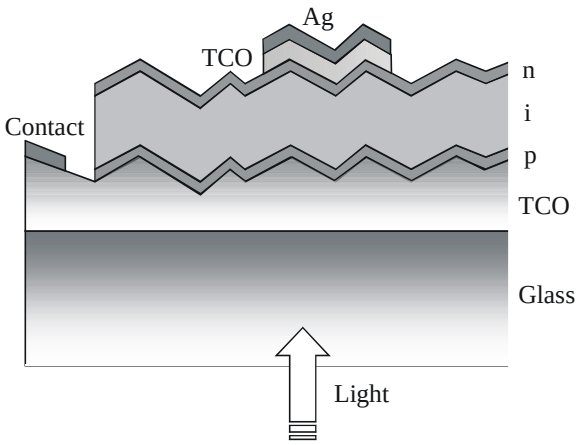

Fig. 5.4 Scheme of a p-i-n solar cell structure including light-trapping strategies: textured front TCO and back reflector.

5.2.1. Front contact

In superstrate-structured devices, the front contact consists of a TCO directly deposited onto glass. Materials most commonly used in these structures are fluorinated tin oxide (SnO_2:F), aluminium doped zinc oxide (ZnO:Al) and indium tin oxide (In_2O_3:Sn or ITO). The requirements the electrode material has to fulfil are [Schropp and Zeman, 1998]:

a) high transmission (preferably > 85%) in the entire wavelength region where the photovoltaic absorber layers are active
b) low sheet resistance (preferably < 10 Ω/□) to minimise series resistance losses
c) low contact resistance with the p-type layer of the p-i-n structure
d) a rough surface to increase the optical path of the light by scattering, while the morphology should avoid shunting paths, pinholes or local depletion
e) chemical resistance against the strongly reducing hydrogen ambient during CVD
f) high thermal stability to avoid diffusion of elements into the growing layer

H-atom density in HWCVD process is one or two orders of magnitude higher than in conventional PECVD process [Masuda et al., 2002]. This strongly reducing atmosphere during deposition leads to a chemical reduction of both ITO and SnO_2:F causing a drastic decrease in their transmittance due to the appearance of metallic Sn or SnO on the surface. Conversely, ZnO:Al films suffer no darkening after exposure to atomic hydrogen [Minami

et al., 1989]. Therefore, textured ZnO:Al films tend to be the preferred option as front contact in p-i-n structures. In this kind of TCO, either texturation is achieved directly during deposition [Meier et al., 2000] or surface textures develop upon etching in diluted HCl [Kluth et al., 1999].

ZnO:Al can also be used as a coating to prevent reduction of SnO_2:F layers [Masuda et al., 2002b, Nasuno et al., 2002], taking advantage of both the optimised surface texturation of commercial SnO_2:F (Asahi-U) and the chemical resistance against the strongly reducing ambient during HWCVD process of ZnO:Al.

We deposited 700 Å ZnO:Al on top of Asahi-U by RF magnetron sputtering from a ceramic target (ZnO:Al_2O_3 98:2 wt%, 99.99% purity) and verified that the good properties of the latter were kept after the coating. Figure 5.5 shows the AFM images of Asahi-U and ZnO:Al coated Asahi-U, the latter before and after 15 minutes of hydrogen treatment ($\phi(H_2)$ = 20 sccm, T_f = 1720ºC, P = $3x10^{-2}$ mbar). RMS roughness, as deduced from those images, increased from 30 to 40 nm with the coating, and suffered no appreciable change upon HW hydrogen treatment. Sheet resistance measured was in the range of 15 Ω/□ both before and after the ZnO:Al coating.

Transmittance measurements were also performed on Asahi-U and ZnO:Al coated Asahi-U before and after being exposed to a hydrogen flow decomposed by a hot tantalum wire (T_f = 1720ºC). The transmittance spectra obtained are plotted in figure 5.6. The transmittance of ZnO:Al coated Asahi-U slightly improved in the long wavelength part of the spectrum while the electrical properties remained unchanged. Conversely, plain Asahi-U, as expected, drastically darkened under the strong reducing atmosphere.

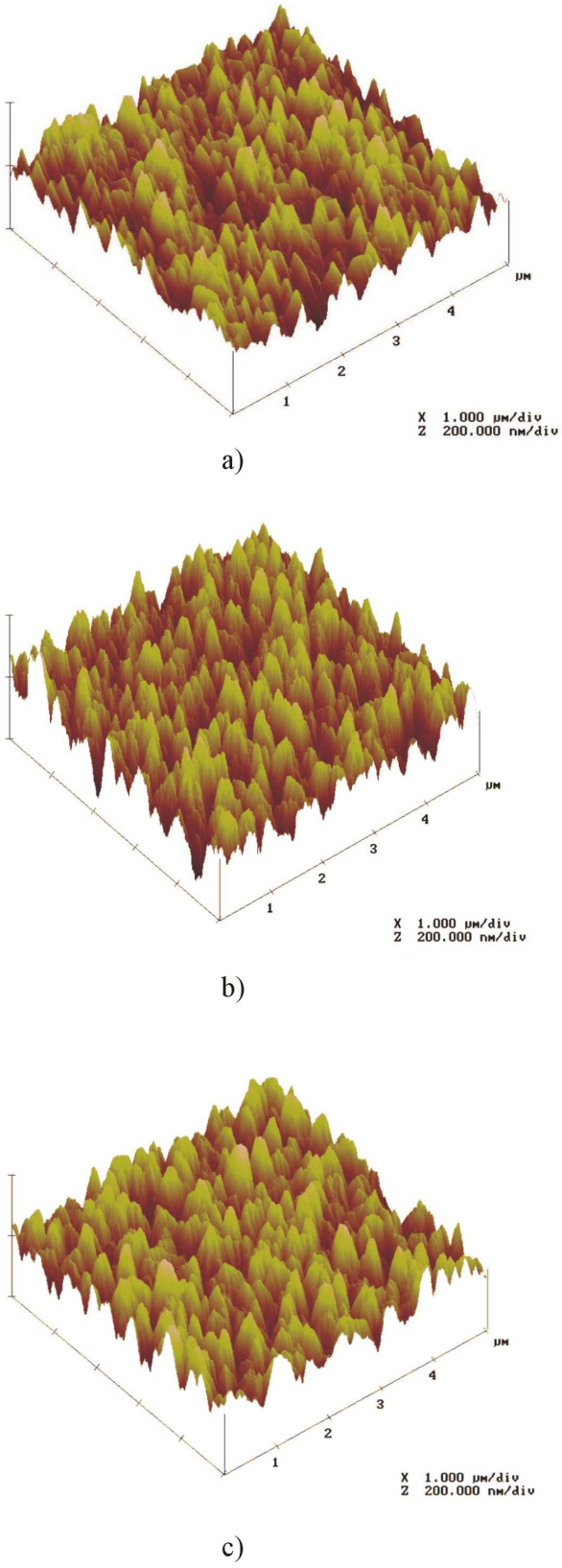

Fig 5.5. AFM images of a) Asahi-U, b) ZnO:Al coated Asahi-U and c) ZnO:Al coated Asahi-U after 15 minutes HW hydrogen treatment.

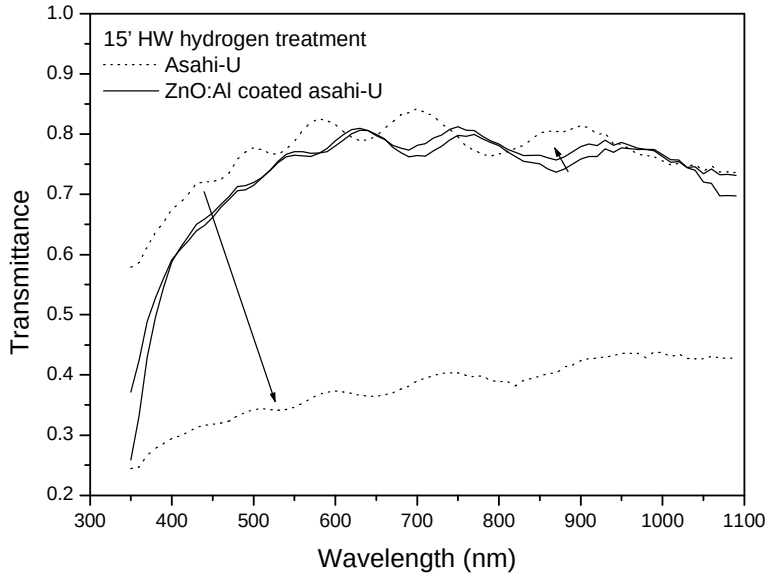

Fig. 5.6. Effect of 15 minutes of HW hydrogen treatment (T_f = 1720ºC) on the transmittance spectra of plain and ZnO:Al coated Asahi-U.

Finally, the implementation of ZnO:Al coated Asahi-U as a front contact in a nc-Si:H p-i-n solar cell, instead of flat ZnO:Al, resulted in a remarkable increase in the short-circuit current and the fill factor due to enhanced light trapping within the device as a consequence of the textured surface of Asahi-U. The effect of the texture in the front contact in one of our devices is illustrated in figure 5.7, where the J-V curves of two cells deposited at the same time on the different substrates considered are plotted.

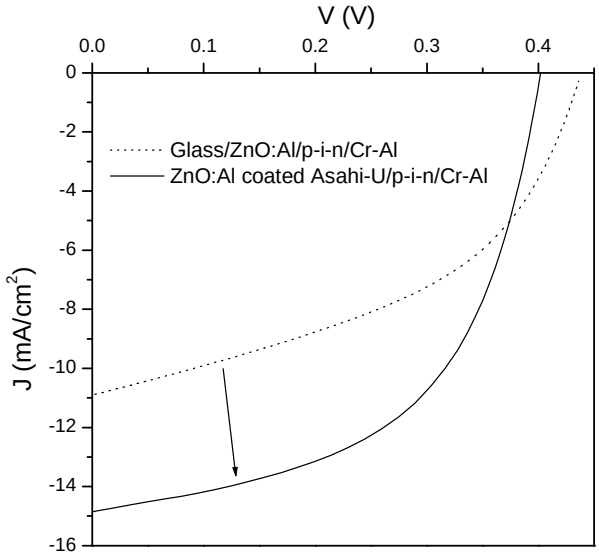

Fig. 5.7. Effect of the use of a textured TCO as front contact in a p-i-n solar cell. Clear improvement in J_{sc} and FF is achieved when growing the same device on ZnO:Al coated Asahi-U instead of on flat ZnO:Al.

5.2.2. Back reflector

A complementary procedure to enhance light absorption within the solar cell is the use of a back contact with reflecting properties, a so-called back reflector [Fig. 5.8]. In combination with silver or aluminium, ZnO is standardly used to enhance the back reflection in p-i-n and n-i-p solar cells. Other TCOs like ZnO:Al and ITO (In_2O_3:Sn) are also used with the same purpose [Hegedus et al., 1997]. In this part of the structure, the TCO has the additional function of preventing diffusion of Ag into the doped layer.

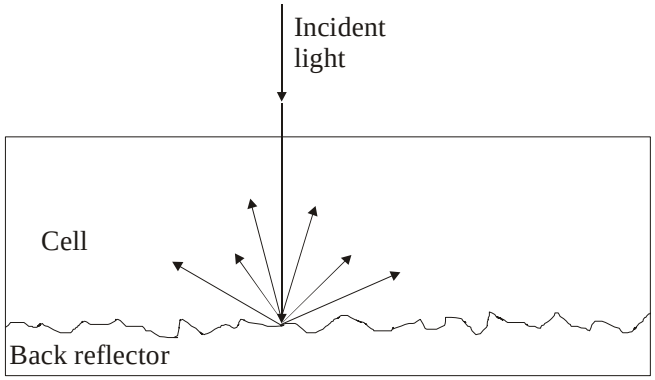

Fig. 5.8. Scheme of light behaviour in contact with a textured back reflector.

Back reflectors considered in this work were ZnO:Al/Ag. ZnO:Al was deposited by RF magnetron sputtering and silver was thermally evaporated on top of the TCO. Al was evaporated on top of the Ag reflector in some cases as a protection against dry-etching, and therefore being ZnO:Al/Ag/Al the complete structure of the back contact. Fig. 5.9 shows the effect the implementation of a ZnO:Al/Ag back reflector instead of a plain metallic Cr/Al back contact had, resulting in a clear improvement in the carrier generation in the long-wavelength region ($\lambda > 650$ nm). The TCO layer used in both cases was around 80 nm thick. In further optimisation of this part of the cell structure different TCO thicknesses and materials (undoped ZnO or ITO) should be analysed.

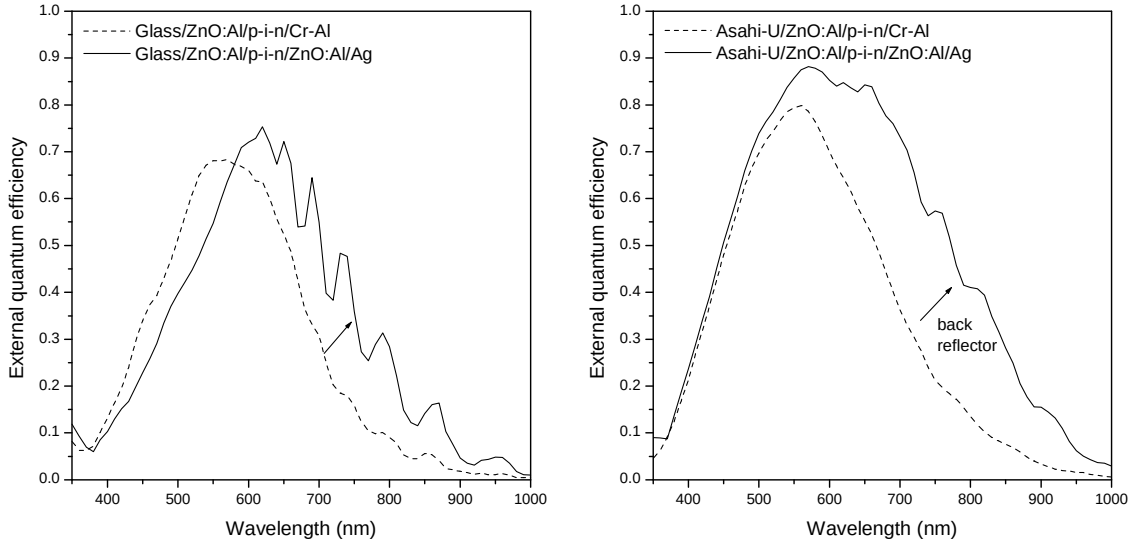

a) b)

Fig. 5.9. Effect of the inclusion of a ZnO:Al/Ag back reflector in the spectral response of two different p-i-n solar cells. Cell a) had smooth ZnO:Al as front contact whereas cell b) was deposited onto ZnO:Al coated Asahi-U.

5.3. HW nc-Si:H solar cells

Despite the fact that the study of the material and its properties is a key issue in the development of thin silicon film photovoltaic technology, the nucleus of this development lies in the analysis of complete devices. As already mentioned at the beginning of the chapter, all cells studied in the present work, have been deposited in the p-i-n configuration, which allows low temperature deposition on cheap substrates. p-i-n

structures have been deposited onto ZnO:Al coated Asahi-U. Doped layers employed, both n and p-type, were also deposited by HWCVD under the same conditions than the ones described in section 4.3.2. Typical thicknesses considered were 70 nm for the p-type layers and 50 nm in the case of phosphorous-doped ones. Substrate size considered was 1" x 1", on which several back contacts were deposited once the cell had been deposited and, therefore, different devices were analysed within the same substrate.

As already mentioned throughout this work, best efficiencies for single-junction nc-Si:H solar cells have been achieved using material close to the transition to amorphous growth [Meier et al., 2001, Klein et al., 2002]. This kind of material has an important amount of amorphous tissue that can turn out to enhance the degradation of the device when exposed to long time illumination (the so-called Staebler-Wronski effect [Staebler and Wronski, 1977]). Light induced degradation up to 10% of the initial cell efficiency has been reported in nc-Si:H solar cells with high amorphous volume fractions [Klein et al., 2003].

Compact material deposited after the implementation of the funnel, that described in section 3.3, had a crystalline fraction of 0.51. A p-i-n solar cell having this material as active layer was stable even after several months of air exposure and 1000 hours of 100 mW/cm^2 light soaking. Growing interest in material close to the transition the amorphous growth regime, led to a study of the relation between the microstructure of the active layer and the solar cell performance having the above-mentioned material as a starting point.

5.3.1. Structural properties

Thus, in order to study the relation between the amount of amorphous fraction in the active layer of a nc-Si:H solar cell and the possible creation of light-induced defects, several p-i-n devices were deposited using different hydrogen to silane ratios in the growth of the intrinsic layer. Studied hydrogen dilution values were comprised between D_H = 93.5 and 95%. The rest of the deposition conditions, in all cases, were $T_f \sim 1600^oC$, $T_s = 200^oC$, $P = 3x10^{-2}$ mbar and $\phi(SiH_4) = 4$ sccm. Total device thickness was 1.1 μm for the devices with $D_H \leq 94.4\%$ and 1.4 μm in the case where the highest dilution was used.

Figure 5.10 shows the Raman spectra obtained for the different values of D_H considered. Appreciable differences in crystallinity were observed, despite the small

variation in the amount of hydrogen used in the different cases. This fact is illustrated in the inset in fig. 5.10, where the crystallinity values deduced from the Raman spectra are plotted, thus evidencing that, in the region close to the transition between amorphous and nanocrystalline growth, even very small changes in the deposition conditions led to significant differences in the microstructure of the resulting material.

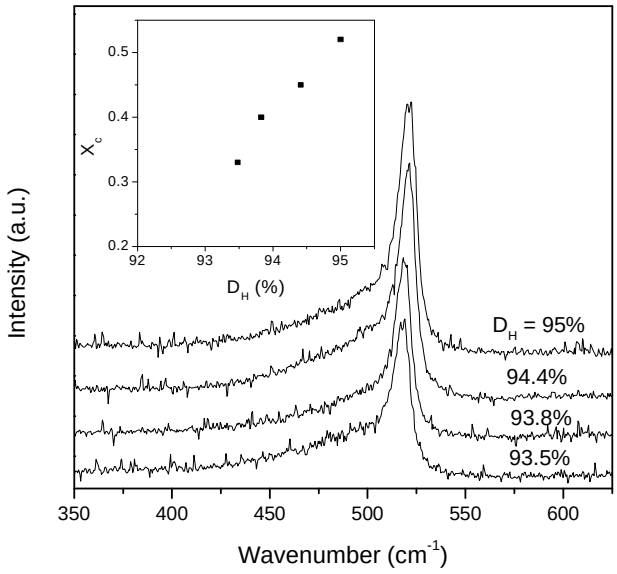

Fig. 5.10. Raman spectra of solar cells with active layers deposited at different hydrogen dilutions. The inset shows the evolution of the crystallinity with D_H.

XRD measurements plotted in figure 5.11 evidenced (220) crystalline preferential orientation for all dilutions considered. Spectra shown there correspond to p-i-n structures grown on glass substrates during the same process in which their counterparts on TCO were deposited. The ratio $I_{(220)}/I_{(111)}$ had its maximum at D_H = 94.4%, where the (111) peak was inappreciable for being either inexistent or small enough to be hidden by the broad amorphous contribution. Grain sizes (G_s) calculated from the XRD spectra evolve from 32 nm at D_H = 94.4 and 95% to 22 nm at D_H = 93.5%, having a maximum of 40 nm at D_H = 93.8%.

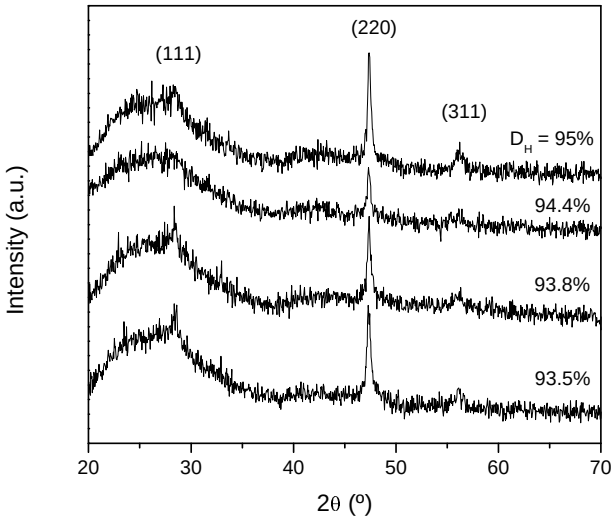

Fig. 5.11. XRD spectra of solar cells as a function of the hydrogen dilution used in the active layer.

5.3.2. Stability of the devices

Stability of the cells deposited at D_H = 95, 94.4 and 93.8% against light soaking and the possible creation of light induced defects and other aspects that could also influence the performance of the devices were evaluated by VIM measurements performed at different stages during 1000 hours of AM1.5 (100 mW/cm^2) illumination.

Figure 5.12 shows the evolution of R_{sc} and FF during the light soaking process for the three cells considered. Little difference was seen between the initial and final states of the cell deposited at D_H = 95%. A slight decrease in R_p, the low illumination limit of R_{sc}, was noticeable eight months after deposition, prior to light soaking of the device. This behaviour could be attributed to some chemical stabilisation of the surface. Identical behaviour in R_{sc} was observed in the 94.4% cell, where a decrease in R_p was also seen between the initial measurement and that performed after 500 hours of illumination. Additionally, a fall of the FF in the high illumination regime with increasing light exposure was observed. An increase of the resistive losses at the contacts of the devices when long exposed to air could be the cause of this sharp decrease, as high series resistances limit the fill factor at high illuminations. Finally, a clear degradation of both FF and R_{sc} upon light exposure for the intermediate illumination regime -where R_{sc} can be correlated with the i-layer properties- was seen in the cell with the highest amount of amorphous fraction

(D_H = 93.8%). The trend observed in this case was similar to that of a-Si:H solar cells when exposed to long time illumination [Merten et al., 1998].

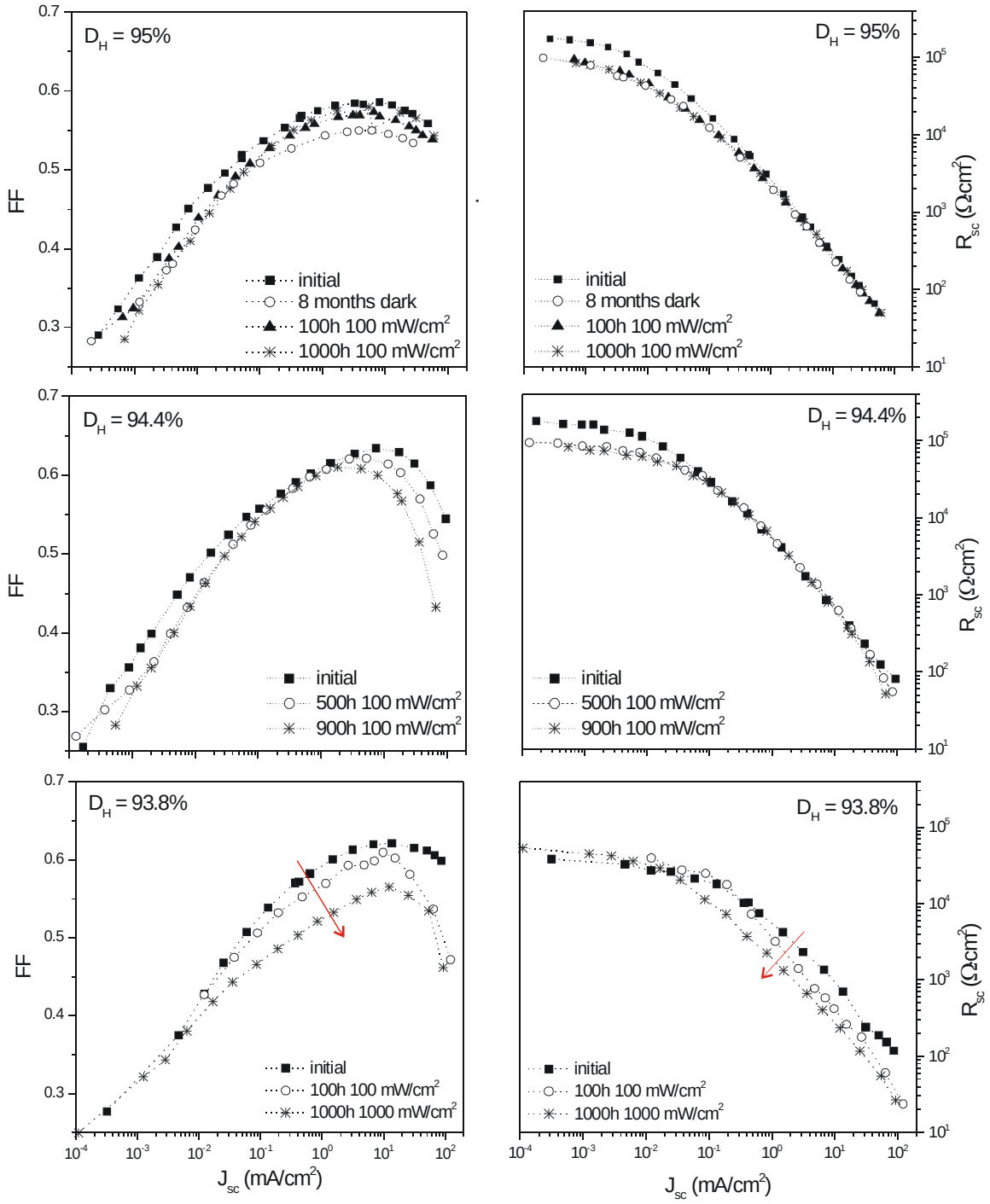

Fig. 5.12. Evolution of FF (a) and R_{sc} (b) during 1000 hours of 100 mW/cm^2 illumination for three cells deposited at D_H = 95, 94.4 and 93.8%.

The dangling bond density (N_{DB}) at the different stages of the process has been estimated from the collection potential ($V_c = J_{sc} \cdot R_{sc}$) at the intermediate illumination regime, where this last parameter is independent of parasitic effects and the illumination level, using[1]:

$$N_{DB} = 3.0 \cdot 10^8 (V^{-1} cm^{-1}) \cdot \frac{V_{bi}^2}{V_{c0} \cdot L^2} \tag{5.1}$$

where V_{bi} stands for the built-in potential (we have considered V_{bi} = 1.1 eV, as our doped layers were heavily doped), V_{c0} is the value of the collection potential at intermediate illumination level and L is the thickness of the cell.

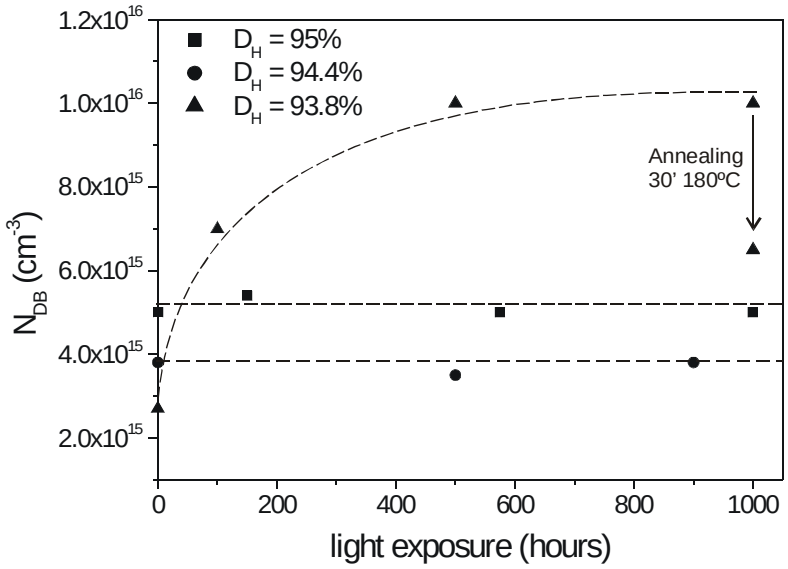

Fig. 5.13. Evolution of the dangling bond density with light exposure for different hydrogen dilutions of the active layer.

The evolution of N_{DB} during 1000 hours of light soaking for the three cells under study is presented in figure 5.13. Analysing this figure, it can be concluded that almost no change in the defect density was appreciated for the most crystalline cell (D_H = 95%). Therefore, recombination in this device kept constant throughout the whole experiment. No change in the dangling bond density over more than 900 hours of light soaking was either seen in the

[1] The explanation of the relation between N_{DB} and V_{oc} and the values of the parameters used in this calculation can be found in Annexe III to the present thesis.

cell deposited at D_H = 94.4%. Defect density values measured in this case were lower than those observed using higher hydrogen dilutions. In fact, if the three dilutions are considered, the lower the amount of hydrogen used during deposition, and therefore also the crystallinity of the sample, the lower the initial dangling bond density obtained.

Taking a look at the results for the cell deposited at D_H = 93.8%, an increase in N_{DB} from $2.7x10^{15}$ to $7.0x10^{15}$ cm^{-3} was observed after only 100 hours of light exposure. Such increment in the dangling bond density was caused by a sharp drop in V_{c0} from 11 to 4.3 V. Longer light exposure resulted in further increasing of the dangling bond density up to $N_{DB} = 1.0x10^{16}$ cm^{-3}. A thirty-minute annealing at 180ºC performed after the light soaking process returned V_{c0} and N_{DB} to values very similar to those measured after only 100 hours of illumination, as is also shown in fig. 5.13. No further improvement was appreciable after a one-hour additional annealing process at 180ºC. Therefore, two different mechanisms seemed to be responsible for the dangling bond creation upon light exposure. On one hand, irreversible changes took place during the first 100 hours of light soaking. One possible explanation of this misbehaviour could be defect creation due to doping diffusion coming from the low temperature deposited p-layer. On the other hand, a reversible change in N_{DB} was observed for long time illumination. The ratio between the density of dangling bonds in the degraded state before and after the annealing is close to a factor of two, clearly lower than the change in one order of magnitude observed for a-Si:H solar cells deposited with the same technique [Merten et al., 1998].

In order to be able to distinguish the recombination mechanisms (in both neutral and charged defect states) and other parasitic effects that might affect the performance of the devices, a model for the short circuit resistance (R_{sc}) taking into account all the different possible contributions has been proposed:

$$R_{sc} = \frac{1}{\frac{J_{sc}}{V_{c0}} + \frac{J_{sc}^{1/2}}{\gamma V_{c0}} + \frac{1}{R_p}} + R_s \qquad (5.2)$$

As is also explained in section III.3 of Annexe III to this work, in this model, the term J_{sc}/V_{c0} takes into account recombination in neutral defects within the volume of the active layer. Recombination in charged states is considered in the second term in the

denominator. The parameter γ indicates the relative importance of this mechanism, being more dominant for lower values of γ. Finally, the terms $1/R_p$ and R_s represent lateral leakages in the p-i-n junction and resistive losses at the contacts, respectively. V_{c0} in equation (5.2) corresponds to the value V_c would have in the intermediate illumination regime, where it is independent of parasitic effects and illumination level.

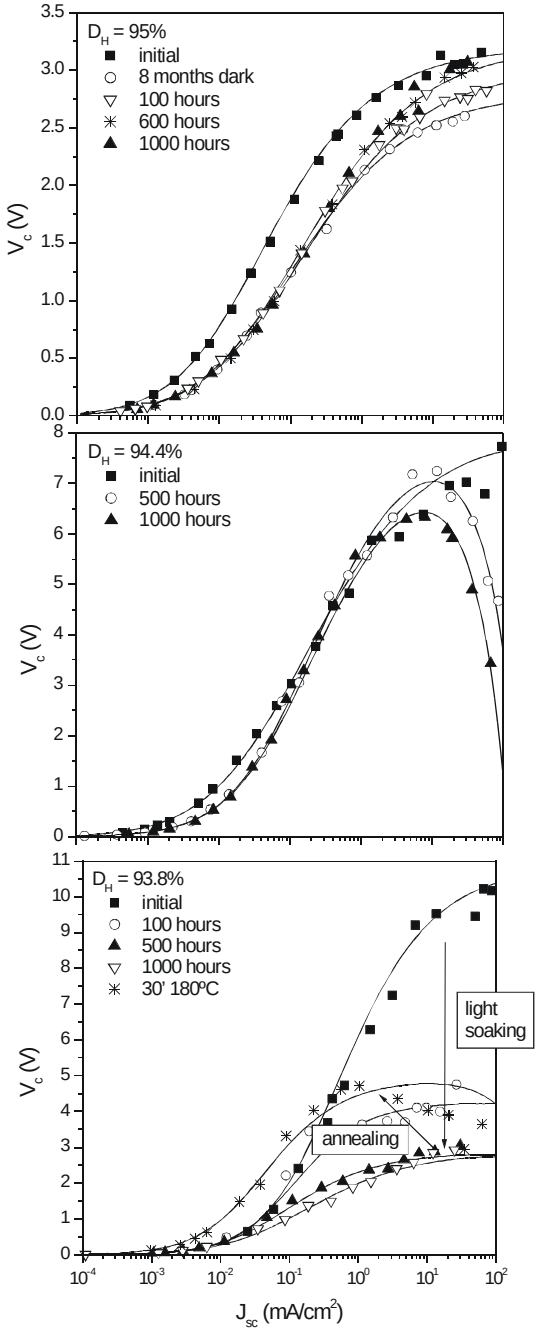

Fig. 5.14. Evolution of V_c during 1000 hours of AM1.5 light soaking for the cells in fig. 5.12. Symbols correspond to experimental data and lines to the fit using (5.2).

Results obtained from properly tuning the parameters in equation (5.2) are presented in fig. 5.14 (taking into account that $V_c(J_{sc}) = R_{sc} \cdot J_{sc}$) together with VIM experimental data for the collection potential. Collection potential, instead of R_{sc}, was chosen to illustrate trends observed during light soaking process as effects under analysis are more clearly seen in the V_c plot. Parameter values needed to fit the experimental data are summarised in table 5.1.

D_H = 95%	V_{c0} (V)	γ ($A^{-1/2}$)	R_p ($\Omega \cdot cm^2$)	R_s ($\Omega \cdot cm^2$)	N_{DB} (cm^{-3})
Initial	3.2	5.5	2.5×10^5	0.2	5.0×10^{15}
8 months dark	2.8	3.0	1.5×10^5	0.2	5.8×10^{15}
100h light	3.0	3.0	1.5×10^5	0.2	5.4×10^{15}
600h light	3.2	2.5	1.5×10^5	0.2	5.0×10^{15}
1000h light	3.2	2.5	1.5×10^5	0.2	5.0×0^{15}

D_H = 94.4%	V_{c0} (V)	γ ($A^{-1/2}$)	R_p ($\Omega \cdot cm^2$)	R_s ($\Omega \cdot cm^2$)	N_{DB} (cm^{-3})
Initial	8.0	2.3	3.0×10^5	0.2	3.8×10^{15}
500h light	8.5	2.5	1.0×10^5	45	3.5×10^{15}
900h light	8.0	2.5	1.0×10^5	65	3.8×10^{15}

D_H = 93.8%	V_{c0} (V)	γ ($A^{-1/2}$)	R_p ($\Omega \cdot cm^2$)	R_s ($\Omega \cdot cm^2$)	N_{DB} (cm^{-3})
Initial	11.0	1.9	4×10^4	0.5	2.7×10^{15}
100h light	4.3	12	4×10^4	0.5	7.0×10^{15}
500h light	2.9	5	5×10^4	0.5	1.0×10^{16}
1000h light	2.9	2.5	5×10^4	0.5	1.0×10^{16}
Annealed	4.5	12	2×10^5	10	6.5×10^{15}

Table 5.1. Values calculated from equation (5.2) in the fits plotted in figure 5.14 for the cells deposited at D_H = 95, 94.4 and 93.8%.

If we first consider the 95% cell, main changes were observed between the initial measurements and those performed 8 months afterwards, prior to any light soaking process. Thus, differences appreciated in γ and R_p could be mainly attributed to an increase in recombination in charged centres, most likely due to some kind of doping diffusion into

the active layer. On the contrary, it could be concluded that, in this case, recombination in neutral centres kept stable during the whole light soaking process, as variations observed in the density of neutral defects were minimal.

Equally to the behaviour plotted in fig. 5.12, a decrease in R_p imputable to a change in lateral leakages upon exposure to the atmosphere was detected in the cell deposited with $D_H = 94.4\%$. No changes in the recombination mechanism upon light soaking were appreciable in this case. Contrary to that, a sharp increase in R_s, causing a drop in the V_c curve at high illumination levels, was observed after long time light exposure. Similar behaviour of the series resistance was reported in [Merten et al., 1998] for some a-Si:H modules, where it was related to degradation effects outside the p-i-n junction, like some kind of degradation or corrosion of the contacts.

Analysing results concerning the 93.8% cell shown in figures 5.12, 5.13 and 5.14, a clear degradation of the material properties was seen during and after light exposure. Annealing of the sample at 180ºC led to a recovery of the values to ones similar to those measured after 100 hours of light soaking. Therefore, irreversible changes seemed to have taken place during the first 100 hours of the experiment. Additionally, a reversible change in N_{DB} was clearly observed. The ratio between the density of dangling bonds in the degraded state before and after the annealing is close to a factor of two, much lower than the change in one order of magnitude observed for a-Si:H solar cells deposited with the same technique [Merten et al., 1998].

Summarising the results extracted from the light soaking experiments performed, we could conclude that the devices suffered from initial irreversible changes mainly imputable to chemical stabilisation of surfaces and interfaces like oxidation or doping diffusion into the active layer. Despite the low crystallinity of the cells studied, only that deposited at $D_H = 93.8\%$ showed a remarkable defect creation upon light exposure. This effect was reversed after a thermal annealing of the sample at 180ºC. The influence of the amorphous tissue in the transport properties of nc-Si:H seemed to be the cause of such misbehaviour. The threshold between the two different behaviours (stable and metastable) of the defect density in nc-Si:H thus lay somewhere between crystalline fractions of 0.40 and 0.45.

5.3.3. Best results and perspectives

Up to now, best results in a preliminary device using light trapping strategies have been achieved in the cell deposited using D_H = 94.4% described in the previous section. It was a completely Hot-Wire grown p-i-n device deposited on a ZnO:Al coated (70nm) Asahi-U substrate. The back contact consisted in 70 nm ZnO:Al plus Ag/Al metallic contacts. Aluminium was added on top of the silver reflective contact as a protection as it outlasts the dry-etching process. Estimated thickness of both doped layers was around 70 nm and the total thickness of the p-i-n junction was 1.1 μm. Fig. 5.15 shows the J-V curve of the solar cell after dry etching. Best efficiency of 5.15% was achieved with J_{sc} = 17.4 mA/cm^2, V_{oc} = 0.47 V and FF = 0.63. The rest of the cells on the same substrate also exhibited efficiency values around 5%, indicating good reproducibility over the whole deposition area.

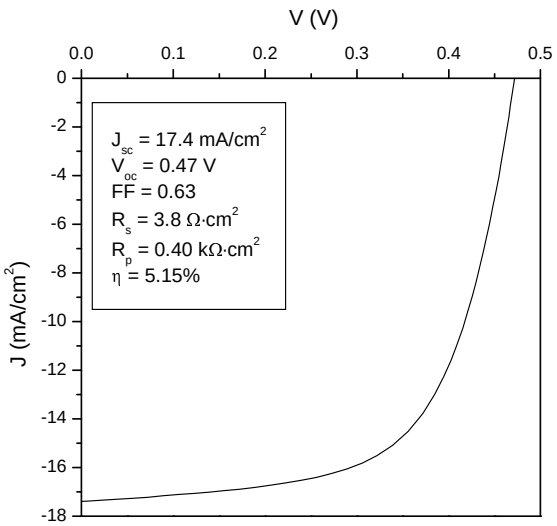

Fig. 5.15. J-V curve of a completely Hot-Wire grown p-i-n solar cell measured under 100 mW/cm^2 illumination. The intrinsic layer was deposited at T_f = 1600ºC, T_s = 200ºC, P = 3x10^{-2} mbar, $\phi(SiH_4)$ = 4 sccm and D_H = 94.4%. Active cell area was 0.096 cm^2.

Measurements kindly performed on this solar cell at the solar simulator of Universitat Politècnica de Catalunya (UPC) resulted in J_{sc} = 17.2 mA/cm^2, which were in agreement with those carried out in our laboratory. Figure 5.16 shows the external quantum efficiency of the device. The effect of the back reflector, tough non-optimised, was the cause of the enhanced carrier generation in the long-wavelength region (λ > 700 nm). On the contrary,

some effect imputable to a too thick p-type layer or a bad p-i interface was also observed in the low-wavelength regime (λ < 450 nm) pointing out that too much light was absorbed, and therefore wasted, before reaching the active layer of the device.

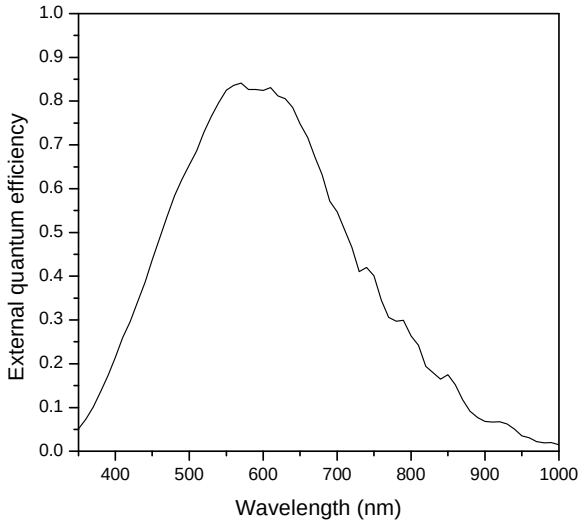

Fig. 5.16. Spectral response of a completely Hot-Wire grown p-i-n solar cell. The intrinsic layer was deposited at T_f = 1600ºC, T_s = 200ºC, P = 3x10^{-2} mbar, $\phi(SiH_4)$ = 4 sccm and D_H = 94.4%. Active cell area was 0.096 cm^2.

Stability of the cell upon light exposure has been demonstrated in the previous section of this chapter, where several drawbacks mainly attributable to problems outside the p-i-n junction or to possible doping diffusion coming from the p-type layer were also detected.

In this chapter, best efficiency of 5.15% has been reported for a completely Hot-Wire grown p-i-n solar cell with preliminary light trapping strategies. This result was achieved using nc-Si:H deposited close to the transition to amorphous growth using a tantalum wire in the low temperature deposition regime (T_f ~ 1600ºC, T_s = 200ºC).

There are a number of different possibilities to further increase the efficiency of the devices. Firstly, optimisation of the front and back contacts would decrease resistive losses and contact degradation. Furthermore, optimisation of the doped layers is necessary to avoid both optical losses and doping diffusion that limit the performance of the solar cells. Additionally, thanks to the low temperature deposition regime in which the highest quality material has been obtained, perspectives to grow devices onto flexible plastic substrates

should be also considered, which would require device deposition in the n-i-p configuration.

Best results in this work have been achieved with material grown at 1.1 Å/s, caused mainly by the reduced filament active area after the implementation of the protective funnel. Despite the low deposition rate, efficiency and stability observed indicated a drastic reduction in the amount of impurities incorporated during growth. Moreover, these results were reproducible over the whole substrate surface considered. Future perspectives should also consider the scaling of these results to larger substrate areas and higher deposition rates. This could be done by increasing the filament area, either changing its geometry or using multiple wires ensuring homogeneous deposition over larger areas.

Conclusions

In previous works it was proven that our solar cells mainly suffered from impurity incorporation during and after deposition. Therefore, different strategies heading towards the obtaining of impurity free nanocrystalline silicon have been presented:

- Several deposition regimes favouring layer density (increase in hydrogen dilution and decrease in total gas flow) were studied still using W as catalyst. Samples showing no oxygen incorporation after air exposure presented poor electrical features, what made them unsuitable to be implemented in solar cells.

- After the change of catalyst to Ta, studies of the effect of the hydrogen dilution and the substrate temperature pointed out promising properties at D_H = 95% and T_s = 200ºC, which were taken as a starting point for subsequent experiments.

- A change in the crystalline preferential orientation of the nc-Si:H samples from (111) to (220) was observed when decreasing the filament temperature for samples with thicknesses close to 1 μm. The transition took place, in the deposition conditions selected, around 1700ºC.

- Samples deposited at low T_f showed much higher resistance to oxygen incorporation after deposition whereas those grown at high T_f dramatically oxidised after air exposure. This effect was attributed to a difference in density of the amorphous tissue surrounding the grain boundaries caused by a possible change in the amount of SiH_3 produced at different filament temperatures. Unfortunately, the most compact layers (T_f ~ 1550-1600ºC) still suffered from impurity incorporation during growth, which affected the performance of the solar cells.

- Residual impurity incorporation (mainly O) coming from inside the deposition chamber was suppressed with the inclusion of the shielding funnel. The inclusion of the funnel did not affect the optimal deposition conditions. Implementation of intrinsic nc-Si:H deposited with the funnel in a p-i-n solar cell resulted in enhanced stability of the device both in dark and under AM1.5 illumination.

The substrate on which a sample is grown does influence the microstructure of the layer. Therefore, it can be concluded that results obtained from material characterisation on one substrate cannot be straightforwardly extrapolated to devices grown on other

substrates. This behaviour was observed by studying the transition from amorphous to nanocrystalline growth caused by a variation in the hydrogen dilution on different substrates (stainless steel, ZnO:Al, glass and Si).

- In the case of undoped samples, stainless steel seemed to enhance nanocrystalline growth, whereas to obtain nc-Si:H on glass, the highest amount of hydrogen was required. ZnO:Al and Si exhibited intermediate behaviours. Thus, identical process conditions can result in amorphous, half-crystalline or fully crystalline material depending on the substrate on which deposition took place.

- Identical experiments performed with doped layers evidenced a clear difference in behaviour depending on whether the doping gas considered was phosphine (n-type) or diborane (p-type). Electrical properties of the samples were in agreement with the transitions observed in the structural properties.

- Substrate dependence in n-type layers was similar to that observed in intrinsic layers, but with crystallisation taking place at lower hydrogen dilutions on all substrates considered. Phosphorous atoms acting as seeds for the nanocrystalline grains could be the cause of such early nucleation.

- On the contrary, higher hydrogen dilutions were required to obtain p-type nc-Si:H, attributable to amorphisation of the samples caused by the inclusion of diborane in the gas flow. Besides, contrary to what happened with n- and i-layers, glass seemed to enhance crystallinity of p-type samples and stainless steel was the substrate on which less crystalline fraction was measured.

- Scaling of doped layers to device size (~ 50 nm) maintaining good electrical properties was effectively carried out. For n-type layers σ_d = 5 S/cm and E_a = 0.02 eV were achieved in a 40 nm-thick sample, whereas σ_d = 2.5 S/cm and E_a = 0.04 eV were obtained in a 50 nm-thick p-type layer.

Finally, special effort has been paid to effectively increase the efficiency of our solar cells and to try to elucidate possible drawbacks affecting their performance.

- It has been demonstrated that the efficiency of a p-i-n solar cell can be effectively increased by the use of light-trapping strategies within the structure of the device (textured front contact and reflective back contact) and by avoiding losses due to the existence of leakage currents. ZnO:Al coated Asahi-U has been used as textured front contact and ZnO:Al/Ag/Al as a preliminary back reflector. Leakage currents have been effectively

reduced by dry-etching the devices in collaboration with the Universitat Politècnica de Catalunya.

- Study of the effect of the hydrogen dilution in a very narrow range of values (D_H = 95-93.5%) in the active layer of p-i-n devices have shown that, especially when working close to the transition to a-Si:H growth, even small changes in this parameter can lead to significant differences in the microstructure of the resulting samples.

- Light soaking experiments performed to evaluate the stability of devices with slightly different microstructure (deposited at D_H = 95, 94.4 and 93.8%) have proven that the p-i-n solar cells considered suffer from initial irreversible changes most likely attributable to chemical stabilisation of surfaces and interfaces like oxidation or doping diffusion into the active layer.

- From the three cases considered, only the solar cell with the active layer deposited using a hydrogen dilution of 93.8% showed noticeable defect creation upon light exposure. This effect was reversed after thermally annealing the sample at 180ºC. The influence of the amorphous tissue in the transport properties of nanocrystalline silicon seemed to be the cause of such misbehaviour. The threshold between the two different behaviours (stable and metastable) lay somewhere between 0.40 and 0.45 of crystalline fraction.

- Best efficiency achieved in preliminary devices including all these aspects was 5.15% in a completely Hot-Wire grown p-i-n solar cell deposited at low filament (1600ºC) and substrate (200ºC) temperatures. Different problems imputable to not properly optimised contacts and doped layers have been identified. Therefore, further optimisation of contacts, doped layers and thickness is required so that higher conversion efficiencies can be achieved. Additionally, taking into account the low deposition rate and the reproducibility of the device results over the whole substrate area, scaling of deposition rate and substrate surface to higher values could be done by increasing the active filament area.

Annexe I: Shutterless deposition of phosphorous-doped microcrystalline silicon by HWCVD

This part of the work is a summary of the results obtained during a 3-month stage at Debye Institute, SID – Physics of Devices at Utrecht University, The Netherlands. During the stage, first HW μc-Si:H n-type layers were deposited at the laboratory in Utrecht. Characterisation of the samples was carried both in Utrecht University and in Universitat de Barcelona. The result of this work can be also found in [Fonrodona et al., 2003].

I.1. Motivation and experimental set-up

Despite the fact that most of devices incorporating intrinsic active layers deposited by HWCVD use heavily doped layers deposited by PECVD [Klein et al., 2002, Niikura et al., 2002], HWCVD's advantages with respect to plasma deposition (higher deposition rates, lack of ion bombardment, greater ability to produce atomic hydrogen) could result in an improvement of a completely hot-wire grown device.

Aiming to obtain device-quality phosphorous-doped layers, a hot-wire assembly was implemented in the chamber assigned for n-type deposition of an ultra high vacuum multichamber system (PASTA). Figure I.1 shows the schematic cross-section of the chamber where both HWCVD and PECVD layers can be deposited. The hot-wire assembly consisted of two linear tantalum wires (0.3 mm diameter) 4 cm apart placed 1.5 cm below the substrate. Due to its internal arrangement, allowing both HW and PECVD process, no shutter was implemented in the chamber.

A shutter is commonly used to avoid deposition on the substrate during the first stages of the process, while deposition conditions have not stabilized. In the n-i-p solar cell configuration, the interface between the stainless steel substrate and the n-type layer does not play a critical role in the device performance. Besides, when scaling up these systems to large area deposition ones, shutters cannot be handled any more.

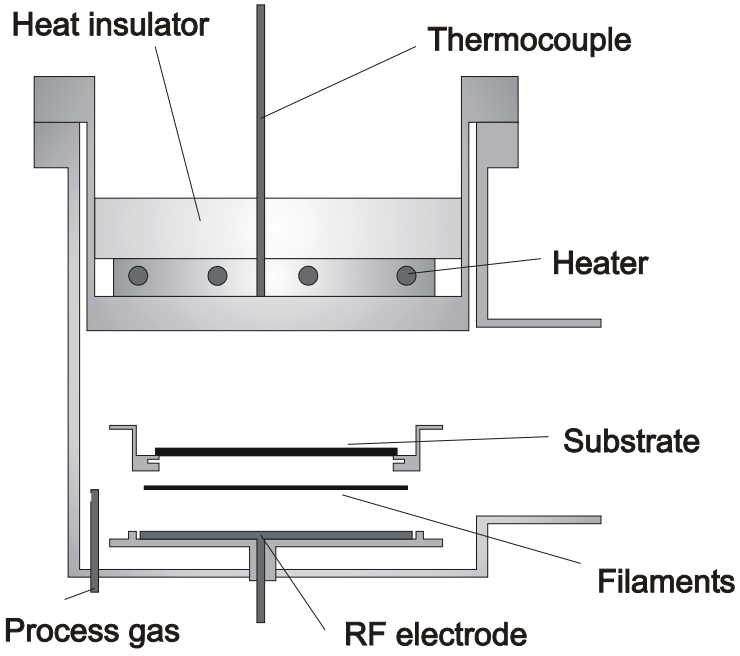

Fig. I.1. Schematic cross-section of the deposition chamber at Utrecht University.

In these shutterless conditions, prior to introducing the gases into the chamber, the filament was heated to the deposition temperature. Then, the gas mixture (H_2, SiH_4 and PH_3) was added and, finally, the process pressure was set. Hydrogen flow of 100 sccm and P = 0.1 mbar were used in all samples. Two different doping levels were considered, $[PH_3]/[SiH_4]$ = 0.48% and 0.92% in the gas phase. Filament temperature was 1850ºC except when the effect of this crucial parameter was studied. No heater or any other heat source but the wires themselves were used to heat the samples during deposition.

I.2. Results and discussion

μc-Si:H films were deposited on 10 cm x 10 cm Corning 1737 glass. The thickness of the films was also measured by reflection/transmission measurements, from which the refraction index (n_0) was also determined. Raman spectra were taken illuminating both from the top of the sample and through the glass. X_c was calculated as described in 2.4.1.

I.2.1. Thickness homogeneity

First studies carried out were those regarding the homogeneity of the samples. All layers exhibited a clear homogeneity in thickness, as illustrated in the thickness profile in figure I.2. This lack of homogeneity had as cause the fact that the filament-substrate distance (1.5 cm) was lower than the distance between the two wires (4 cm). Material grown between the wires presented slightly higher σ_d and lower X_c values than that grown directly above the wires. Conversely, material grown at the edge of the substrate had worse electrical and structural properties. This fact can be optimised in further experiments by adjusting the geometry of the hot-wire assembly. Results presented from now on refer, unless indicated otherwise, to material deposited right above the filament.

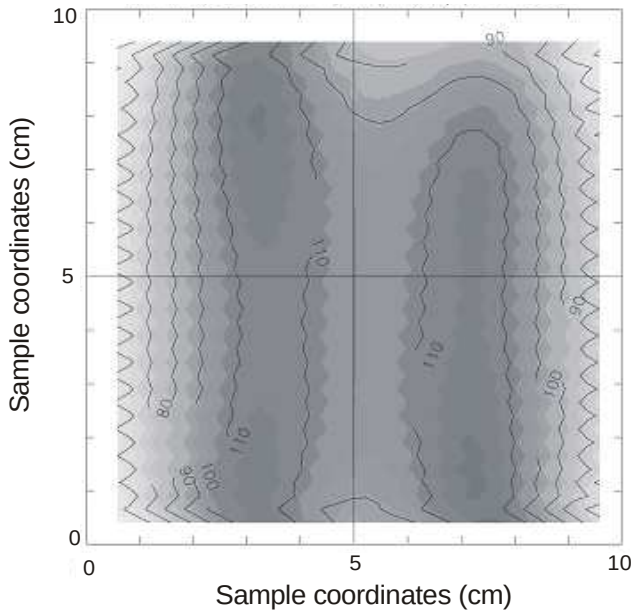

Fig I.2. Thickness profile of a μc-Si:H film. The numbers represent the relative thickness in %.

I.2.2. Effect of the starting sequence

In the shutterless geometry considered, deposition on the substrate started the moment SiH_4 entered the chamber. Different starting procedures have been tried in order to minimise the effect of the lack of control of the technological parameters when the gases are introduced into the chamber. For that purpose, two films were deposited, the only difference between them being the sequence in which the different gases were introduced

in the chamber. In one case, after the wire had been set to the process temperature, all gases were introduced at once whereas in the second case considered, silane was introduced in the chamber once hydrogen and phosphine flows had already stabilized.

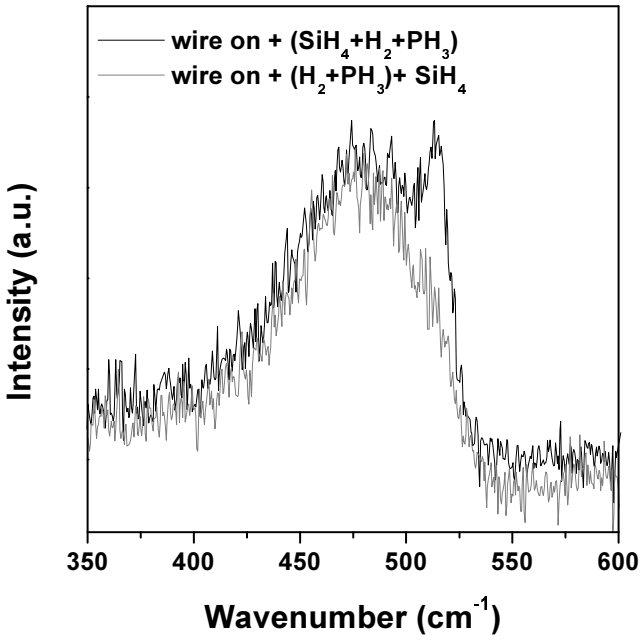

Fig. I.3. Raman spectra of samples deposited with different starting sequences. Deposition conditions in both cases were T_f = 1850ºC, P = 0.15 mbar, D_H = 95.2% and $[PH_3]/[SiH_4]$ = 0.24%. Both samples were 360 nm thick.

Figure I.3 shows the Raman spectra resulting from the different starting sequences. The first sequence considered, the introduction of the three process gases at once, resulted in a sample with X_c = 0.13. Conversely, the film grown having introduced SiH_4 after H_2 and PH_3 flows had stabilized was almost entirely amorphous. This difference in crystallinity could be attributed to the existence of a huge pressure peak in the latter the moment silane entered the chamber. One consequence of very high pressure is polymerisation. Therefore, initial deposition of large Si chains might decrease the number of nucleation centres and result in a more amorphous growth.

All samples analysed from this point on were deposited following the first sequence considered, i.e., first the filament was heated to the process temperature, then the gas mixture (H_2, SiH_4 and PH_3) was added at once and, finally, the process pressure was set.

I.2.3. Effect of the thickness

Uncontrolled deposition conditions in the first stages of the process might also affect the properties of the layers in the region close to the substrate. Therefore, thickness dependence of the crystalline fraction has been studied in order to elucidate whether the lack of shutter in our system caused the growth of material with poor structural properties during the first instants. 130, 50 and 20 nm thick layers were deposited using 2.5 sccm of silane (D_H = 97.5%), and a gas concentration of PH_3 of 0.48%. The rest of the deposition parameters were T_f = 1850ºC and P = 0.1 mbar. Crystallinity of the samples was determined from the Raman spectra taken both from the top of the sample and through the glass. The spectra acquired illuminating from the top of the sample are presented in figure I.4. X_c values obtained were 0.53 for the 130 nm thick layer and 0.25 for the 50 nm thick one. Values determined from the measurements through the glass were approximately 0.22 in both cases. Crystalline preferential orientation in these films was (111). On the contrary, the thinnest layer was clearly amorphous from both sides.

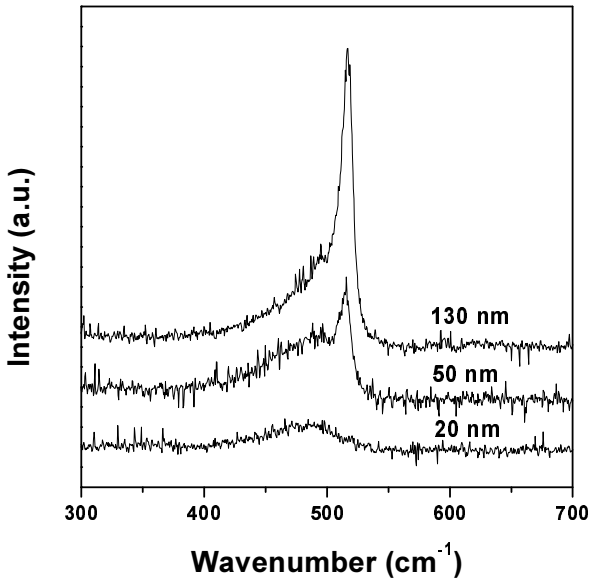

Fig. I.4. Evolution of the Raman spectra measured illuminating from the top of the sample with thickness.

Electrical measurements performed in the 50 nm thick sample (thickness suitable to be used in n-i-p solar cells) resulted in σ_d = 5.4 S/cm and E_a = 0.034 eV.

The same trend was observed using different deposition conditions (T_f = 1950ºC, D_H = 98.7% and $[PH_3]/[SiH_4]$ = 0.92%). In this case, a reduction in thickness caused a change from clearly microcrystalline electrical values at 50 nm (σ_d = 1.01 S/cm, E_a = 0.08 eV) to ones characteristic for amorphous material at 27 nm ($\sigma_d = 6.4x10^{-3}$ S/cm, E_a = 0.35 eV). This behaviour seemed to indicate the existence of an incubation layer with a thickness of around 20 nm. Incubation phase thickness observed in samples grown using a shutter at similar deposition conditions, with very high hydrogen dilution, is of tens of Å [Rath et al., 1998, Fonrodona et al., 2002].

I.2.4. The role of the filament temperature

Further studies of hydrogen dilution and doping concentration aiming to properly tune the deposition conditions showed that an optimum compromise between electrical and structural properties and deposition rate is found using D_H = 98.7% ($\phi(H_2)$ = 100 sccm and $\phi(SiH_4)$ = 1.3 sccm). Regarding the doping concentration, an increase of $[PH_3]/[SiH_4]$ from 0.48% to 0.92% resulted in an increment in σ_d from 2.4 to 7.2 S/cm while keeping the crystalline fraction almost constant (X_c = 0.51 and 0.48, respectively).

The following step to optimise the n-type μc-Si:H layers deposited without shutter was to study the effect of the Ta wire temperature in the best conditions found (P = 0.1 mbar, D_H = 98.7% and $[PH_3]/[SiH_4]$ = 0.92%). With this purpose, several samples approximately 50 nm thick were deposited in the range of T_f comprised between 1580 and 1950ºC. Figure I.5 shows the evolution of both dark conductivity and activation energy with T_f. Dark conductivity at room temperature increased with increasing T_f up to a value of 12.8 S/cm at 1770ºC. For higher temperatures, the conductivity decreased again to σ_d = 1 S/cm at 1950ºC. The activation energy presented a minimum at T_f = 1770ºC (E_a = 0.026 eV), increasing then to 0.08 eV at 1950ºC. Crystalline fraction values showed little differences in the range of temperatures studied. The sample deposited at the highest T_f turned out to be the most crystalline one (X_c = 0.59) whereas the minimum in X_c was found for the layer grown at 1770ºC (X_c = 0.46). The refraction index calculated from the reflection/transmission measurements also had its maximum at the same T_f. This trend seemed to indicate that μc-Si:H grown around this wire temperature had a slightly bigger amount of amorphous phase (i.e., less crystalline fraction) but that the amorphous tissue is denser (maximum in the refraction index).

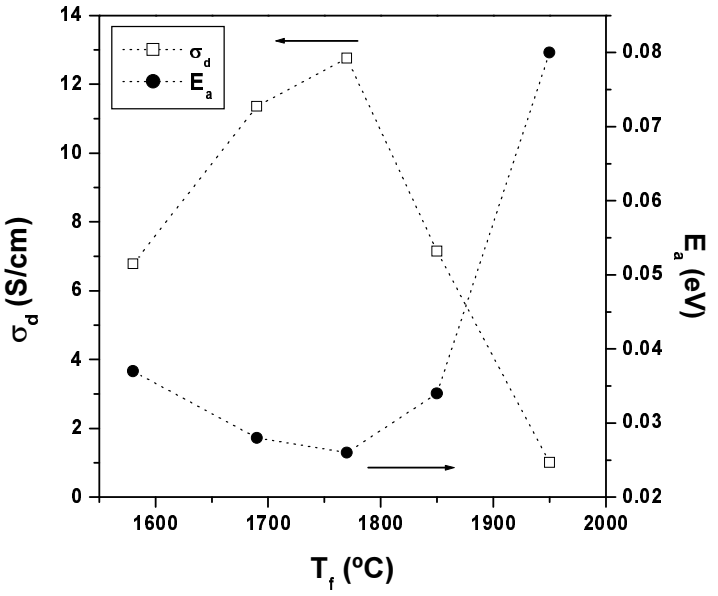

Fig. I.5. Dark conductivity at room temperature (σ_d) and activation energy (E_a) as a function of the filament temperature. The rest of the deposition conditions are P = 0.1 mbar, D_H = 98.7% and $[PH_3]/[SiH_4]$ = 0.92%. Lines are set as a guide for the eye.

Phosphorous-doped μc-Si:H deposited under optimised conditions exhibited dark conductivity and activation energy values (12.8 S/cm and 0.026 eV in 50 nm thick films grown at 1 Å/s) that make them suitable to be included in a solar cell. These features were comparable to those obtained in PECVD n-type layers (25 S/cm and 0.02 eV in 50 nm thick films grown at 0.16 Å/s) deposited in the same chamber.

I.3. Conclusions

A hot-wire assembly was implemented in one of the chambers of the PASTA system at Utrecht University, allowing PECVD and HW deposition of thin silicon films in the same chamber. Due to its internal arrangement, the deposition chamber was shutterless.

An incubation layer of approximately 20 nm might be the result of the uncontrolled conditions caused by the lack of shutter during the first stages of deposition. The sequence in which the gases were introduced in the chamber caused changes in the film structure.

Therefore, even though the presence of a shutter in the deposition chamber might be advisable to prevent the above-mentioned effects, its presence is not strictly necessary to obtain n-type μc-Si:H suitable to be implemented in solar cells. This result is of special interest when dealing with large area deposition systems, where a shutter cannot be handled.

50 nm thick n-type μc-Si:H with good electrical and structural properties was obtained by properly tuning the deposition conditions. Best values obtained make this material suitable to be used in photovoltaic devices. Preliminary results concerning the inclusion of these HWCVD grown n-type μc-Si:H layers in n-i-p structured solar cells on flexible stainless steel substrates can be found in [Veen, 2003].

Annexe II: Low Temperature Cat-CVD

In this annexe, preliminary trials to grow thin silicon films from silane decomposition upon collision with atomic hydrogen generated using titanium as catalyst, what will be called Low Temperature Cat-CVD, will be considered.

II.1. Motivation

Silicide formation in the cold ends of the filaments leading to contamination of the deposited materials and to an early breakage of the wire can be effectively prevented by avoiding any contact of the incoming SiH_4 gas flow with the colder parts of the wire. A first approximation to this goal is the inclusion of protective shields like the box described in [Guillet et al., 2000] or the funnel designed in section 2.2.2. A step further in this path is found in the design of the catalyst together with the gas inlet, like in [Ishibashi, 2001], where H_2 and NH_3 are introduced into the chamber close to the catalyst terminals, therefore preventing SiH_4 molecules from colliding with the cold ends of the wire.

SiH_3, which is also believed to be the main precursor of device-quality material in HWCVD, is supposed not to be directly generated on the catalyst but from the secondary reaction $SiH_4 + H \rightarrow SiH_3 + H_2$ [Masuda et al., 2002]. This fact, together with the fact that H production in HWCVD is one or two orders of magnitude higher than in PECVD can lead to the conclusion that no catalyst is indeed needed for the decomposition of SiH_4 molecules as far as there is a large enough amount of H atoms supplied [Masuda et al., 2002]. This statement can lead to the design of alternative low-temperature processes for thin silicon film deposition.

II.2. Design of the catalytic tube

The main idea of what we call Low-Temperature Catalytic CVD (LTCat-CVD) is the separate decomposition of hydrogen and silane inside the chamber. In this variation of Cat-CVD, a titanium tube heated by means of a Ta wire is used as a catalyst to decompose H_2 into atomic H. With this arrangement, there is no need of what is commonly known as a hot-wire (the Ta filament is heated to much lower temperatures than the ones used in

HWCVD) that might interact with SiH_4 molecules. Thus, in this case, the term Catalytic CVD is more adequate to describe the process.

Figure II.1 shows a scheme of the LTCat-CVD catalyst. A Ti tub is connected to the gas inlet and shielded with a ceramic protection. The tube is heated by a Ta wire and its temperature (T_{Ti}) is measured with a thermocouple attached to it. H_2 is catalytically decomposed into atomic hydrogen when crossing the heated tube. A new gas inlet into the chamber, parallel to the substrate holder, has also been included in the internal arrangement so that SiH_4 can be introduced into the chamber either through this new inlet or through the Ti tube. Summarising, in LTCat-CVD hydrogen molecules are catalytically decomposed into atomic hydrogen by a heated titanium tube. Silicon growth is expected from the secondary reactions taking place upon collision of H atoms with SiH_4 molecules.

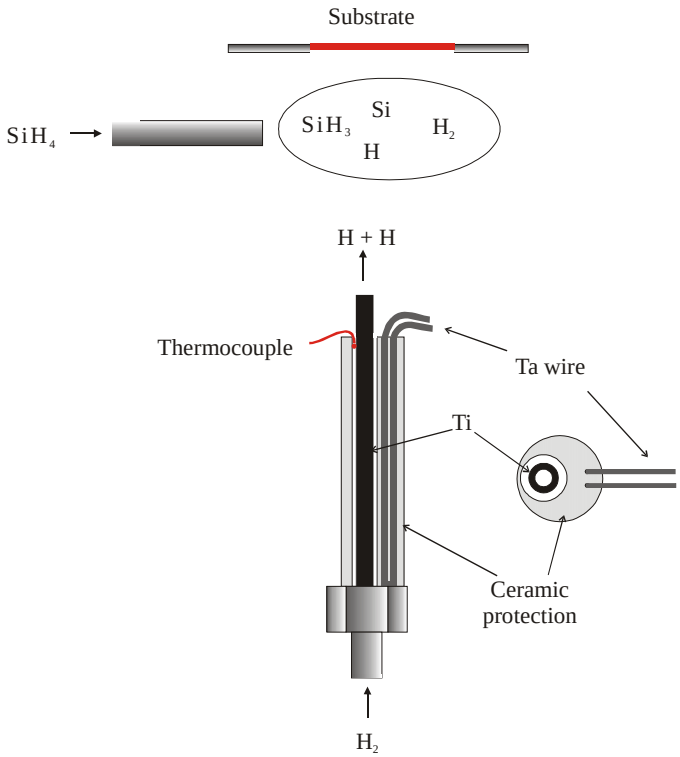

Fig. II.1 Design of the catalytic tube for Low-Temperature Catalytic CVD.

The evolution of T_{Ti} as a function of the intensity through the tantalum wire is shown in figure II.2. The calibration was carried out both at base pressure and in a hydrogen atmosphere. The temperature value measured at a certain intensity was pressure-dependent,

being approximately 25ºC lower with hydrogen at P = $1.8x10^{-2}$ mbar than with no gas at the base pressure. The dependence of T_{Ti} with the wire intensity seemed to follow a linear behaviour for temperatures higher than 150ºC. In both cases the substrate temperature was set at 300ºC and the measure was taken after the temperature had stabilised. The substrate temperature chosen was the main cause that T_{Ti} = 110ºC was gauged with the filament off.

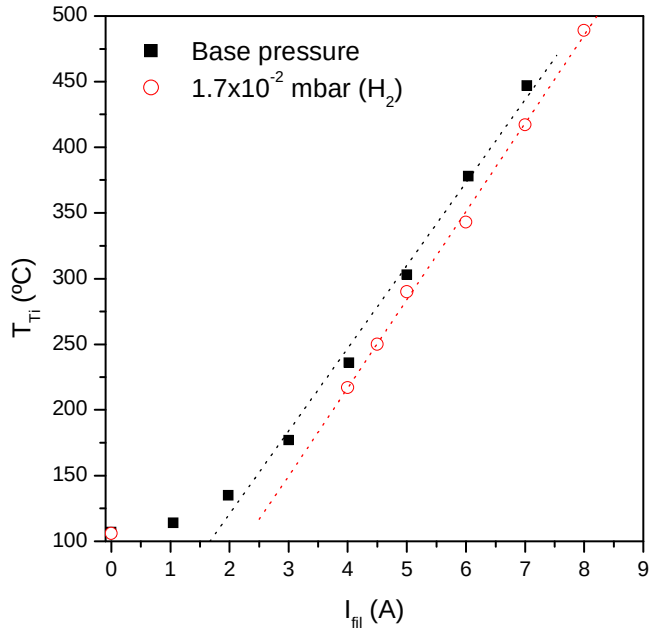

Fig. II.2. Calibration of the titanium temperature as a function of the filament intensity at different pressures. The substrate temperature was set at 300ºC.

II.3. H_2 decomposition

First step in the study of LTCat-CVD was to verify whether the catalytic tube effectively decomposed H_2 into H and the possible effect of T_{Ti} in the production of atomic hydrogen. Therefore, SnO_2 was used as a detector of atomic hydrogen inside the chamber, as it drastically darkens under a strong reducing ambient, like HWCVD process [Masuda et al., 2002b]. Hence, SnO_2 layers were exposed to a 15-minute hydrogen treatment (20 sccm H_2 at P = $1.8x10^{-2}$ mbar) at different T_{Ti} values. Transmission measurements were performed to the SnO_2 samples after hydrogen treatment. Transmittance spectra obtained at different T_{Ti} values are represented in figure II.3. The spectrum of a SnO_2 substrate exposed to 15 minutes of hydrogen decomposition by means of a tantalum wire heated at the usual process temperature (1650ºC) is also included for comparison.

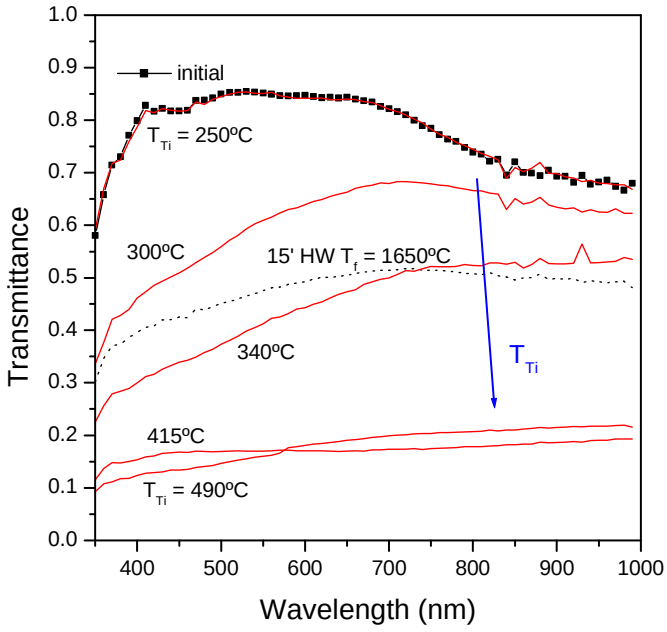

Fig. II.3. Transmittance spectra of SnO_2 layers after 15 minutes of hydrogen treatment at different T_{Ti}. The effect of the exposure to a hot-wire heated at 1650ºC for 15 minutes is also plotted for comparison.

No effect in the SnO_2 transmittance was observed at temperatures below 250ºC, indicating that there was not enough atomic hydrogen produced, if any, to reduce the tin oxide. For $T_{Ti} \geq 300$ºC, the transmittance of the layers decreased with increasing temperature. A minimum in the transmittance was reached for T_{Ti} above 400ºC, as not much difference was seen after increasing the titanium temperature from 415 to 490ºC. This fact seemed to point to the decomposition of all the H_2 crossing the catalytic tube for $T_{Ti} \geq 415$ºC. The comparison of the transmittance spectra obtained at $T_{Ti} = 340$ºC and with the hot-wire at $T_f = 1650$ºC ($\phi(H_2) = 20$ sccm, $P = 1.8 \times 10^{-2}$ mbar and $T_s = 300$ºC for 15 minutes in both cases) seemed to indicate that nearly the same amount of H_2 is decomposed in both cases.

Once the efficient decomposition H_2 molecules into atomic hydrogen had been proved, next step was to try to grow some kind of thin silicon film from the reactions taking place between H atoms and SiH_4 molecules.

II.4. Si deposition

First and very preliminary attempts to grow silicon by LTCat-CVD were carried out after verifying atomic hydrogen production. The regime chosen was that ensuring high atomic hydrogen production, so that it could interact with silane via the reaction $SiH_4 + H \rightarrow SiH_3 + H_2$. Therefore, taking into account the transmittance results presented in fig. II.3, the titanium tube temperature chosen was $T_{Ti} \sim 400^oC$ (corresponding to a current of 7 A through the tantalum wire according to the calibration in fig. II.2).

Titanium temperature	~400ºC
Substrate temperature	400ºC
Pressure	1 mbar
Hydrogen flow	20 sccm
Silane flow	8 sccm

Table II.1. Deposition conditions in first attempts of silicon deposition by LTCat-CVD.

Deposition conditions are summarised in table II.1. Moderately high substrate temperature (400ºC) was chosen aiming to the possible growth of dense silicon (as high substrate temperatures enhance hydrogen desorption from the surface of the substrate). A high process pressure was likely to increment the collision probability of atomic hydrogen with incoming silane molecules and the secondary reactions, thus favouring the production of radicals that could contribute to the growth of a thin silicon film. In this experiment, silane entered the chamber via the new lateral inlet.

Substrates considered were Corning 1737 glass and stainless steel. Thirty minutes of LTCat-CVD process at the deposition conditions mentioned in table II.1 resulted in an extremely thin layer, with thickness below the resolution limit of our profilometer. Apparently no appreciable deposition took place after increasing the deposition time four times. Surface etching by atomic hydrogen with an etching rate higher than the silicon deposition rate could be the responsible for this behaviour.

Figure II.4 shows the transmittance spectra of a plain glass and the LTCat-CVD silicon layer. Due to the thinness of the layer, no interference fringes were seen, only a decrease in the transmittance in the region of 400-500 nm evidencing the presence of a very thin semiconductor layer on the glass substrate.

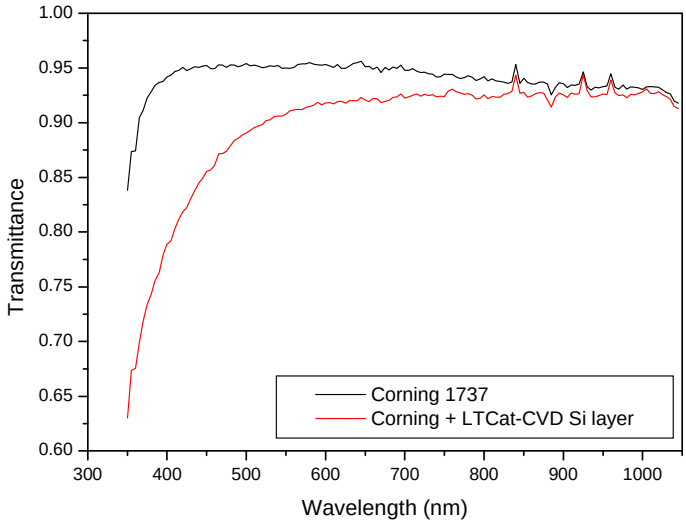

Fig. II.4. Transmittance spectra of Corning 1737 glass and that of a LTCat-CVD thin silicon film.

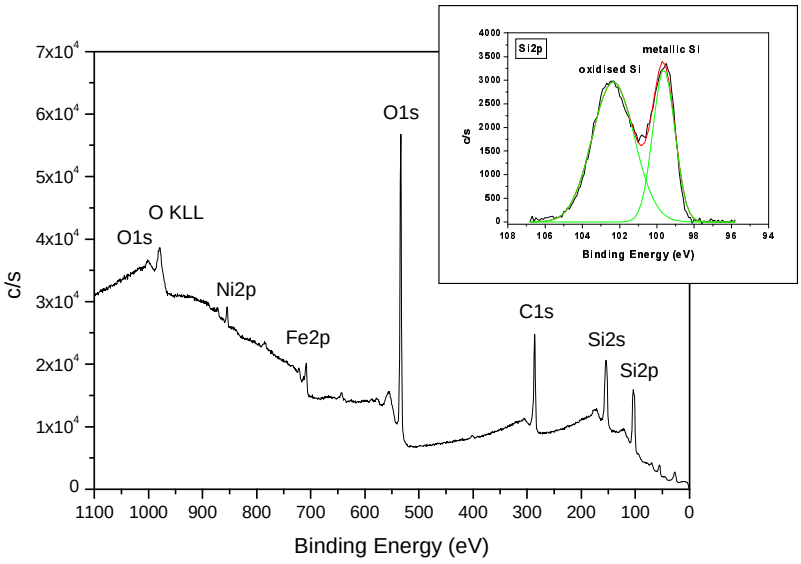

Fig. II.5. Superficial XPS analysis of the LTCat-CVD sample on stainless steel. The inset shows the region of the Si2p band, where the contributions corresponding to oxidised and metallically bonded silicon are seen.

XPS measurements evidenced silicon deposition on stainless steel, as can be seen in figure II.5. Apart from silicon, carbon attached to the surface upon exposure to the

atmosphere and several metallic contributions attributable to the stainless steel substrate were observed. The inset in fig. II.5 shows the region of the Si2p band, where a double contribution was detected corresponding to oxidised (~102.7 eV) and metallic silicon (~99.9 eV). The relation between the two contributions calculated by fitting gaussian curves was 60% of the total silicon detected bonded to oxygen.

Silicon deposited onto the substrates was due to interaction between the atomic hydrogen with the silane molecules. Additionally to that mechanism, a second kind of silicon deposition took place inside the chamber by thermal CVD of silane. Pyrolysis of silane happened in contact with the hottest parts of the set-up ($T \geq 700^{o}C$) resulting in silicon deposition on the tantalum wire and on the outer part of the ceramic insulator closer to the wire.

In this annexe, very preliminary results regarding what we called Low-Temperature Cat-CVD have been presented. Extremely low deposition rates achieved discard this technique as a feasible alternative to HWCVD or PECVD. Nevertheless, it has only been demonstrated that silicon thin films can be deposited using this method. Any trial to optimise material grown by this technique is beyond the scope of the present thesis.

Annexe III: Variable Illumination Measurement technique (VIM)

III.1. Qualitative approach

The main drawback of a-Si:H is the fact that the electronic properties degrade when the material is exposed to light: the so-called Staebler-Wronski effect [Staebler and Wronski, 1977]. Fortunately, when nc-Si:H with high crystalline fractions is considered, the Staebler-Wronski effect does not play an important role in the stability of the device, as we have not observed any degradation effect under light soaking attributable to an increase in the defect density [Voz, 2001]. On the other hand, light induced degradation of nc-Si:H solar cells with high amorphous volume fraction up to 10% of the initial efficiency ascribable to Staebler-Wronski like defect generation in the amorphous phase has been reported [Klein et al., 2003].

The Variable Illumination Measurement (VIM) method has been used to assess any possible degradation in our devices attributable to light induced defect creation. Besides, this technique also allows to successfully discriminate other effects that might also influence the performance of a solar cell, like sheet resistance of electrodes or parallel resistance due to leakage currents. The VIM method mainly consists in the acquisition of J-V curves over a wide range of illumination levels, from which the open circuit voltage (V_{oc}), fill factor (FF), differential resistance in short circuit (R_{sc}) and differential resistance in open circuit (R_{oc}) are determined and represented as a function of the short circuit current density (J_{sc}) [Merten et al., 1998]. Figure III.1 shows how the different parameters are determined from each J-V curve.

The behaviour of electronic devices is commonly described using equivalent circuits. An ideal solar cell would be modelled by a diode plus a current source connected in parallel representing the photogenerated current. When dealing with real devices, some terms need to be added to that simple circuit: parasitic parallel and series resistance should be taken into account. The first one is of special importance in thin film structures, where shunting paths are easily formed, whereas the latter takes into account the voltage drop in the electrodes and the contact resistance. As recombination is relatively intense within low mobility a-Si:H and nc-Si:H due to the relatively high concentration of recombination

centres, an additional recombination loss term should also be included into the model [Merten et al., 1998]. This last term is symbolised by the current sink in dash lines in figure III.2.

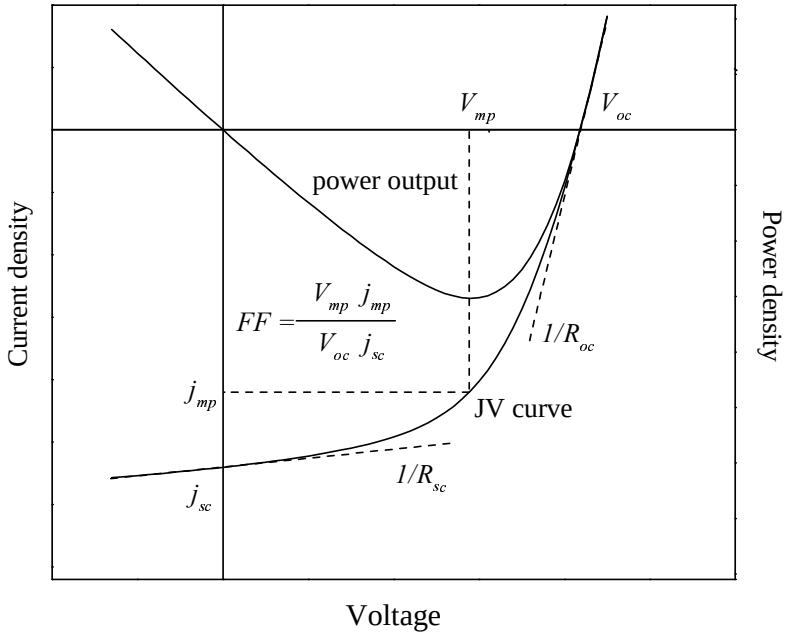

Fig. III.1. Parameters determined from each J-V curve acquired in a VIM measurement.

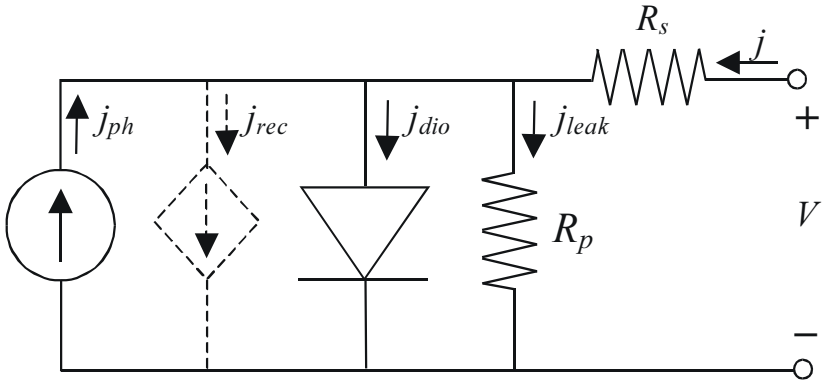

Fig. III.2. Equivalent circuit for a low mobility thin film solar cell, where a recombination term (dashed) has been added to take into account the recombination within the active layer.

Different effects (Staebler-Wronski, sheet resistance of electrodes, parallel resistance due to leakage currents) can be successfully discriminated from the VIM measurements

and from the comparison of the obtained curves in the initial and degraded states. An extensive explanation of the different effects degradation has on the performance of a solar cell can be found in [Merten et al., 1998]. Nevertheless, the main effects light soaking causes in an a-Si:H cell are set in figure III.3 as an example (data extracted from [Merten et al., 1998]).

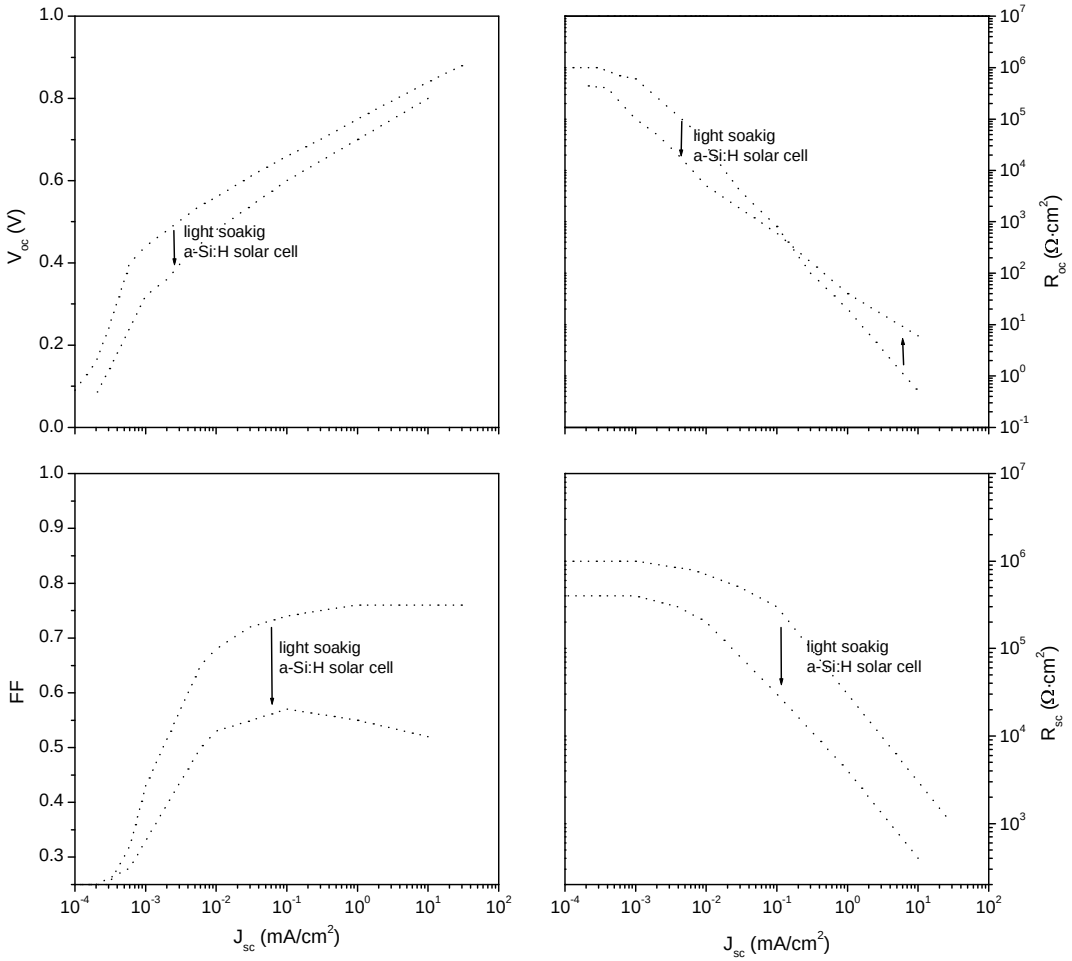

Fig. III.3. VIM measurements illustrating the degradation effects suffered when an a-Si:H solar cell is exposed to illumination (extracted from [Merten et al., 1998]).

In VIM analysis, results concerning the active layer of the device are deduced from the so-called intermediate illumination regime, which approximately corresponds to the normal operating regime of a solar cell (J_{sc} in the range of 0.1-10 mA/cm^2). On the other hand, conclusions related to parasitic resistance effects are deduced from very low

illumination levels (J_{sc} lower than 10^{-3} mA/cm^2) in the case of parallel resistance effects and very high illumination levels (J_{sc} around 100 mA/cm^2 and higher) for series resistance effects.

The drop in the FF and R_{sc} values after light exposure in the intermediate illumination regime is a clear symptom of light induced defect creation in the i-layer (Staebler-Wronski degradation). On the other hand, a decrease in the V_{oc} curve, which gives information about the diode performance, indicates diode degradation mainly imputable to the doped layers.

The low illumination limit of R_{sc} corresponds to the parallel resistance (R_p), which is a measure of the technological quality of the device, indicating low R_p values the existence of leakage currents within the cell. A decrease in this parameter at low illuminations indicates an increase in the leakage currents. One possible explanation of this behaviour is the creation of pinholes during degradation. The high illumination limit of R_{oc} corresponds to the series resistance (R_s) of the device. This parameter is physically determined by the sheet resistance of the electrodes, especially that of the TCO. A continuous increase of R_s is attributed to degradation effects outside the p-i-n junction (TCO or metallic contacts).

III.2. Defect evaluation using VIM

Taking a deeper look at the behaviour of the short circuit resistance, it is known that the dependence of R_{sc} on J_{sc} is usually affected by the lateral leakages at low illumination levels and by resistive losses at the contacts at high illumination levels. Anyway, in the case of a good p-i-n cell, the behaviour of this curve at intermediate illumination levels does not depend on this parasitic effects, and, therefore, the $R_{sc} \cdot J_{sc}$ product (the collection potential, V_c [Hof et al., 2000]) is also independent of the illumination level and can be expressed as a function of the carrier transport and recombination parameters [Merten et al., 1998, Asensi et al., 1999]:

$$V_c = R_{sc} \cdot J_{sc} = \frac{\mu \tau_{eff} \cdot V_{bi}^2}{L^2} \qquad \text{(III.1)}$$

where V_{bi} stands for the built-in potential, L is the thickness of the cell and $\mu\tau_{eff}$ is the effective mobility-lifetime product of the carriers in the intrinsic zone, which can be expressed as a function of the defect density by:

$$\mu\tau_{eff} = 2\frac{\mu_n^0\tau_n^0 \cdot \mu_p^0\tau_p^0}{\mu_n^0\tau_n^0 + \mu_p^0\tau_p^0} \tag{III.2}$$

with

$$\tau_n^0 = \frac{1}{v_{th}\sigma_n^0 N_{DB}},\ \tau_p^0 = \frac{1}{v_{th}\sigma_p^0 N_{DB}} \tag{III.3}$$

Using the common values of the thermal velocity of the carriers ($\nu_{th}=10^7$ cm/s) and the capture cross sections of the neutral dangling bond for electrons and holes (σ_n^0 = 5x10^{-16} cm^2, σ_p^0 = 10^{-16} cm^2) and considering carrier mobility close to 1 cm^{2}V^{-1}s^{-1} and V_{bi} = 1.1 eV (as doped layers used were heavily doped), the collection potential can be directly related to the dangling bond density (N_{DB}) by:

$$N_{DB} = 3.0 \cdot 10^8 (V^{-1}cm^{-1}) \cdot \frac{V_{bi}^2}{V_{c0} \cdot L^2} \tag{III.4}$$

were V_{c0} stands for the value the collection potential would have at intermediate illumination level, i.e., without any parasitic effect.

For amorphous silicon p-i-n solar cells it has been demonstrated that light induced creation of defects can be easily quantified with this method, resulting in a difference of one order of magnitude between the initial and the stabilized density of defects after long time light exposure [Merten et al., 1998].

III.3. Solar cell analysis from the V_c curve

The collection potential ($V_c = J_{sc} \cdot R_{sc}$) is related to the carrier recombination in defects. In a simple model, it is assumed that the dominant mechanism in carrier recombination is

the recombination in neutral defects (D^0), mechanism that is indeed dominant when considering the high injection regime (high illumination levels). Nevertheless, in the low injection regime, recombination in charged defects near the p-i and i-n interfaces becomes the dominant mechanism [Asensi et al., 1999].

Recombination mechanisms and other effects that might affect the performance of a solar cell have been evaluated taking into account the definition of collection potential and a model for the short circuit resistance (R_{sc}). In this model, all the different contributions that affect the short circuit resistance have been taken into account:

- recombination in defect states
- lateral leakages in the p-i-n junction, which are generally modelled as a parasitic parallel resistance (R_p)
- series resistance (R_s) due to resistive losses at the contacts.

When analysing the recombination effects existing in a p-i-n junction, two different contributions need to be considered. First of all, the recombination in neutral defects within the volume of the active layer of the solar cell, which is the dominant mechanism at intermediate and high illumination levels. The second contribution is that of recombination in charged states. Inclusion of this term is a consequence of the fact that, at low illumination levels, most of the recombination occurs close to the interfaces where the defects are charged [Asensi et al., 1999].

Taking into account all the different contributions to R_{sc}, we have modelled its behaviour with the expression (III.5):

$$R_{sc} = \frac{1}{\frac{J_{sc}}{V_{c0}} + \frac{J_{sc}^{1/2}}{\gamma V_{c0}} + \frac{1}{R_p}} + R_s \qquad \text{(III.5)}$$

where the term J_{sc}/V_{c0} takes into account recombination in neutral defects within the volume of the active layer of the solar cell, dominant at intermediate and high illumination levels. Relation between R_{sc} and J_{sc} in this regime is that expressed in equation (III.1).

The effect of recombination in charged states is considered in the second term ($J_{sc}^{1/2}/\gamma V_{c0}$). In this term, the assumption that the recombination in the charged defects depends on the illumination level has been made, as charged regions shrink with increasing illumination. The dependence $J_{sc}^{1/2}$ is merely phenomenological, and its exactness is still

under study. The parameter γ indicates the relative importance of this mechanism, being the recombination in charged defects more important for lower values of γ.

The collection potential $V_c(J_{sc}) = R_{sc} \cdot J_{sc}$, instead of R_{sc}, is what is actually chosen to illustrate the different effects considered in equation (III.5), as effects are more clearly seen in the V_c plot. Therefore, what has been plotted in this work was:

$$V_c(J_{sc}) = J_{sc} \cdot R_{sc} = \frac{J_{sc}}{\frac{J_{sc}}{V_{c0}} + \frac{J_{sc}^{1/2}}{\gamma V_{c0}} + \frac{1}{R_p}} + J_{sc} \cdot R_s \qquad \text{(III.6)}$$

Fit has been done by manually adjusting the different parameters (V_{c0}, γ, R_p and R_s) taking into account their effect in the V_c curve. V_{c0} is directly related with the maximum value of the curve whereas R_s is responsible for a sharp drop at high illumination, sharper for higher R_s values. Higher values of R_p cause a shift towards lower illuminations of the V_c curve, and γ is related to its slope, the higher the importance of the recombination in charged states (therefore, the lower γ), the lower the slope.

References

Aberle A.G., Harden N.P., Oelting S., J. Cryst. Growth **226**, 209 (2001)

Ahn J.Y., Jun K.H., Lim K.S., Konagay M., Appl. Phys. Lett. **82**, 1718 (2003)

Alpuim P., Chu V., Conde J.P., J. Appl. Phys. **86**, 3812 (1999)

Asensi J.M., Merten J., Voz C., Andreu J., J. Appl. Phys. **85**, 2939 (1999)

Baia Neto A.L., Lambertz A., Carius R., Finger F., J. Non-Cryst. Solids **299-302**, 274 (2002)

Bailat J., Vallat-Sauvain E., Feitknecht L., Droz C., Shah A., J. Non-Cryst. Solids **299-302**, 1219 (2002)

Bauer S., Schröder B., Herbst W., Lill M., Proceedings of the 2nd World Conference on Photovoltaic Solar Energy Conversion, Vienna (H.S. Stephens and Associates, Bedford, UK), p.363 (1998)

Brühne K., Schubert M.B., Köhler C., Werner J.H., Thin Solid Films **395**, 163 (2001)

Bustarret E., Hachicha M.A., Brunel M., Appl. Phys. Lett. **52**, 1675 (1988)

Brüggemann R., Kleider J.P., Longeaud C., Mencaraglia D., Guillet J., Bourée J.E., Niikura C., J. Non-Cryst. Solids **266-269**, 258 (2000)

Cheng H.C., Huang C.Y., Wang F.S., Lin K.H., Tarntair F.G., Jpn. J. Appl. Phys. **39**, L19 (2000)

Cifre J., Bertomeu J., Puigdollers J., Polo M.C., Andreu J., Lloret A., Appl. Phys. A **59**, 645 (1994)

Cullity B.D., "Elements of X-ray diffraction" (Addison-Wesley, Boston 1977)

Curtins H., Veprek S., Solid State Comm. **57**, 215 (1986)

Diehl F., Scheib M., Schröder B., Oechsner H., J. Non-Cryst. Solids **227-230**, 973 (1998)

Dirani E.A.T., Andrade A.M., Noda L.K., Fonseca F.J., Santos P.S., J. Non-Cryst. Solids **273**, 307 (2000)

Dyer T.E., Marshall J.M., Pickin W., Hepburn A.R., Davies J.F., J. Non-Cryst. Solids **164-166**, 1001 (1993)

Finger F., Klein S., Dylla T., Baia Neto A.L., Vetterl O., Carius R., Mater. Res. Soc. Symp. Proc. **715** A26.2 (2002)

Fonrodona M., Soler D., Asensi J.M., Bertomeu J., Andreu J., J. Non-Cryst. Solids **299-302**, 14 (2002)

Fonrodona M., Gordijn A., van Veen M., van der Werf C.H.M., Bertomeu J., Andreu J., Schropp R.E.I., Thin Solid Films **430**, 145 (2003)

Fontcuberta i Morral A., Hofmeister H., Roca i Cabarrocas P., J. Non-Cryst. Solids **299-302**, 284 (2002)

Goetzberger A., Hebling C., Schock H.W., Mat. Sci. Eng. **R40**, 1 (2003)

Guillet J., Saha S.C., Equer B., Bourée J.E., Kleider J.P., Longeaud, Proceedings of the 2nd World Conference on Photovoltaic Solar Energy Conversion, Vienna (H.S. Stephens and Associates, Bedford, UK), p. 826 (1998)

Guillet J., Niikura C., Bourée J.E., Kleider J.P., Longeaud C., Brüggemann R., Mat. Sci. Eng. **B69-70**, 284 (2000)

Han D., Yue G., Lorentzen J.D., Lin J., Habuchi H., Wang Q., J. Appl. Phys. **87**, 1882 (2000)

He A., Heya A., Otsuka N., Matsumura H., Jpn. J. Appl. Phys. **37**, 92 (1998)

Hegedus S., Buchanan W., Eser E., Proc. 26th IEEE PVSC, Anaheim (USA), p. 603 (1997)

Hof Ch., Wyrsch N., Shah A., J. Non-Cryst. Solids **266-269**, 1114 (2000)

Honda N., Masuda A., Matsumura H., J. Non-Cryst. Solids **266-269**, 100 (2000)

Hsiao H.L., Hwang H.L., Yang A.B., Chen L.W., Yew T.R., Appl. Surf. Sci. **142**, 316 (1999)

Ishibashi K., Thin Solid Films **395**, 55 (2001)

Klein S., Wolff J., Finger F., Carius R., Wagner H., Stutzmann M., Jpn. J. Appl. Phys. **41**, L10 (2001)

Klein S., Finger F., Carius B., Rech B., Houben L., Luysberg M., Stutzmann M., Mat. Res. Soc. Symp. Proc. **715**, A26.2 (2002)

Klein S., Wolff J., Finger F., Carius R., Wagner H., Stutzmann M., Jpn. J. Appl. Phys. **41**, L10 (2002b)

Klein S., Finger F., Carius R., Dylla T., Rech B., Grimm M., Houben L., Stutzmann M., Thin Solid Films **430**, 202 (2003)

Kluth O., Rech B., Houben L., Wieder S., Schöpe G., Beneking C., Wagner H., Löffl A., Schock H.W., Thin Solid Films **351**, 247 (1999)

Kondo M., Toyoshima Y., Matsuda A., Ikuta Z., J. Appl. Phys. **80**, 6061 (1996)

Martins R., Ferreira I., Fernandes F., Fortunato E., J. Non-Cryst. Solids **227-230**, 901 (1998)

Masuda A., Ishibashi K., Matsumura H., Mat. Res. Soc. Symp. Proc. **609**, A6.3 (2000)

Masuda A., Izumi A., Umemoto H., Matsumura H., Vacuum **66**, 293 (2002)

Masuda A., Imamori K., Matsumura H., Thin Solid Films **411**, 166 (2002b)

Matsumura H., J. Appl. Phys. **65**, 4396 (1989)

Matsumura H., Jpn. J. Appl. Phys. **30**, 1522 (1991)

Matsumura H., Jpn. J. Appl. Phys. **37**, 3175 (1998)

Matsumura H., Umemoto H., Izumi A., Masuda A., Thin Solid Films **430**, 7 (2003)

Meier J., Kroll U., Dubail S., Golay S., Fay S., Dubail J., Shah A., Proc. 28th IEEE PVSC, Anchorage (USA), 746 (2000)

Meier J., Vallat-Sauvain E., Dubail S., Kroll U., Dubail J., Golay S., Feitnecht L., Torres P., Fay S., Fischer D., Shah A., Solar Energy Materials and Solar Cells **66**, 73 (2001)

Meier J., Dubail S., Golay S., Kroll U., Fay S., Vallat-Sauvain E., Feitknecht L., Dubail J., Shah A., Solar Energy Materials and Solar Cells **74**, 457 (2002)

Merten J., Asensi J.M., Voz C., Shah A., Platz R., Andreu J., IEEE Transactions on Electron Devices, **Vol. 45**, No 2, 423 (1998)

Minami T., Sato H., Nanto H., Takata S., Thin Solid Films **176**, 277 (1989)

Morrison S., Madan A., J. Vac. Sci. Technol. **A19,** 2817 (2001)

Nasuno Y., Kondo M., Matsuda A., Jpn. J. Appl. Phys. **41**, 5912 (2002)

Niikura C., Brenot R., Guillet J., Bourée J.E., Kleider J.P., Brüggemann R., Longeaud C., Solar Energy Materials and Solar Cells **66**, 421 (2001)

Niikura C., Poissant Y., Gueunier M.E., Kleider J.P., Bourée J.E., J. Non-Cryst. Solids **299-302**, 1179 (2002)

Pant A., Russell T.W.F., Huff M., Aparicio R., Birkmire R.B., Ind. Eng. Chem. Res. **40**, 1377 (2001)

Peiró D., Bertomeu J., Voz C., Robin G., Andreu J., Proceedings of the 2nd World Conference on Photovoltaic Solar Energy Conversion, Vienna (H.S. Stephens and Associates, Bedford, UK), p. 766 (1998)

Peiró D., Ph.D. Thesis, University of Barcelona (1999)

Puigdollers J., Cifre J., Polo M.C., Asensi J.M., Bertomeu J., Andreu J., Lloret A., Appl. Surf. Sci. **86**, 600 (1995)

Rath J.K., Tichelaar F.D., Meiling H., Schropp R.E.I., Mat. Res. Soc. Symp. Proc. **507**, 879 (1998)

Rath J.K., Schropp R.E.I., Mat. Res. Soc. Symp. Proc. **609**, A22.1 (2000)

Roca i Cabarrocas P., Layadi N., Heitz T., Drévillon B., Appl. Phys. Lett. **66**, 3609 (1995)

Ruihua W., Zhiqiang L., Li L., Jahe L., Solar Energy Materials and Solar Cells **62,** 193 (2000)

Schropp R.E.I., Zeman M., "Amorphous and microcrystalline silicon solar cells" (Kluwer Academic Publishers, Boston 1998)

Schropp R.E.I., Rath J.K., IEEE Transactions on Electronic Devices **46**, 2069 (1999)

Schropp R.E.I., Alkemade P.F.A., Rath J.K., Solar Energy Materials and Solar Cells **65**, 541 (2001)

Schropp R.E.I., Thin Solid Films **403-404**, 17 (2002)

Shah A., Meier J., Vallat-Sauvain E., Droz C., Kroll U., Wyrsch N., Guillet J., Graf U., Thin Solid Films **403-404**, 179 (2002)

Soler D., Fonrodona M., Voz C., Bertomeu J., Andreu J., Thin Solid Films **383**, 189 (2001)

Soler D. Fonrodona M., Voz C., Asensi J.M., Bertomeu J., Andreu J., Thin Solid Films **430**, 157 (2003)

Staebler D.L., Wronski C.R., Appl. Phys. Lett. **31**, 292 (1977)

Stannowski B., Rath J.K., Schropp R.E.I., Thin Solid Films **430**, 220 (2003)

Stöger M., Breymesser A., Schlosser V., Ramadori M., Plunger V., Peiró D., Voz C., Bertomeu J., Nelhiebel M., Schattschneider P., Andreu J., Physica B **273-274**, 540 (1999)

Tsu R., González-Hernández J., Chao S.S., Lee S.C., Tanaka K., Appl. Phys. Lett. **40**, 534 (1982)

Vallat-Sauvain E., Kroll U., Meier J., Shah A., Pohl J., J. Appl. Phys. **87**, 3137 (2000)

Veen M.K. van, Ph.D. Thesis, Utrecht University (2003)

Veenendaal P.A.T.T. van, Rath J.K., Gijzeman O.L.J., Schropp R.E.I., Polycrystalline Semiconductors VI – Materials, Technologies, and Large Area Electronics in: O. Bonnaud, T. Mohammed-Brahim, H.P. Strunk, J.H. Werner (Eds.), Series 'Solid State Phenomena' **80-81**, 53 (2001), Scitec Publ., Uettikon am See, Switzerland

Veenendaal P.A.T.T. van, Werf C.H.M. van der, Schropp R.E.I., J. Non-Cryst. Solids **299-302,** 1184 (2002)

Voz C., Fonrodona M., Soler D., Peiró D., Asensi J.M., Bertomeu J., Andreu J., Proceedings of the 16th European Photovoltaic Solar Energy Conference, Glasgow (James & James (Science Publishers) Ltd.), p. 417 (2000)

Voz C., Peiró D., Bertomeu J., Soler D., Fonrodona M., Andreu J., Mat. Sci. Eng. **B69-70**, 278 (2000b)

Voz C., Ph.D. Thesis, University of Barcelona (2001)

Wiesmann H., Ghosh A.K., McMahon T., Strongin M., J. Appl. Phys. **50**, 3752 (1979)

Yamamoto K., Yoshimi M., Suzuki T., Tawada Y., Okamoto Y., Nakajima A., Proceedings of the 2nd World Conference and Exhibition on Photovoltaic Solar Energy Conversion, Vienna (H.S. Stephens and Associates, Bedford, UK), 1284 (1998)

Yu S., Gulari E., Kanicki J., Appl. Phys. Lett. **68**, 2681 (1996)

Zhu M., Guo X., Chen G., Han H., He M., Sun K., Thin Solid Films **360**, 205 (2000)

Acronym list

α: optical absorption coefficient

AFM: Atomic Force Microscopy

AM1.5: Air Mass 1.5

a-Si:H: amorphous silicon

Cat-CVD: Catalytic Chemical Vapour Deposition

C_H: hydrogen content

C_O: oxygen content

CVD: Chemical Vapour Deposition

d: thickness

D_H: hydrogen dilution

DLTS: Deep Level Transient Spectroscopy

E_a: dark conductivity activation energy

E_g: optical band gap

FF: fill factor

FTIR: Fourier Transform Infrared spectroscopy

γ: relative importance of recombination in charged states

G_S: grain size

η: solar cell efficiency

HRTEM: High-Resolution Transmission Electron Microscopy

HWCVD: Hot-Wire Chemical Vapour Deposition

ITO: Indium Tin Oxide

J_{sc}: short circuit current density

L: device thickness

LTCat-CVD: Low-Temperature Catalytic Chemical Vapour Deposition

μ: mobility

μc-Si:H: microcrystalline silicon

$\mu\tau$: mobility-lifetime product

n_0: refraction index

N_A, N_D: carrier concentrations

N_{DB}: Dangling bond density

nc-Si:H: nanocrystalline silicon

P: process pressure

PDS: Photothermal Deflection Spectroscopy

PECVD: Plasma-Enhanced Chemical Vapour Deposition

PID: Proportional-Integral-Derivative temperature control

p-Si:H: protocrystalline silicon

pm-Si:H: polymorphous silicon

poly-Si:H: polycrystalline silicon

r_d: deposition rate

RF: Radio Frequency

R_{oc}: open circuit resistance

R_p: parallel resistance

R_s: series resistance

R_{sc}: short circuit resistance

σ_d: dark conductivity

σ_{ph}: steady state photoconductivity

SIMS: Secondary Ion Mass Spectrometry

SS: Stainless Steel

SSPC: Steady State Photoconductivity

TCO: Transparent Conductive Oxide

TEM: Transmission Electron Microscopy

T_f: filament temperature

T_s: substrate temperature

T_{Ti}: Titanium temperature

UHV: Ultra-High Vacuum

VHF CVD: Very High Frequency Chemical Vapour Deposition

VIM: Variable Illumination Measurements technique

V_{bi}: built-in voltage

V_c: collection potential

V_{c0}: collection potential at intermediate illumination level

V_{oc}: open circuit voltage

X_c: crystalline fraction

XPS: X-ray Photoelectron Spectroscopy

XRD: X-Ray Diffraction

Figure list

Fig. 5.15. J-V curve of a completely Hot-Wire grown p-i-n solar cell measured under 100 mW/cm^2 illumination. The intrinsic layer was deposited at T_f = 1600ºC, T_s = 200ºC, P = 3x10^{-2} mbar, $\phi(SiH_4)$ = 4 sccm and D_H = 94.4%. Active cell area was 0.096 cm^2.

Fig. 5.16. Spectral response of a completely Hot-Wire grown p-i-n solar cell. The intrinsic layer was deposited at T_f = 1600ºC, T_s = 200ºC, P = 3x10^{-2} mbar, $\phi(SiH_4)$ = 4 sccm and D_H = 94.4%. Active cell area was 0.096 cm^2.

Fig. I.1. Schematic cross-section of the deposition chamber at Utrecht University.

Fig I.2. Thickness profile of a μc-Si:H film. The numbers represent the relative thickness in %.

Fig. I.3. Raman spectra of samples deposited with different starting sequences. Deposition conditions in both cases were T_f = 1850ºC, P = 0.15 mbar, D_H = 95.2% and $[PH_3]/[SiH_4]$ = 0.24%. Both samples were 360 nm thick.

Fig. I.4. Evolution of the Raman spectra measured illuminating from the top of the sample with thickness.

Fig. I.5. Dark conductivity at room temperature (σ_d) and activation energy (E_a) as a function of the filament temperature. The rest of the deposition conditions are P = 0.1 mbar, D_H = 98.7% and $[PH_3]/[SiH_4]$ = 0.92%. Lines are set as a guide for the eye.

Fig. II.1 Design of the catalytic tube for Low-Temperature Catalytic CVD.

Fig. II.2. Calibration of the titanium temperature as a function of the filament intensity at different pressures. The substrate temperature was set at 300ºC.

Fig. II.3. Transmittance spectra of SnO_2 layers after 15 minutes of hydrogen treatment at different T_{Ti}. The effect of the exposure to a hot-wire heated at 1650ºC for 15 minutes is also plotted for comparison.

Fig. II.4. Transmittance spectra of Corning 1737 glass and that of a LTCat-CVD thin silicon film.

Fig II.5. Superficial XPS analysis of the LTCat-CVD sample on stainless steel. The inset shows the region of the Si2p band, where the contributions corresponding to oxidised and metallically bonded silicon are seen.

Table list

Resum en català

1. Introducció

Avui en dia, prop del 99% de la producció de cèl·lules solars per aplicacions terrestres es basa en materials relacionats amb el silici. Un 85% d'aquesta producció correspon a la tecnologia d'oblies de silici. Malgrat aquest fet, els esforços esmerçats en les darreres dècades a abaratir costos en la fabricació de dispositius, han provocat un desenvolupament de la tecnologia de silici en capa fina, que permet la fabricació de dispositius utilitzant fins a cinc-centes vegades menys material i mitjançant tècniques de dipòsit relativament simples i econòmiques. Aquestes tècniques, a més a més, són compatibles amb l'ús de substrats barats com ara el vidre, l'acer inoxidable i plàstics.

Existeixen diferents tipus de silici en capa prima susceptibles d'ésser emprats en dispositius fotovoltaics, majoritàriament distingibles entre si per la quantitat de teixit amorf present i la mida dels grans cristal·lins. El més utilitzat és el silici amorf (a-Si:H), que presenta com a major problema el fet que les seves propietats elèctriques es degraden quan és exposat a períodes llargs d'il·luminació, el que s'anomena efecte Staebler-Wronski. El material objecte d'estudi en aquest treball és el silici nanocristal·lí (nc-Si:H), que consisteix en un agregat de cristallets de mides de l'ordre de desenes de nanòmetres en una matriu de silici amorf. La terminologia silici microcristal·lí (μc-Si:H) també es fa servir per descriure aquest mateix tipus de silici en capa fina.

El nc-Si:H s'obté majoritàriament per tècniques de dipòsit químic en fase vapor (*Chemical Vapour Deposition*, CVD), on el material es diposita sobre el substrat després de produir-se la dissociació de la mescla de gasos que conté el precursor. Existeixen diferents tipus de CVD depenent del mecanisme que provoca la dissociació. Les capes estudiades en aquest treball han estat dipositades per dipòsit químic en fase vapor assistit per filament calent (*Hot-Wire Chemical Vapour Deposition*, HWCVD). En aquesta tècnica, també anomenada dipòsit químic catalític en fase vapor (*Catalytic CVD*, Cat-CVD), el silici és dipositat després d'haver-se descompost catalíticament la mescla de gasos, silà (SiH_4) i hidrogen (H_2), a la superfície d'un filament calent escalfat a temperatures de l'ordre de 1500-2000ºC. Aquesta tècnica presenta alguns avantatges si la comparem amb el dipòsit químic en fase vapor assistit per plasma (*Plasma-Enhanced*

CVD, PECVD), la tècnica més utilitzada actualment per al dipòsit de silici en capa fina, com són l'absència de bombardeig iònic durant el procés, els alts ritmes de dipòsit assolits, i el baix cost d'instal·lació i manteniment dels equips de dipòsit. Actualment es poden trobar en la literatura cèl·lules solars amb eficiències fins el 9.4% que incorporen capes intrínseques dipositades amb HWCVD, així com excel·lents resultats també en el camp dels transistors en capa prima (*Thin Film Transistors*, TFT) i del dipòsit en gran àrea.

El primer equip de HWCVD a la Universitat de Barcelona es va instal·lar el 1993. Les primeres capes de silici policristal·lí (tant intrínsec com dopat) crescudes a Europa es van dipositar en aquest primer equip. Amb anterioritat a aquest treball, els resultats relacionats amb la tecnologia del silici nanocristal·lí a la Universitat de Barcelona es poden trobar a les tesis doctorals del Dr. D. Peiró i el Dr. C. Voz, on es descriuen extensament el sistema de dipòsit actual i la caracterització estructural, elèctrica i òptica tant del material pròpiament dit com dels primers dispositius fotovoltaics crescuts per HWCVD. En les conclusions d'aquest treballs es van identificar una sèrie de problemes d'aquests primers dispositius analitzats, principalment atribuïbles a la presència d'impureses contaminants a la capa intrínseca. D'aquesta manera, la meta del treball aquí presentat era l'optimització tant del sistema com de les condicions de dipòsit per tal d'obtenir cèl·lules enterament crescudes per HWCVD estables i amb una major eficiència de conversió.

2. Sistema experimental i tècniques de caracterització

Equip de dipòsit

L'equip de dipòsit mitjançant HWCVD està format per tres cambres d'ultra-alt buit aïllades entre si. Una primera cambra s'utilitza com a cambra de càrrega i per a dipositar òxids conductors transparents (*Transparent Conductive Oxide*, TCO) per als contactes mitjançant polvorització catòdica magnetró. Un sistema de transferència magnètic s'empra per traslladar els substrats fins a la cambra on es realitzarà el dipòsit. Les dues cambres restants és on es diposita el silici en capa prima mitjançant HWCVD. En una d'elles es diposita solament material intrínsec mentre que en l'altra s'hi creixen capes dopades, tant tipus p com tipus n, afegint petites quantitats controlades de diborà (B_2H_6) o fosfina (PH_3) a la mescla d'hidrogen i silà. S'utilitzen cambres separades per al dipòsit de material

intrínsec i dopat per tal d'evitar qualsevol incorporació no desitjada de contaminació creuada a la capa activa del dispositiu.

Per tal d'evitar en part la incorporació de contaminants durant el procés de dipòsit, la cambra on es realitza el dipòsit de material intrínsec ha sofert una sèrie de canvis. Primerament, el calefactor intern de resistència de grafit –que era una font potencial d'impureses- es va substituir per un d'extern, que bàsicament consistia en un bloc d'alumini amb quatre resistències de 200 W connectades en paral·lel.

Durant el treball que aquí es presenta, també es va incloure en la mateixa cambra una mena d'embut protector que tenia com a finalitat protegir el flux de gas i els substrats d'altres fonts potencials d'impureses com podien ser les parets de la cambra o els extrems freds del filament. Com que els extrems del filament queden fora de l'embut protector, aquest sistema també serveix per disminuir la quantitat de siliciurs que es formen en aquestes regions més fredes del filament.

Tàntal i tungstè són, en l'actualitat, els dos materials més utilitzats com a catalitzador en HWCVD. La tria entre els dos sembla dependre, majoritàriament, del rang de temperatures que es considera. El tàntal és més dúctil i menys fràgil que tungstè, i permet treballar a temperatures de filament més baixes ja que forma menys siliciurs. Pel contrari, la ductilitat i la tendència del Ta a deformar-se a temperatures lleugerament elevades fa que els filaments d'aquest material siguin més difícils de reproduir. Les capes analitzades en aquest treball, si no es diu el contrari, han estat dipositades fent servir un filament de tàntal. La geometria utilitzada és la de cistella invertida de tres voltes, exceptuant les mostres fetes després de la col·locació de l'embut, on els filaments són lineals.

Tècniques de caracterització

El gruix de les capes s'ha mesurat amb un perfilòmetre Dektak 3030 i a partir d'aquesta mesura s'ha calculat el ritme de dipòsit mitjà de les capes. La mida dels grans cristal·lins (G_s) s'ha avaluat mitjançant mesures de difracció de raigs X (*X-Ray Diffraction*, XRD). La fracció cristal·lina (X_c) de les mostres l'hem estimada a partir de les contribucions amorfa i cristal·lina dels espectres Raman. Altra caracterització morfològica i estructural que s'ha dut a terme en algunes mostres ha estat per microscopia electrònica de transmissió (*Transmission Electron Microscopy*, TEM) i microscopia de força atòmica (*Atomic Force Microscopy*, AFM). L'anàlisi composicional de les mostres s'ha realitzat, bàsicament, per

espectroscòpia d'infraroig per transformada de Fourier (*Fourier Transform Infrared spectroscopy*, FTIR), que ens ha permès de calcular el contingut d'hidrogen i oxigen de les capes, i per espectrometria de masses d'ions secundaris (*Secondary Ion Mass Spectrometry*, SIMS). Les propietats òptiques del material s'han avaluat per mitjà de mesures d'espectroscòpia de deflexió fototèrmica (*Photothermal Deflection Spectroscopy*, PDS) i de transmitància òptica. Per mitjà d'aquestes tècniques es poden calcular el coeficient d'absorció (α) a cada longitud d'ona i l'amplada de la banda prohibida (E_g). Pel que fa a les mesures elèctriques, la conductivitat a temperatura ambient (σ_d) i l'energia d'activació (E_a) s'han obtingut de mesures de resistència en funció de la temperatura. La fotoconductivitat (σ_{ph}) de les mostres s'ha obtingut de mesures de fotoconductivitat en estat estacionari (*Steady State Photoconductivity*, SSPC).

Pel que fa referència a les cèl·lules solars, el funcionament dels dispositius s'ha analitzat a partir de la mesura de corbes corrent-tensió a 100 mW/cm^2 i a diferents nivells d'il·luminació al llarg de diversos ordres de magnitud de llum incident, el que s'anomena *Variable Illumination Measurement technique* (VIM), i de la mesura de la resposta espectral.

3. La recerca de material químicament estable

El paper del filament

Els intents fracassats d'obtenir material de qualitat que no s'oxidés fent servir el filament de tungstè, juntament amb el fet que temperatures de filament altes afavorissin la incorporació d'impureses durant el creixement de les capes, van provocar el canvi de catalitzador utilitzat de tungstè a tàntal.

Els estudis preliminars de la influència de la temperatura de substrat i la dilució emprades en el dipòsit van donar els millors resultats a T_s = 200ºC i D_H = 95% (4 sccm de SiH_4 i 76 sccm de H_2) treballant a una pressió de $3x10^{-2}$ mbar. En aquestes condicions, es va observar, al voltant de T_f = 1700ºC, una transició de direcció cristal·lina preferent de (220) a (111) en baixar la temperatura de filament en capes de gruix lleugerament inferior a 1 μm. L'anàlisi de les capes amb FTIR fetes tres mesos després del dipòsit va mostrar un alt grau d'oxidació en les mostres dipositades a $T_f \geq 1700$ºC, mentre que les dipositades amb el filament més fred presentaven un grau d'oxidació molt menor. Els perfils de SIMS

van mostrar que, en aquest darrer cas, la incorporació d'oxigen era molt més superficial que per a les capes dipositades a alta T_f. Aquest material químicament més estable i en aparença més compacte consistia en grans cristal·lins enmig d'una matriu amorfa, de manera que la major compacitat d'aquestes capes es va associar a una major densitat del teixit amorf i de les fronteres de gra. Aquesta diferència apreciada en el material en disminuir la temperatura del filament es va atribuir a diferències en la dissociació del silà al filament, de tal manera que a temperatures de filament més baixes la quantitat de SiH_4 no descompost al filament és major. D'aquesta manera, a baixa temperatura queda més SiH_4 per descompondre's en la reacció secundària $SiH_4 + H \rightarrow SiH_3 + H_2$ i, per tant, es produeix més SiH_3. Aquest radical és considerat el responsable del creixement de material dens en capes de PECVD.

L'aplicació d'aquest material més estable (T_f ~ 1550ºC) a una cèl·lula solar amb estructura p-i-n i sense cap mena de confinament òptic va evidenciar una major estabilitat en comparació amb cèl·lules més antigues dipositades amb filament de tungstè. Malgrat tot, aquest dispositiu també presentava un cert grau de degradació i uns valors que indicaven la presència, encara que en menor grau, d'impureses en la capa activa del dispositiu.

L'embut

Per tal d'evitar la possible incorporació d'impureses provinents de les parets o de les parts més fredes del filament, es va col·locar un embut protector a la sortida de gasos. Aquest embut també havia de servir per a minimitzar la formació de siliciurs a les parts més fredes del filament ja que aquestes quedaven fora de la influència directa del flux de gas entrant. La col·locació de l'embut va provocar un canvi de la geometria del filament vers l'ús de filaments lineals, causant una lleugera disminució en el ritme de dipòsit. A partir del dipòsit de tres capes en condicions idèntiques, per una banda es va verificar la no incorporació d'oxigen durant el creixement i, per l'altra, es va descartar l'existència de qualsevol efecte secundari derivat d'un possible envelliment o embrutament del filament i l'embut. També es va realitzar una escombrada de paràmetres al voltant del punt on es tenia el millor material per comprovar si el fet d'haver col·locar l'embut havia afectat d'alguna manera les condicions de dipòsit considerades òptimes fins al moment.

El material intrínsec que presentava les millors condicions es va fer servir com a capa activa en una cèl·lula p-i-n sense cap mena d'estratègia per a confinar la llum. Els resultats obtinguts mostraven una eficiència conversora pobra a causa de la manca d'optimització tant de les capes dopades com del confinament òptic. Malgrat aquest fet, tal i com van palesar les mesures de VIM dutes a terme durant 1000 hores d'il·luminació AM1.5, no es va evidenciar cap mena de degradació atribuïble a manca de qualitat de la capa intrínseca o a la formació de defectes induïts per la il·luminació, tot i que la fracció cristal·lina de la capa intrínseca era 0.51, és a dir, tenia una quantitat important de teixit amorf.

4. Influència del substrat i material dopat

Petits canvis en les condicions de dipòsit de les capes fines de silici poden donar lloc a canvis molt més evidents en la microestructura de les capes resultants. Molt sovint, les propietats del material s'analitzen en mostres crescudes sobre substrats de vidre i després les conclusions extretes s'extrapolen directament al dispositiu, on les capes es creixen sobre substrats diferents. Per tal de verificar el possible efecte de la naturalesa del substrat en l'estructura de capes intrínseques de nc-Si:H, especialment prop de la transició a a-Si:H, es van dipositar una sèrie de mostres per diferents valors de dilució d'hidrogen (D_H) alhora sobre vidre, ZnO:Al, silici i acer inoxidable. D_H es va variar entre el 75 i el 95%, i la resta de condicions de dipòsit van ser T_f = 1650ºC, T_s = 200ºC i P = $3x10^{-2}$ mbar. En tots els casos, la transició de a-Si:H a nc-Si:H es va produir en un marge estret de dilucions, però la quantitat d'hidrogen necessària per començar a veure creixement nanocristal·lí va variar depenent de quin fos el substrat analitzat. El substrat on es va detectar creixement nanocristal·lí abans va ser l'acer inoxidable (a D_H = 90%), mentre que sobre el vidre totes les mostres van sortir amorfes excepte la crescuda a D_H = 95%. El llindar en el silici i el ZnO:Al estava en dilucions intermitges. D'aquesta manera, es va observar que, per a una dilució en concret, idèntiques condicions de dipòsit poden resultar en material amorf, nanocristal·lí amb important contribució amorfa o enterament nanocristal·lí. De la comparació dels nostres resultats amb els de la literatura, es va poder arribar a la conclusió que semblava que com més gran fos la conductivitat del substrat, menys hidrogen era necessari per tenir creixement nanocristal·lí. Malgrat tot, el mecanisme responsable d'aquest comportament no ha estat identificat.

Com que en les cèl·lules solars en capa prima les capes que realment es dipositen sobre TCO o metall són les capes dopades, es va repetir el mateix experiment amb capes dopades tipus p i tipus n, per tal de veure si la inclusió de gas dopant feia canviar d'alguna manera la tendència observada per al material intrínsec. Es va veure una clara diferència en comportament, tant en mesures de Raman com en les elèctriques, depenent de si el tipus de dopant emprat havia estat fosfina o diborà. Les mostres tipus n presentaven una dependència amb el tipus de substrat anàloga a l'observada en les intrínseques, llevat que, en tots els substrats, el creixement cristal·lí es donava per dilucions més baixes. A D_H = 85% els espectres Raman mostraven contribució cristal·lina en tots els casos. Aquest comportament va ser atribuït al fet que els àtoms de fòsfor poguessin actuar com a centres de nucleació dels grans cristal·lins. Per altra banda, van caler dilucions d'hidrogen del 95 i el 96% per poder detectar cap contribució nanocristal·lina a les mostres dopades tipus p. Sorprenentment, per aquestes mostres el substrat en el que es va veure abans nc-Si:H va ser el vidre, i pel que va fer falta més hidrogen, l'acer inoxidable, contràriament al que s'havia observat per a les capes intrínseques i tipus n. El fet que calgués més hidrogen per créixer nc-Si:H tipus p es va atribuir a l'amorfització, ja coneguda, que causa la incorporació de diborà a la mescla de gasos.

Partint del material dopat més adequat per formar part d'una cèl·lula solar, es van dipositar capes amb un gruix similar al necessari en els dispositius (~50 nm). Això va provocar que s'hagués de doblar en la capa n la quantitat de dopant necessària per tal de tenir bones propietats elèctriques (P/Si = 2% amb T_f = 1750ºC, T_s = 200ºC, P = $3x10^{-2}$ mbar i D_H = 95%). Pel que fa referència a les capes p, les mateixes condicions de dipòsit de les capes gruixudes van donar capes primes amb bones propietats elèctriques (B/Si = 5% amb T_f = 1850ºC, T_s = 125ºC, P = $3x10^{-2}$ mbar i D_H = 96%).

5. Cèl·lules solars

Aspectes previs

Malgrat que l'optimització del material de la capa activa és el tema central en el desenvolupament de les cèl·lules de nc-Si:H, hi ha altres aspectes que també s'han de tenir en compte per tal d'obtenir dispositius amb eficiències de conversió raonables: les fuites laterals i el confinament òptic. En cèl·lules solars en capa prima, les fuites laterals són

degudes a què en CVD les vores no queden perfectament definides i llavors les capes n o i poden contactar lateralment el TCO. Una part del corrent paràsit creat per aquestes fuites es pot evitar interrompent físicament el camí que aquest hauria de seguir. En col·laboració amb la Universitat Politècnica de Catalunya s'han atacat alguns dels nostres dispositius amb un plasma de CF_4, aconseguint una clara reducció de les fuites laterals.

Mitjançant confinament òptic, augmentant la quantitat de llum absorbida en el dispositiu, es pot aconseguir augmentar el rendiment de les cèl·lules fent servir capes actives més primes ja que s'augmenta el recorregut de la llum dins el dispositiu. Primerament s'ha utilitzat un substrat texturat -SnO_2:F comercial (Asahi-U) recobert de ZnO:Al per tal que no es redueixi- i seguidament s'han fet les primeres proves amb ZnO:Al i plata com a reflector posterior. S'ha demostrat que aquestes dues estratègies tenen com a conseqüència un augment en el corrent en curtcircuit de les cèl·lules.

Cèl·lules solars de nc-Si:H

Totes les cèl·lules solars analitzades en aquest capítol són del tipus p-i-n. El substrat utilitzat és Asahi-U recobert de ZnO:Al i les capes dopades són com les primes descrites en el capítol anterior amb un gruix aproximat de 70 nm per les tipus p i 50 nm per a les tipus n. L'objectiu a estudiar era la possible relació entre la fracció amorfa de la capa intrínseca d'una cèl·lula p-i-n i la possible creació de defectes generats per la llum. Aquesta anàlisi es va fer amb cèl·lules on la capa intrínseca s'havia dipositat amb dilucions d'hidrogen lleugerament diferents (D_H = 93.5-95%). Una anàlisi estructural d'aquestes mostres va posar en evidència que diferències molt petites en les condicions de dipòsit poden donar lloc a canvis apreciables en la microestructura del material, com van fer palès els espectres de Raman d'aquests dispositius. Posteriorment les mostres dipositades a D_H = 95, 94.4 i 93.8% es van deixar sota il·luminació AM1.5 durant 1000 hores. L'evolució de les cèl·lules es va anar seguint a partir de mesures de VIM. En les cèl·lules dipositades amb més hidrogen (D_H = 95 i 94.4%), els únics canvis observats es van poder atribuir a efectes fora de la unió p-i-n. Només pel dispositiu crescut amb D_H = 93.8% es van observar efectes anàlegs als que sofreixen les cèl·lules solars de a-Si:H atribuïbles a una degradació de les propietats de la capa activa del dispositiu. Les mesures de VIM també van permetre de quantificar la densitat d'enllaços no saturats (*dangling bond density*, N_{DB}) durant el temps d'il·luminació. N_{DB} es va mantenir constant per D_H = 95 i

94.4%. Pel dispositiu del 93.8%, N_{DB} va augmentar amb el temps d'exposició a la llum. Un recuit a 180ºC de la mostra va retornar el valor de N_{DB} a valors semblants als observats al cap de 100 hores d'il·luminació, mostrant la coexistència de dos mecanismes: un de reversible (imputable a la creació de defectes induïts per la llum a la capa activa del dispositiu) i un d'irreversible (que es podria atribuir a una difusió de dopant provinent de la capa p dipositada a baixa temperatura cap a la capa intrínseca). La coexistència d'aquests dos mecanismes es va verificar a partir de la modelització del comportament de la resistència en curtcircuit en funció de la il·luminació, corroborant que tots els dispositius sofreixen una degradació irreversible causada per estabilització de les superfícies i interfícies (com oxidació o difusió de dopant) i que la degradació reversible (atribuïble a la influència del teixit amorf en les propietats de transport del nc-Si:H) només es dóna en els materials amb més contribució amorfa. El llindar de teixit amorf necessari per observar aquest segon comportament es troba entre 0.40 i 0.45 de fracció cristal·lina.

El millor resultat fins al moment obtingut per una cèl·lula solar de nc-Si:H on s'han tingut en compte tots els aspectes descrits anteriorment correspon al de la cèl·lula on la capa intrínseca havia estat dipositada amb D_H = 94.4%. Aquesta cèl·lula presenta una eficiència del 5.15% amb J_{sc} = 17.4 mA/cm^2, V_{oc} = 0.47 V i FF = 0.63. Malgrat el resultat aconseguit, aquest dispositiu presentava problemes causats per una capa p massa gruixuda, de manera que optimizant el gruix d'aquesta i també millorant el confinament òptic es podrien aconseguir eficiències de conversió superiors. Aquesta eficiència màxima s'ha aconseguit creixent el material a tan sols 1.1 Å/s i tenint bona reproductibilitat sobre tot el substrat de polzada per polzada. Partint d'aquí, en un futur s'hauria de considerar augmentar l'àrea efectiva de filament per tal d'obtenir resultats semblants o millors en superfícies més grans i més ràpidament.

Conclusions

El principal problema de les cèl·lules solars de nc-Si:H presentades en treballs anteriors a aquest era la presència d'impureses que en limitaven el funcionament. En aquest treball s'han presentat una sèrie de resultats que pretenien disminuir aquesta presència no desitjada en els dispositius:

- Els diferents intents d'aconseguir material compacte utilitzant un filament de tungstè no van donar fruit, motivant un canvi de catalitzador vers l'ús de tàntal. Els estudis preliminars amb aquest filament van donar resultats prometedors a $D_H = 95\%$ i $T_s = 200ºC$.

- Una transició de direcció cristal·lina preferencial (111) a (220) al voltant de 1700ºC va ser observada en disminuir la temperatura de filament. Les mostres dipositades a baixa T_f van resultar ser més compactes ja que la incorporació d'oxigen després del dipòsit en elles es limitava a una capa superficial. La diferència en comportament es va atribuir a una diferència en la quantitat de SiH_3 produït al filament en baixar la seva temperatura.

- La incorporació d'impureses (majoritàriament oxigen) durant el dipòsit de les capes es va suprimir amb la inclusió d'un embut protector. Les cèl·lules solars on la capa activa havia estat dipositada amb l'embut van mostrar una gran estabilitat tant en fosc com sota il·luminació AM1.5

El substrat on es diposita una capa té una influència directa en l'estructura de la mateixa, de manera que cal prendre precaucions i no extrapolar conclusions del material obtingut sobre un substrat al dipositat sobre un altre. Aquest comportament es va veure per capes intrínseques i dopades sobre diferents substrats (vidre, silici, ZnO:Al i acer inoxidable):

- Per a capes intrínseques, l'acer inoxidable va semblar afavorir el creixement cristal·lí mentre que el cas més desfavorable va resultar ser el vidre. El ZnO:Al i el silici van presentar un comportament intermig.

- En les capes n es va observar un comportament anàleg al comentat amb les mostres intrínseques, tot i que en tots els casos el creixement cristal·lí es produïa amb quantitats menors d'hidrogen. Una possible causa en seria la nucleació dels grans cristal·lins al voltant dels àtoms de fòsfor.

- En el cas de les capes p, van fer falta dilucions d'hidrogen majors en tots els casos per obtenir nc-Si:H. Aquest fet pot ser degut a una amorfització causada per la presència de diborà a la mescla de gasos. Addicionalment, en aquest tipus de capa el substrat que va donar creixement cristal·lí abans va ser el vidre i el darrer, l'acer inoxidable.

- Les capes dopades, tant p com n, que presentaven millors propietats es van aprimar fins a gruixos adequats per a dispositiu mantenint bones propietats elèctriques. Es van obtenir capes dopades tipus n de 40 nm amb $\sigma_d = 5$ S/cm i $E_a = 0.02$ eV, i capes tipus p de 50 nm amb $\sigma_d = 2.5$ S/cm i $E_a = 0.04$ eV.

Finalment, s'han analitzat diferents aspectes de cèl·lules solars dipositades en la configuració p-i-n:

- S'ha demostrat que es pot augmentar l'eficiència de les cèl·lules solars en capa prima mitjançant tècniques de confinament òptic i evitant fuites laterals.

- S'han sotmès a 1000 hores d'il·luminació AM1.5 cèl·lules solars amb lleugeres diferències en la cristal·linitat de la capa intrínseca. Aquest experiment ha mostrat que els nostres dispositius sofreixen canvis irreversibles atribuïbles a una estabilització química de superfícies i interfícies com poden ser efectes d'oxidació dels contactes o de difusió de dopant vers la capa activa.

- Cèl·lules solars amb una fracció cristal·lina de la capa intrínseca inferior a 0.45 han mostrat, a més a més, una creació de defectes deguda a l'exposició a la llum. Aquest efecte és reversible amb un recuit a 180ºC i ha estat atribuït a la influència del teixit amorf en les propietats de transport de la capa nanocristal·lina.

- Una eficiència del 5.15% s'ha aconseguit en una cèl·lula incloent tots aquests aspectes, malgrat identificar-hi certs problemes relacionats amb les capes dopades i els contactes, que caldrà optimitzar en un futur. Més perspectives de futur estan relacionades amb augmentar l'àrea útil del filament, i encarades a reproduir i millorar aquests resultats en superfícies més grans i amb velocitats de dipòsit majors.

Annex I: Capes de silici microcristal·lí dopades amb fòsfor dipositades per HWCVD sense l'ús d'obturador

Aquesta part del treball recull els resultats obtinguts durant l'estada de tres mesos realitzada a la Universitat d'Utrecht (Holanda). Durant aquest període, es van dipositar en aquella universitat les primeres capes de μc-Si:H tipus n amb HWCVD. La caracterització de les mateixes es va dur a terme tant a Utrecht com a la Universitat de Barcelona.

Per tal de poder dipositar les capes tipus n per HWCVD, es van col·locar dos filaments de tàntal separats 4 cm entre si i col·locats 1.5 cm per sobre el substrat, en la cambra de dipòsit tipus n. Com que es va voler mantenir el capçal de PECVD dins la mateixa, es va haver de retirar l'obturador present a la cambra i que habitualment s'utilitza per evitar dipòsit mentre les condicions de dipòsit no són estables. La poca separació filament-substrat comparada amb la distància entre els dos filaments va causar que el dipòsit no fos

homogeni en tot el substrat. Es va observar una capa d'incubació amorfa d'uns 20 nm com a conseqüència de la manca de control de les condicions de dipòsit, causada per la manca d'obturador, durant els primers instants del dipòsit. La seqüència d'entrada dels gasos i d'ajust de paràmetres va induir canvis en l'estructura del material resultant. Es van aconseguir capes de μc-Si:H tipus n amb bones propietats elèctriques, de manera que es va concloure que, malgrat que la presència d'un obturador en la cambra de dipòsit pot ser aconsellable, no és necessària.

Annex II: Dipòsit químic catalític en fase vapor a baixa temperatura

La producció d'hidrogen en HWCVD és un ordre de magnitud superior que en PECVD. En HWCVD, el SiH_3, que es considera el principal precursor del creixement de material de qualitat, es creu que es forma principalment a partir de reaccions secundàries entre silà i hidrogen atòmic produït catalíticament a la superfície del filament. A partir d'aquestes dues afirmacions, es va intentar dissenyar un sistema de dipòsit a baixa temperatura que evités qualsevol incorporació d'impureses al material crescut. Amb aquesta finalitat es va dissenyar l'equip que s'anomenaria de dipòsit químic catalític en fase vapor a baixa temperatura (*Low Temperature Catalytic CVD*, LTCat-CVD). El LTCat-CVD consisteix en el dipòsit de silici en capa prima a partir de les reaccions produïdes entre silà i hidrogen atòmic. Aquest hidrogen atòmic es produiria de la dissociació catalítica d'hidrogen molecular en travessar un tub de titani escalfat per mitjà d'un fil de tàntal.

Primerament es va avaluar l'eficiència de descomposició d'hidrogen del tub de titani escalfat. Per això es van fer servir capes d'òxid d'estany (SnO_2) com a indicador, ja que aquest material s'enfosqueix en reduir-se en ambients altament reductors. Els resultats obtinguts es van comparar amb la transmitància d'una capa de SnO_2 sotmesa a quinze minuts de descomposició d'hidrogen per HWCVD en condicions de temperatura de filament similars habituals a les de dipòsit. Van fer falta temperatures de titani superiors a 250ºC per detectar enfosquiment en la capa de SnO_2. Per sobre de 400ºC, un augment de la temperatura del tub ja no es traduïa en un major enfosquiment del SnO_2, de manera que tot semblava indicar que en aquestes condicions tot l'hidrogen es dissociava.

Un intent preliminar de dipositar silici mitjançant aquesta tècnica (T_{Ti} = 400ºC, T_s = 400ºC, P = 1 mbar, 8 sccm de SiH_4 i 20 sccm de H_2) va tenir com a resultat una mostra extremadament prima. Mesures de transmitància i d'espectrometria de fotoelectrons

van revelar la presència d'una capa molt prima de silici sobre els substrats de vidre i acer inoxidable. El ritme de dipòsit extremadament baix amb el qual va créixer aquesta mostra, fa inviable per ara el LTCat-CVD com a alternativa a HWCVD o PECVD. Malgrat això s'ha pogut demostrar que es poden dipositar capes fines de silici mitjançant aquest nou procediment.

Annex III: La tècnica del *Variable Illumination Measurement* (VIM)

La tècnica de la mesura a diferents il·luminacions (*Variable Illumination Measurement*, VIM) consisteix en la mesura de corbes corrent-tensió per diferents nivells d'il·luminació. D'aquestes mesures s'obtenen els diferents paràmetres característics del dispositiu i s'analitza la seva evolució en funció del corrent en curtcircuit, que és un indicador del nivell d'il·luminació. L'estudi del comportament d'aquests paràmetres ens permet identificar diferents factors responsables de la degradació d'un dispositiu (degradació dels contactes, difusió de dopant, creació de defectes en el si de la capa intrínseca, etc.).

La relació existent entre la resistència en curtcircuit i el corrent en curtcircuit per a nivells d'il·luminació intermedis ens ha permès avaluar la quantitat de defectes no saturats presents a la capa activa de les nostres cèl·lules. Per altra banda, un model del comportament de la resistència en curtcircuit en funció de la il·luminació, que ha tingut en compte les resistències paràsites pròpies de tot dispositiu no ideal i les contribucions de defectes neutres i carregats en la recombinació, ha estat emprat per avaluar la contribució d'aquests diferents mecanismes en diferents moments de la vida dels nostres dispositius.